8-11-2014

Classifying Mechanisms of Spiral Wave Breakup Underlying Cardiac Fibrillation Using Quantitative Metrics

Sejal Jagdish Rai

Classifying Mechanisms of Spiral Wave Breakup Underlying Cardiac Fibrillation Using Quantitative Metrics

by

Sejal Jagdish Rai

A Thesis Submitted in Partial Fulfillment of the Requirements
for the Degree of Master of Science in Applied and Computational Mathematics

School of Mathematical Sciences
College of Science

Rochester Institute of Technology
Rochester, NY

Aug 11, 2014

Advisor: Prof. Elizabeth M. Cherry

Committee: Prof. Elizabeth M. Cherry

Prof. Tamas Wiandt

Prof. Laura Munoz

Abstract

Cardiovascular diseases are one of the leading causes of death in the world and manifest themselves in several forms, including arrhythmias. These disruptions in the normal rhythm of the heart inhibit the regular transmission of electrical signals that are essential for the heart to contract and pump blood to the rest of the body. During reentrant arrhythmias, spiral or scroll waves of electrical activation are conducted through the cardiac tissue and excite it repeatedly. As these waves propagate through the heart, they can break up in an irregular manner, leading to the onset of fibrillation. There are several mechanisms by which these reentrant waves can destabilize, but they are known mostly from computational studies. Experimentally, it has not been possible so far to distinguish among these mechanisms based on straightforward observations of the heart's voltage during fibrillation. As a preliminary step in this direction, we aim to determine whether quantifying certain observable properties of the system will allow us to identify the mechanism underlying a given fibrillation episode.

Toward this end, we propose a number of metrics that could help us classify mechanisms underlying fibrillation, including chaos in the system as assessed by the largest Lyapunov exponent; the amount of information (mutual information) and dependency (spatial correlation) shared by various spatial points in the domain; and reentrant wave properties like the number of reentries, wave birth and death rates, reentrant wave lifetimes, and spiral wave tip speeds. We implement and apply these metrics to simulated data obtained by numerically solving partial differential equations describing electrical wave propagation in the heart. Specifically, we analyze data achieved through six different mechanisms of reentrant wave breakup: steep APD restitution, discordant alternans, bistability, Doppler effect, supernormal conduction velocity and periodic boundary conditions. Our results suggest that of the various reentrant wave properties, the distribution of the number of reentries over time serves to be the most useful metric by providing a visual representation of how

the breakup proceeds with time for each mechanism. When the mutual information and spatial correlation are studied in the context of the distribution of reentries over time, they help us gauge any spatial dependencies that may be present in the system.

To validate our findings, we carried out a blind test to classify breakup mechanisms in four provided data sets with established breakup mechanisms. Our metrics correctly classified the mechanisms for three of these cases, and we are confident that further optimization could improve the reliability of our approach. Our work forms the basis for future studies that apply these and other metrics towards identifying the mechanisms responsible for fibrillation in experimental settings.

Dedication

First of all, I would like to thank my advisor, Professor Elizabeth M. Cherry for her constant guidance and support right through my thesis, and especially her patience and co-operation with all my timings. Of course, this feat would not have been possible without the encouragement that I received from my family and friends from across the oceans. A big thank you to Nathaniel Bush, for the numerous valuable discussions that we have had and for being able to inspire me with his incredible work ethic. I would also like to thank Ambika Shetty, my dearest friend who has been with me on this, right from the beginning, and has encouraged me on every step of the way.

Contents

List of Tables

List of Figures

Chapter 1

Introduction

Cardiovascular disease stems from the irregular functioning of the heart or blood vessels. A person exhibiting such symptoms would be at increased risk of heart attack, heart failure, sudden death, stroke and cardiac rhythm problems, thus resulting in decreased quality of life and decreased life expectancy. It is also one of the leading causes of death in the modern world [1]. Ventricular fibrillation is a chaotic electrical activity in the myocardium that inhibits the heart's ability to contract, in turn rendering it unable to carry out its normal pumping function. During the normal functioning of the heart, the presence of a single wave of excitation (an electrical impulse) triggers the cells of the ventricles to contract and pump blood to the rest of the body; however, during fibrillation the presence of several electrical waves with a lack of co-ordination poses as a hindrance to carry out this task [2] [3] [4]. This leads to sudden cardiac death if not halted [1]. The ventricles have an extremely complicated spatiotemporal pattern during fibrillation which disrupts the regular functioning of the heart—in which case normalcy can be re-established by administering a defibrillating shock to the heart. Previous studies [5] [6] have suggested that reentry sustains the accelerated activation of the ventricles during fibrillation, which is largely caused by an action potential propagating into areas of recovered tissue (regions consisting of cells that are quiescent or not excited) during reentry. Action potential refers to the response of the cardiac cell, when electrical impulses cause changes in the membrane potential of these cells. In the normal rhythm of the heart, electrical waves are conducted by the myocardial cells in a regular fashion. After the

onset of an electrical wave, the heart undergoes a refractory period after the previous wave dies out and before the onset of the next wave. The refractory period is the period during which the cells cannot support another action potential if stimulated. When a propagating wave does not die out after the electrical excitation of the heart, it persists and can re-excite the heart, which constitutes reentry [7]. One of the ways that reentry manifests itself is in the form of spiral waves in 2D and scroll waves in 3D. Experimental observations have confirmed the presence of spiral waves in the heart during arrhythmias [2] [3] [4]. Although the concept of reentry is clear, the manner in which it is initiated is still not clearly understood. When reentrant waves run into tissue that is partially refractory or partially recovered, it gives rise to wave break, resulting in the formation of new waves at that site. This refractory tissue thus behaves as a conduction block, as it cannot be excited until it has completely recovered and, hence, prevents any further propagation of waves that invade the region. As discussed in later chapters, these conduction blocks feature in the different mechanisms of spiral wave breakup and influence the manner in which the breakup occurs. In the United States, ventricular fibrillation causes around 15% of all deaths [1]. Several methods such as implantable devices and antiarrhythmic drugs have been used to prevent this condition but have not always been successful [8] [9] [10] [11].

Despite the ongoing research in this field, from a clinical point of view, the exact mechanism behind the onset of ventricular fibrillation and the exact dynamics of the heart suffering from this condition remain unclear. The lack of experimental data as well as limitations in obtaining this data make it a challenging feat; however, extensive computational approaches combined with robust mathematical modeling allow another avenue for insights into mechanisms that lead to spiral wave breakup in cardiac tissue.

As illustrated in [5], some of the mechanisms that lead to spiral wave breakup are steep APD restitution-induced breakup, bistability, Doppler effect, supernormal conduction velocity and periodic boundary conditions, all of which will be discussed more in detail in the later chapters. The wave breaks that result from most of these mechanisms look similar, so trying to discern them visually in a given scenario is usually not possible. Of course, recognizing the mechanism that leads to wave breakup in a particular case is expected to give some valuable insights into how to prevent

or treat a given arrhythmia.

In this thesis, we propose tools that could be employed to classify the mechanism of an arrhythmic episode based on observable properties. Presently, we are not aware of any existing research that has been carried out on this exact topic and one of the leading reasons for this could be the lack of perfect knowledge of the experimental system coupled with the paucity of data. Our main aim is to provide some means of differentiating among these mechanisms, as this is a problem that is not suitable for the human eye alone. The rest of this thesis is organized as follows. Chapter 2 gives a detailed overview of the dynamics of the heart during fibrillation and is also accompanied by an enumeration of the different mechanisms of spiral wave breakup. Chapter 3 includes the model that was used as a basis to generate data corresponding to the above mechanisms for the application of metrics that we developed and also covers the methods that were employed to track spiral waves and implement boundary conditions. Chapter 4 is a detailed introduction to the metrics that we developed in an attempt to classify breakup mechanisms and Chapter 5 shows the results of applying these metrics to various data sets. Chapter 6 encompasses the validation process that was used to measure the robustness of our metrics. Chapter 7 includes a short summary of the usefulness of these metrics along with the limitations and future work that accompany this research.

Chapter 2

Overview

Before we move on to the complexities of ventricular fibrillation, we review some of the basic concepts of the heart. This chapter is organized into two sections. The first section gives a background on the electrical waves in the heart, their functions and how reentrant waves are generated. The technicalities of action potential duration and conduction velocity are also included in this section. The subsequent section enumerates some of the proposed mechanisms behind spiral wave breakup.

2.1 Background

2.1.1 Dynamics of the Human Heart

The heart is one of the most vital organs of the body and its main purpose is to supply blood to the lungs and the rest of the body. It consists of 4 chambers—the right and left atria that form the upper chambers and the two ventricles that form the lower chambers. It consists of an elaborate electrical system which generates the electrical impulses that are responsible for the heartbeat. The main components of this system are the sinoatrial (SA) node that is located in the right atrium, the atrioventricular (AV) node located in between the atria and ventricles, and the His-Purkinje system found along the walls of the ventricles. The SA and AV nodes are characterized by a structure of cells wherein the SA produces the electrical signal which is then funneled through the AV node

from the atria to the His-Purkinje system and ventricles. One entire heartbeat is constituted of the following events. First, the electrical signals originate from the SA node and travel through the atria, causing them to contract and consequently pump blood into the ventricles. At this point, the ventricles are completely relaxed while the atria pump blood into them. This constitutes the diastolic phase of cardiac activity or is simply referred to as diastole. Next, these signals reach the AV node where they slow down in order to facilitate the filling of the ventricles with blood. Once this is achieved, the signals travel through another organization of muscle cells called the bundle of His (of the His-Purkinje network) from where they cause the ventricles to contract and pump blood to the rest of the body. This constitutes what is known as systole. Following this, the ventricles go back to their original state before the contraction so that they may be refilled with blood and the entire process is repeated for a new heartbeat [7]. As mentioned in the introduction, during ventricular fibrillation there is a lack of co-ordination between these electrical signals, which leads to the inefficient pumping of blood. When the normal flow of these signals is disrupted, the exact cause for which is still not known, instead of initiating the normal contraction of ventricles, these chaotic impulses cause the ventricles to twitch or quiver irregularly, due to which blood is not pumped efficiently to the body. This causes the blood pressure to drop and due to the blood supply being cut off, there is a lack of oxygen in the cells of the body. The situation usually escalates rapidly, resulting in either unconsciousness or sudden cardiac death or both.

2.1.2 Action Potential and Ion Channels

The cardiac action potential is an essential component in the electrical system of the heart. It is an event that involves a change in the membrane potential of the cardiac cells, that follows a certain trajectory. Movement of ions across the cell membrane gives rise to an action potential. The cardiac cells are coupled to form a tissue through which the action potential propagates as wave. When the cardiac cells are electrically stimulated, the electrical response produced by them describes the action potential which responds to any changes in the heart rate and maintains consistency between the various ionic interactions that take place during the normal functioning. Several ionic channels are located on the cell membrane of the cardiac cells, that allow ions to move across them.

The influx or efflux of ions through the cell membrane is determined by the sign of the difference between the equilibrium potential and the membrane potential. This movement of ions across the membrane generates the electrical signals within the heart. There are many different ion channels present, of which the most important are the sodium, potassium and calcium ion channels. The ionic channels are permeable only to specific ions, for example, the sodium channel only conducts sodium ions. This selective permeability gives rise to the different phases of the action potential. Depending on the difference between the equilibrium potential and the membrane potential, either depolarization (influx of positive ions into the cell) or repolarization takes place (efflux of ions). If the channels are voltage-gated, then their gating mechanism, which in this case is dependent on the voltage, enables them to open up the channel during depolarization so that ions can move into the cell and drives them to close the channel during repolarization [12]. The action potential can be characterized by 5 phases as shown in Figure 2.1. Phase 0 consists of rapid depolarization, also known as the upstroke. In this phase, the sodium channels open under the influence of an electrical stimulus and there is an influx of positive sodium ions into the cell causing the membrane potential to shift to a positive value. Phase 1 consists of early rapid repolarization. During this phase, there is an efflux of potassium ions, which causes the change in the shape of the action potential. In Phase 2, the calcium channels open leading to an influx of calcium ions into the cell. The rate of repolarization decreases during this phase, subsequently extending the refractory period and it is also commonly referred to as the "plateau" phase. Phase 3 is the final rapid repolarization phase before the cell enters Phase 4, the diastolic phase. In this phase, the cell returns to its resting membrane potential and there is no exchange of ions across its membrane. From this phase, once again the application of an eletrical stimulus causing the opening of the sodium channels, will trigger the whole process to repeat [12].

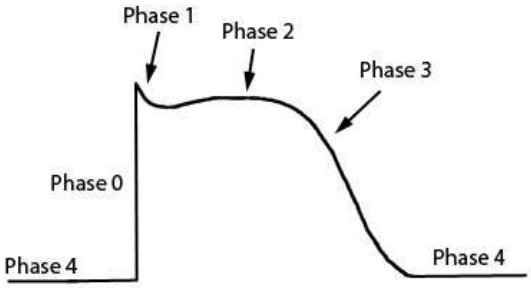

Figure 2.1: Phases of Action Potential. Figure from Ref [13].

2.1.3 Reentrant Waves

The cardiac action potential is responsible for the various electrical chracateristics of the heart that triggers the contraction of the ventricles and the subsequent pumping of blood to the rest of the body. When the cardiac cells are electrically stimulated and produce an action potential, they wait for a certain amount of time (refractory period) before another action potential can be produced. If an electrical stimulus produces a second action potential while the tissue is still in recovery from the first wave, then the second potential may not be able to propagate in the direction of the first wave (while the cells in that region of the tissue are in recovery), but the second action potential will propagate towards areas of recovered tissue. When the tissue around the first action potential wave recovers, then the second wave will propagate toward this region curling around it producing reentrant waves. Thus, when the electrical wave from the previous excitation fails to die down and remains in the heart to produce another excitation, it gives rise to reentrant waves. Each of these waves is characterized by a wave front and a wave back as shown in Figure 2.2. Ideally for normal propagation, the wave front and wave back never meet and the distance between them remains constant. This distance, or in other words, the wavelength, can be calculated by the finding the product of the action potential duration (APD) and conduction velocity (CV). The action potential duration (APD) is calculated from the time that the action potential is initiated until the time that the repolarization finishes. The time lapse between two successive action potentials is called the diastolic interval (DI); this corresponds to Phase 4 of the action potential. The speed at which the

action potential propagates is called the conduction velocity (CV).

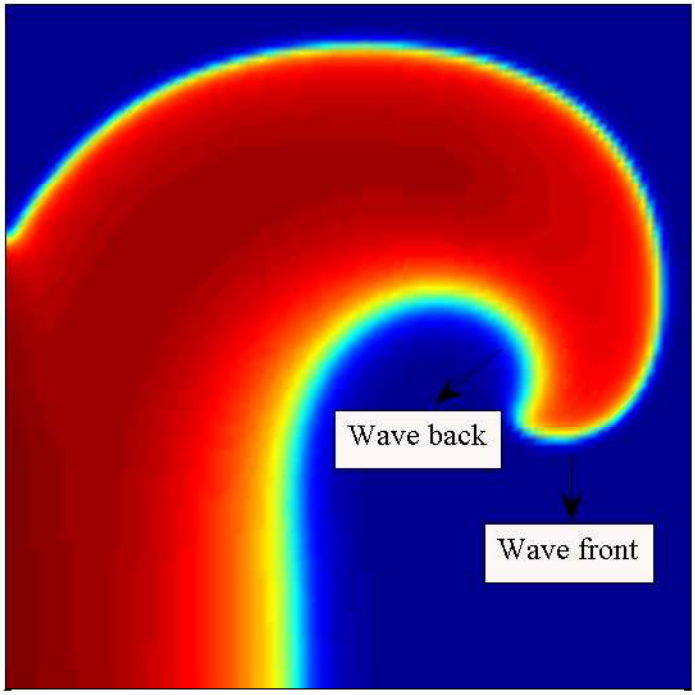

Figure 2.2: Reentrant wave showing the wave front and wave back.

If the wave of excitation is unable to propagate uniformly along the entire wave front, then the wave is just terminated. However, if the obstruction to the wave propagation is more localized, then it paves the way for wave break, which can be characterized by a point where the wave front meets the wave back. This is the main reason behind reentry, as the point where the wave break occurs, makes it a high-curvature point, due to which the remaining portion of the wave rotates around this point. The conduction of the wave is also very slow at the point of high-curvature [14]. This gives rise to spiral-like waves that usually rotate around the obstruction, that led to the wave break. Nevertheless, it is important to note that the obstructions should not be associated with any properties intrinsic to its location, but can arise dynamically. Tissue with various heterogeneities

are more conducive to wave breakup, which implies that scarred tissues in the heart that have resulted from previous heart attacks make the heart more susceptible to fibrillation [15].

2.1.4 Restitution

Restitution describes the relationship between the APD and the preceeding DI. When the heart rate increases, the rate at which the atria pump blood into the ventricles and the subsequent rate at which this blood is pumped to the rest of the body have to remain highly coordinated. In other words, if the systolic duration changes, the diastolic duration would have to be modified too. The main outcome of not having these processes coordinated with each other is that the ventricles would not be completely filled with blood before they contract, and pump blood to the rest of the body. At this point, the ionic processes across the cells would not have completely recovered or repolarization would not have restored the cells to their resting potential before the next action potential is initiated. With the DI being reduced, the next action potential is already initiated but owing to the fact that the cells have only partially recovered from the previous pulse of excitation, the CV is also decreased. It is also important to mention here that the DI has to be of a minimum length in order to support the propagation of pulses; if not, then a smaller DI leads to a partially recovered medium which can pose as a conduction block to the subsequent pulse, possibly leading to breakup [5] [6].

The changes in the action potential duration in relation to the diastolic interval and the changes in the conduction velocity with respect to diastolic interval are usually measured by restitution curves. These curves are called the APD and CV restitution curves, respectively. An APD restitution curve is a graphical description where the APD is plotted against the preceeding DI, as a functional relationship [16]. The slope of this curve is useful in determining how changes in the DI may translate into smaller or larger changes in the following APD [17]. One cycle consists of the action potential and the diastolic interval. When the cycle length is shortened but there is still a constant rate of stimulation, a long APD may be followed by a short DI and similarly a shorter APD by a longer DI. These alternations in the APD give rise to what we call alternans and these alternans are one of the causes of spiral wave breakup. Alternans are the predicted

dynamical state when the restitution curve is steep or has a slope greater than one and signify a steady-state solution losing stability [17]. Similarly, CV restitution curves are obtained by plotting the CV against the preceeding DI. The time lapse between the onset of depolarization (phase 0 of action potential) and the subsequent repolarization to a certain value gives the action potential duration. This value is referred to as a threshold potential which will be seen in the next chapter. The CV is measured by considering two sites that are a certain distance apart and then measuring the difference in times of arrival of the stimulus at the two sites under consideration [18].

2.2 Mechanisms Responsible for Spiral Wave Breakup

From previous studies [19] [2] and simulations we know that spiral waves form the basis for the onset of certain kinds of arrhythmias. From a clinical point of view, it would be helpful to understand exactly which factors contribute to the stability of these spiral waves and also affect their behavior-whether they break up, meander or remain stationary. It has been observed experimentally that ventricular fibrillation can be initiated by one or two reentrant waves that break up into several wave fronts of electrical excitation. These wave fronts can propagate through the ventricular muscle in a very erratic manner and can have varied lifetimes. Improved understanding of the properties of these reentrant waves could make it easier to develop anti-fibrillatory drugs and therapies [20] [21]. Also, it would help in the development of other electrical therapies like anti-tachycardia pacing that can be enforced and which can be useful in curbing the occurrence of some arrhythmias when conditions that are conducive to it are detected [22].

The main cause of spiral wave breakup in 2D is the formation of conduction blocks. When a wave runs into partially refractory tissue, it fails to propagate, thus leading to the formation of new waves. Depending on how these conduction blocks are formed, in principle we may be able to distinguish among the different mechanisms that lead to the breakup. We have selected for examination, a subset of the mechanisms described in [5] . Other mechanisms that are described in the paper require the use of a 3D tissue, which is outside the scope of our present work. We have followed the format prescribed in [5] to describe the mechanisms.

Mechanism 1: Steep APD restitution

It has been found that wave breakup in 2D can be caused by steep APD restitution curves that produce alternations in the action potential duration by a Hopf bifurcation [23] [24] [17]. These steep APD curves have a slope that is greater than one. As mentioned in the previous section, this translates into the fact that any small changes in the diastolic interval (DI) lead to larger changes in the action potential duration. If the subsequent APD is very long, then it can lead to a DI that is below the minimum DI that can support propagation consequently leading to a conduction block. Figure 2.3 is a restitution curve that was generated using the Beeler-Reuter model of cardiac cell electrophysiological processes [25], and shows the development of a conduction block.

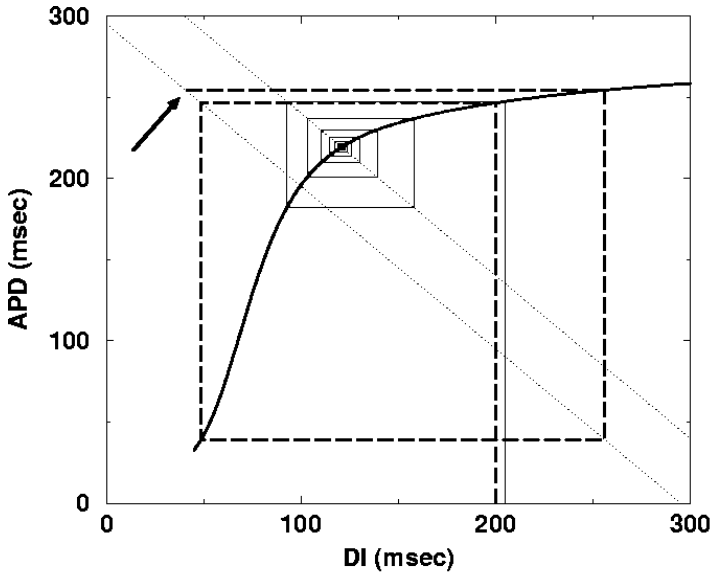

Figure 2.3: APD restitution curve illustrating the oscillations of the APD and the conduction block from Ref. [5].

Figure 2.3 shows the Beeler-Reuter APD restitution curve. In the figure, we can identify a steady state and conduction block. The solid line shows the steady state with an initial DI=205ms and pacing at T=320ms where T represents the cycle length. Starting from the initital DI=205ms, when the curve has a slope greater than one, the system converges to a stable solution (solid lines). On the other hand, the dashed line shows the conduction block (indicated by the arrow) with

DI=200ms and pacing at T=295ms. The period of stimulation is the sum of APD and DI, or, in other words the line defined by the points $(0, T)$ and $(T, 0)$, with a slope of -1. The APD and DI together make up the length of one cycle.

Steep APD restitution curves are responsible for two mechanisms—spiral wave breakup that occurs close to the tip, which we will refer to as steep APD restitution through the rest of this thesis, and breakup that occurs far from the tip which we will be referred to as discordant alternans to avoid any confusion (explained in Section 2.2).

In the case of steep APD restitution, the wave tries to propagate over a medium that is still in recovery. Due to this, the wave front and the wave back travel at different velocities. The wave back travels at a lesser velocity than the wave front and the velocities appear to diverge at a certain threshold. This is the point where the slope of the APD curve is 1. The threshold is important because over time the velocity of the wave back decreases more and more until it reaches a point where it barely moves, as a result posing as a conduction block to the following wave. The formation of the conduction block here is called scalloping. As the wave turns, it runs into its scallop which in this case is formed near the spiral wave tip and this collision results in breakup [5]. An example of this kind of wave breakup is shown in Figure 2.4.

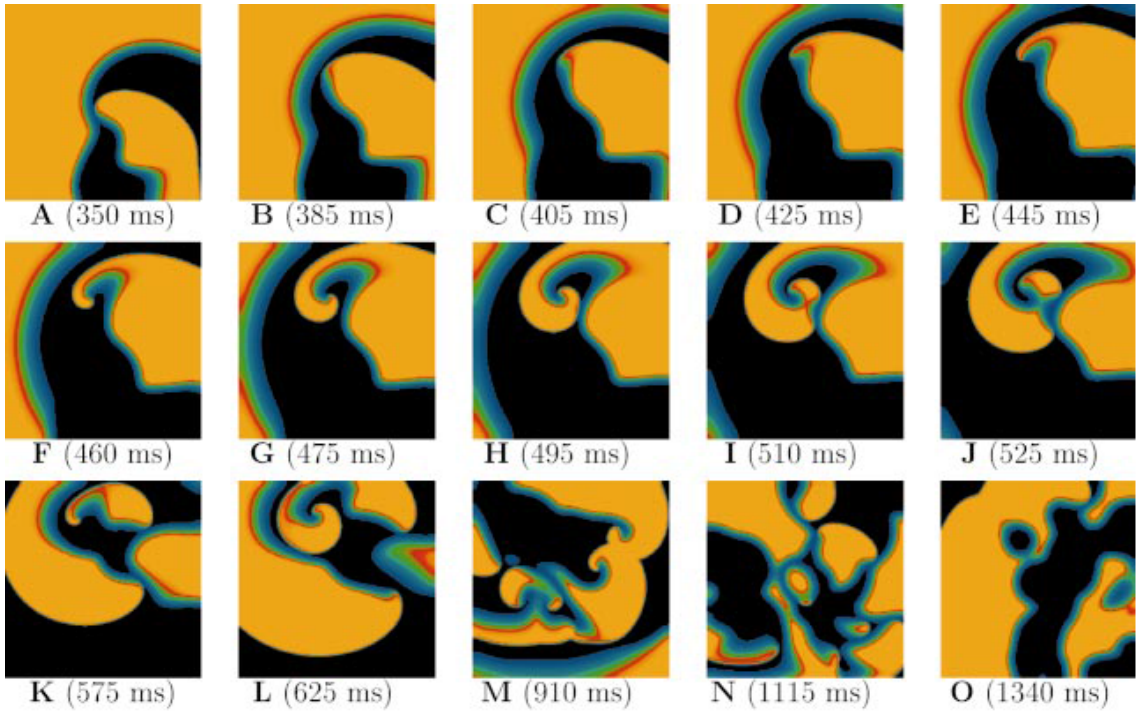

Figure 2.4: Mechanism 1: Steep APD Restitution. From Ref. [5].

Figure 2.4 was generated using parameter set 1 from Table 3.1 with a spatial resolution $\Delta x = 0.025cm$ and time step $\Delta t = 0.25ms$ in a $12.5cm \times 12.5cm$ domain. The figure shows the presence of scallops (regions of refractory tissue) that formed conduction blocks as the wave front collided with them and broke up. Note that the breakup occurred close to the spiral wave tip. The spiral wave first encountered refractory tissue, as seen in the first few panels, and then tried to turn when it reached excitable tissue. Due to the formation of a scallop along the wave back of this moving wave, the wave front ran into this scallop and broke up. This process continued until there were only wave backs present in the system, so that breakup was transient and not sustained.

Mechanism 2: Discordant Alternans

Steep APD restitution curves can also give rise to spiral wave breakup that occurs far from the tip, which we will refer to as discordant alternans. For this mechanism, there is a period of time during which the system is governed by stable APD oscillations; the length of this period is determined

by how steep the curve is. In Section 2.1.4, we explained alternans as alternating APD oscillations. When these alternating APD patterns are seen in the entire domain, with one long APD followed by a short APD in the next beat, they are referred to as concordant alternans. In certain cases, concordant alternans develop into what is referred to as discordant APD alternans. These are spatially discordant, so that the same wave changes from a long wavelength to a short wavelength (or vice versa) as it propagates [26] [27]. The discordant alternans contribute to the increase in the refractoriness of the tissue that develops far from the spiral wave tip which leads to wave break [27]. With each successive beat, the difference in the magnitude of the APDs keeps growing until it reaches a point where the massive difference between the long and short APD leads to the formation of a conduction block [5]. Figure 2.5 illustrates this mechanism of breakup.

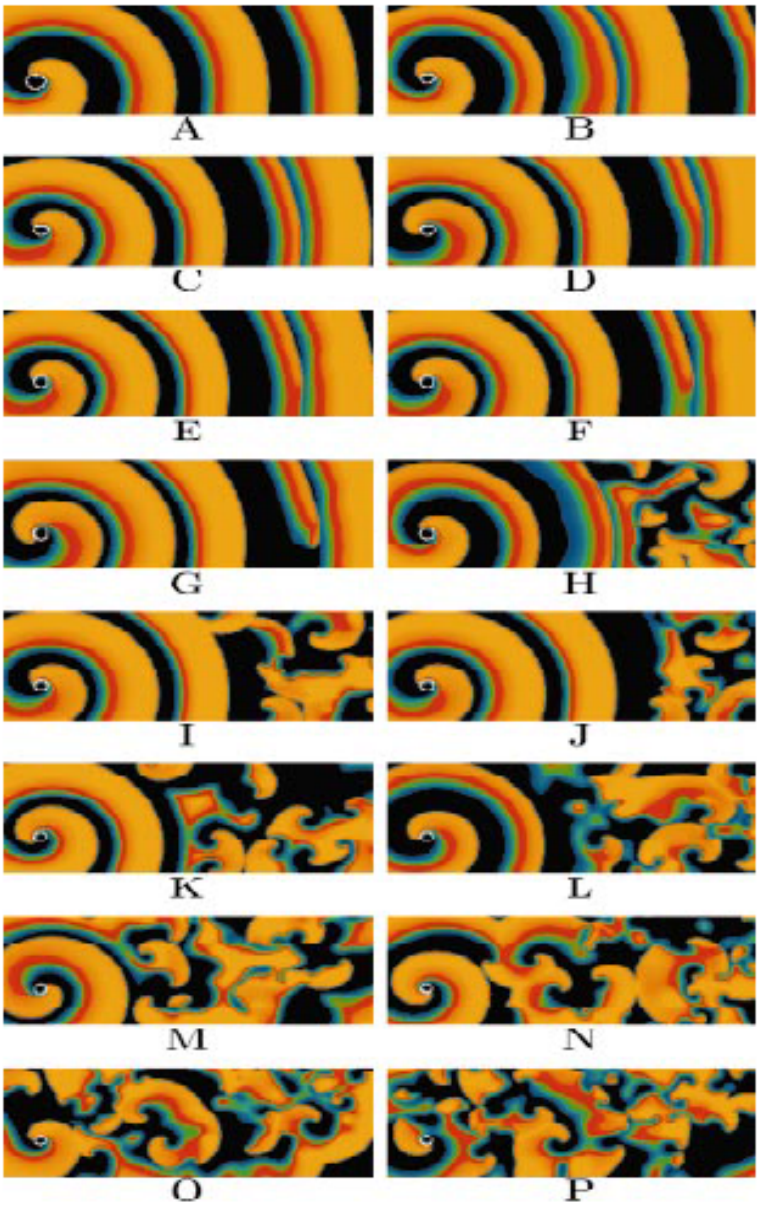

Figure 2.5: Mechanism 2: Discordant alternans. From Ref. [5].

Figure 2.5 was generated using parameter set 2 from Table 3.1 with a spatial resolution $\Delta x = 0.025cm$ and time step $\Delta t = 0.1ms$ in a $30cm \times 12.5cm$ domain. The simulation started off with a stable spiral wave, as seen in Panel A, following which the excitability was increased, the result of which is shown in panels D-G, where a long wavelength was followed by a short wavelength.

Note that the wave exhibited a long (short) wavelength and a little later, and further along in the tissue, it had a short (long) wavelength. The formation of the discordant alternans finally led to the breakup that occured far from the tip seen in Panels H-J. When the excitability was increased further along in the simulation, the higher the value of the excitability, the fewer rotations that the spiral remained intact for before breaking up completely as seen in the next few panels.

Mechanism 3: Bistability

The presence of two stable responses of the system to pacing at a given period depending on how the system arrived at that period is referred to as bistability. When every two pacing beats at a fixed period produces only one action potential, these waves have a longer duration. However, when every beat produces an action potential, the waves have a shorter duration [5].

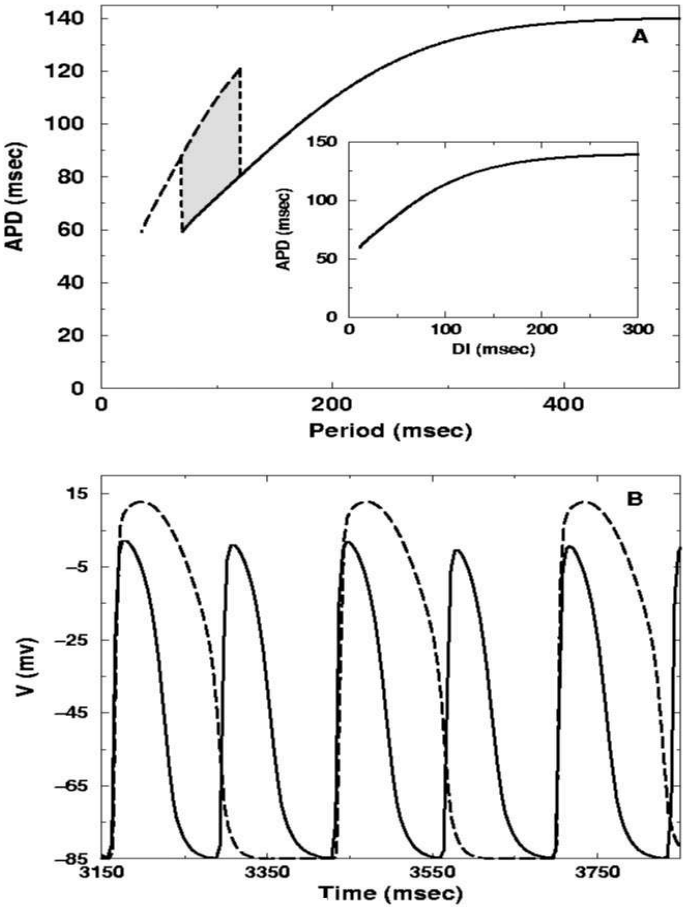

Figure 2.6: Bistability APD restitution curve. From Ref. [5].

When the length of the cycle (APD and DI combined) decreases below a threshold T_{min}, for every two beats, only one action potential is produced, causing the formation of a conduction block (2:1 dashed line in Figure 2.6). This T_{min} is the minimum period that is required for propagation. The conduction block is formed because for a long APD, the tissue remains in a refractory state, making it unable to conduct any incoming impulses. Thus, as the length of the DI increases, so does the APD. If the cycle length is increased such that it is greater than the minimum DI as well as the APD from the 2:1 branch, then it switches back to the 1:1 branch where every beat produces an activation. If the cycle length did not increase that much, then the system would remain in the 2:1 branch. This is what leads to a region of bistability. This difference in the way the system reacts

to any changes in the cycle length is a case of hysteresis. Sometimes, two different regions of the tissue will react differently to an incoming stimulus. A 2:1 conduction block may cause one region of the tissue to not conduct any impulses whereas another part of the tissue that is in recovery state (DI) from a previous wave may conduct any incoming impulses. In a similar fashion, in some cases, for tissue close to the tip, a spiral wave, where the rotation period is smaller, follows the 1:1 branch, but further away it may conduct only every other impulse [5]. An example of this type of breakup is seen in Figure 2.7.

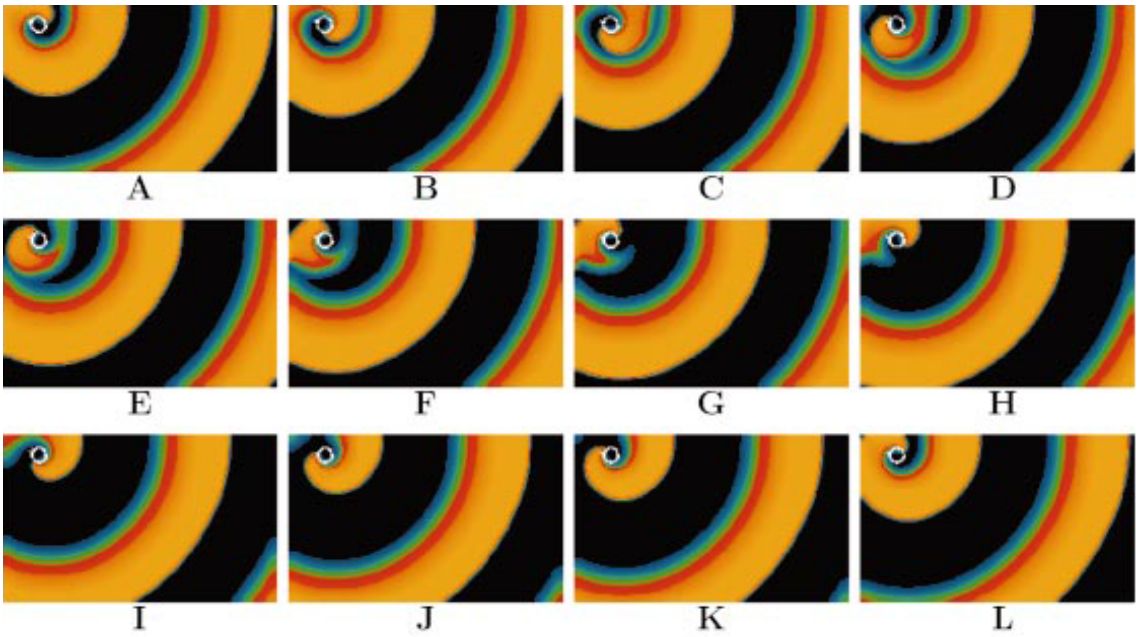

Figure 2.7: Mechanism 3: Bistability. From Ref. [5].

Figure 2.7 was generated using parameter set 3 from Table 3.1 with a spatial resolution $\Delta x = 0.025cm$ and time step $\Delta t = 0.25ms$ in a $16.25cm \times 10cm$ domain. During this simulation, once the spiral wave was initiated, when its period fell in the region of bistability, different parts of the domain conducted the wave differently. In Panels A and B, the regions of the wave near the spiral wave tip moved at the same frequency as the tip; however, away from the tip, the tissue remained quiescent for longer (longer DIs formed away from the tip). As a result, when the wave turned and invaded this region of quiescent tissue, it began to break up as seen in panels D-G. Over the next

few ms, as the new wave was generated, it propagated successfully through the tissue, as shown by panels I-L.

Mechanism 4: Doppler Effect

The Doppler effect is defined as a change in the frequency of a wave that moves with respect to its source. As the spiral wave tip moves, it acts as a moving periodic source of waves. The frequency observed during the Doppler effect is influenced by the type of tip trajectory that is traced out. There are different kinds of tip trajectories that are illustrated in Chapter 3. If we consider the 1:1 branch and 2:1 branch that was explained for bistability, the transition between the two branches can also take place due to the Doppler effect. This happens due to the kind of trajectory traced by the spiral wave tip. For example, if we look at Figure 2.8, a cycloidal trajectory is traced out by the wave, leading to a Doppler shift of the frequency, which can be viewed as a higher frequency in the direction that the tip is moving and a lower frequency behind. These waves with higher frequencies have short rotation periods [5].

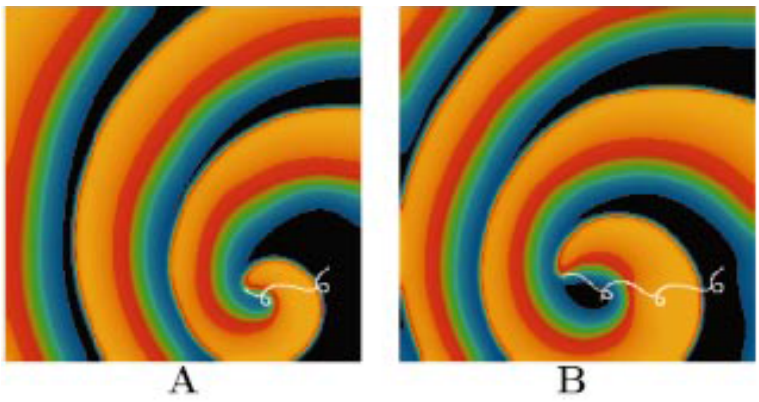

Figure 2.8: Cycloidal trajectory traced by the spiral wave tip. From Ref. [5].

The main idea behind this mechanism is that it produces waves with short rotation periods. This implies that if the waves produced have a period that is greater than the DI_{min}, then propagation of waves is carried out without any formation of conduction blocks. The spiral wave tip trajectories have an influence on the Doppler effect and may result in waves that have a period less than

DI_{min}. If this happens, then there is a shift from the 1:1 to the 2:1 branch, eventually leading to the formation of a conduction block and subsequent wave breakup [5]. The concept of Doppler effect is illustrated in Figure 2.9, which shows how the refractory wave back poses as the conduction block eventually.

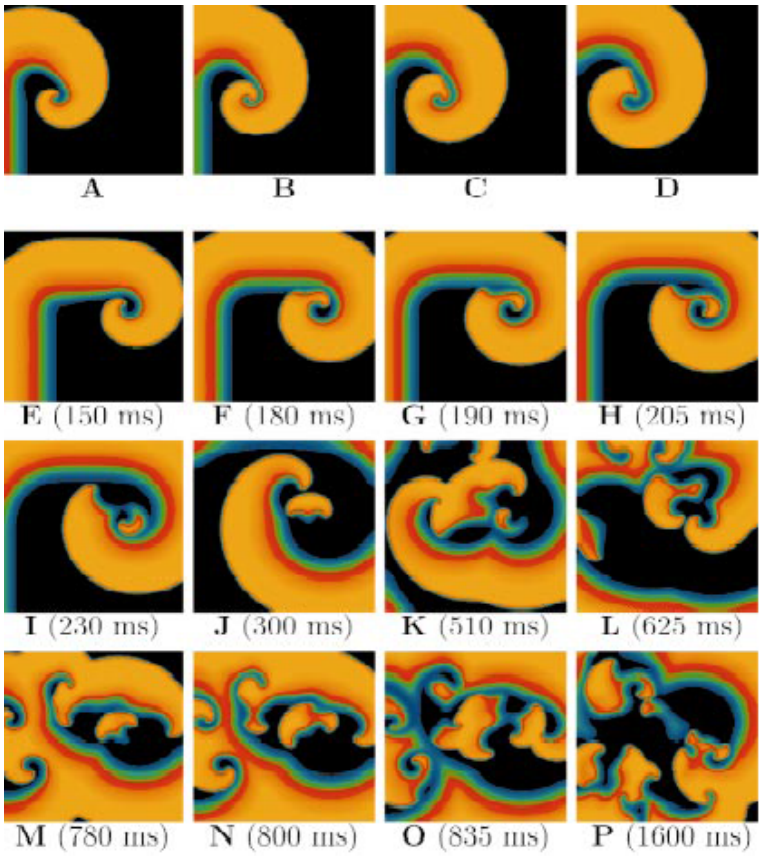

Figure 2.9: Mechanism 4: Doppler Effect. From Ref. [5].

Figure 2.9 was generated using parameter set 3 from Table 3.1 with a spatial resolution $\Delta x = 0.025cm$ and time step $\Delta t = 0.25ms$ in a $11.25cm \times 11.25cm$ domain. As discussed, due to a Doppler effect on the frequency of the wave, during this simulation we observe a wave with a short rotation period that turns too quickly and collides with its own refractory wave back, resulting in breakup, as seen in Panels F-I. The refractory tissue forms a 2:1 conduction block and prevents the propagation of the wave. The new spiral that forms continues to propagate through the recovered

parts of the tissue before the same process is repeated and further breakup takes place as shown in Panels K-N.

Mechanism 5: Supernormal Conduction Velocity

Supernormal conduction refers to the increase in the propagation speed of the action potentials as the cycle length decreases which leads to the propagating pulse catching up with a pulse from the previous cycle [28]. This phenomenon of breakup occurs when extremely fast-moving action potentials collide into one another and start stacking together due to the small diastolic intervals. Thus, they form a conduction block, preventing any further propagation of waves and leading to rapid breakup of the waves. In this case, it is the supernormal conduction that leads to the refractoriness or conduction blocks to be formed in the tissue rather than the steep APD restitution curves. From [28], we can deduce that supernormal conduction disrupts the periodic generation of the action potentials. Due to this concept of supernormality, the waves travel so rapidly that they almost collide with the refractory wave backs, which leads to the development of new secondary waves. The waves that conduct supernormally are usually formed owing to the small diastolic intervals near the spiral wave tip, where most of the breakup occurs.

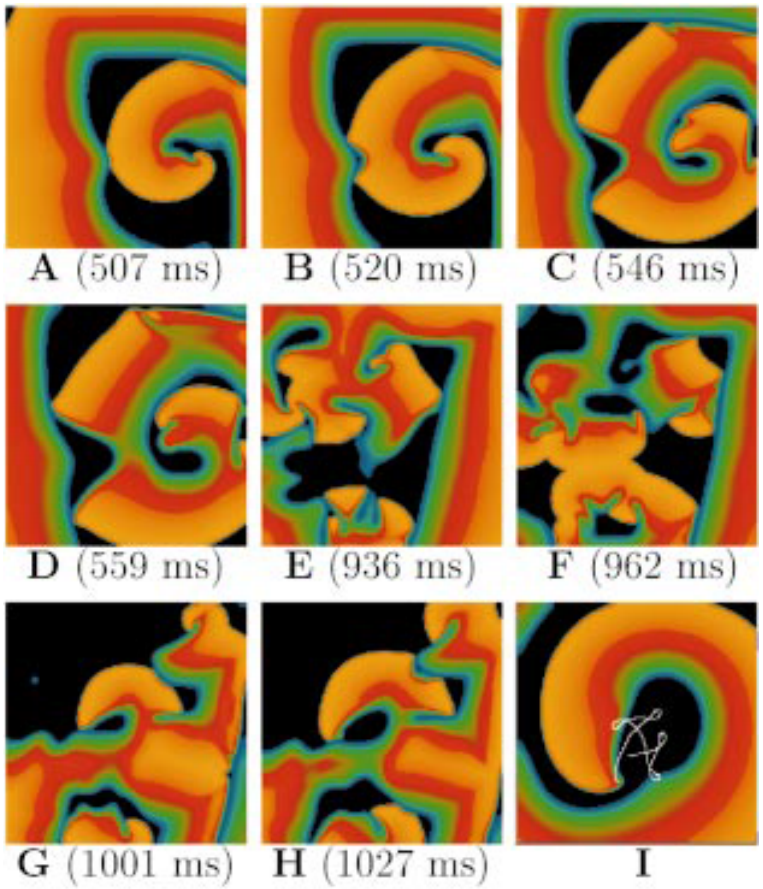

Figure 2.10: Mechanism 5: Supernormal conduction velocity. From Ref. [5].

Figure 2.10 was generated using parameter set 4 from Table 3.1 with a spatial resolution $\Delta x = 0.022cm$ and time step $\Delta t = 0.2ms$ in a $8.85cm \times 8.85cm$ domain. During this simulation, the spirals were observed to turn rapidly as they ran into their own refractory wave backs, leading to wave breakup. This can be seen in Panels A-C. As the simulation continued, the broken waves further propagated at high speeds as they collided with the refractory wave backs of other waves, which can be observed in Panels E-G. The last panel shows a stable wave that was generated using the same parameter set but without the use of supernormal conduction velocity.

Mechanism 6: Periodic Boundary Conditions

The last mechanism considered is periodic boundary conditions. The main reason behinding implementing periodic boundary conditions is to simulate the movement of spiral waves in a cylindrical ventricle, which is a closer approximation of the geometry of the heart than a 2D sheet. The periodic boundary conditions were seen to affect the behavior of the spiral waves mostly in cases where the wavelength was comparable to the perimeter of the domain. Although, normally, no flux or Neumann boundary conditions are used, periodicity was seen to produce breakup in cases where no breakup occurred with no-flux homogenous boundary conditions. In such cases, the spiral wave would be disrupted by the incoming waves generated by itself. In our implementation, we used parameter set 5 from Table 3.1, which showed no breakup when no-flux boundary conditions were applied. The most distinctive feature of this type of breakup is the fact that until the wavelength of the wave is lesser than the perimeter of the domain, we have a stable wave moving around the domain accompanied with various regions of refractory tissue but when this condition no longer exists, the spiral wave begins to collide with incoming waves generated by itself inducing breakup [5]. The periodicity was administered on the right and left boundaries, such that it could emulate a cylindrical ventricle as shown in Figure 2.11.

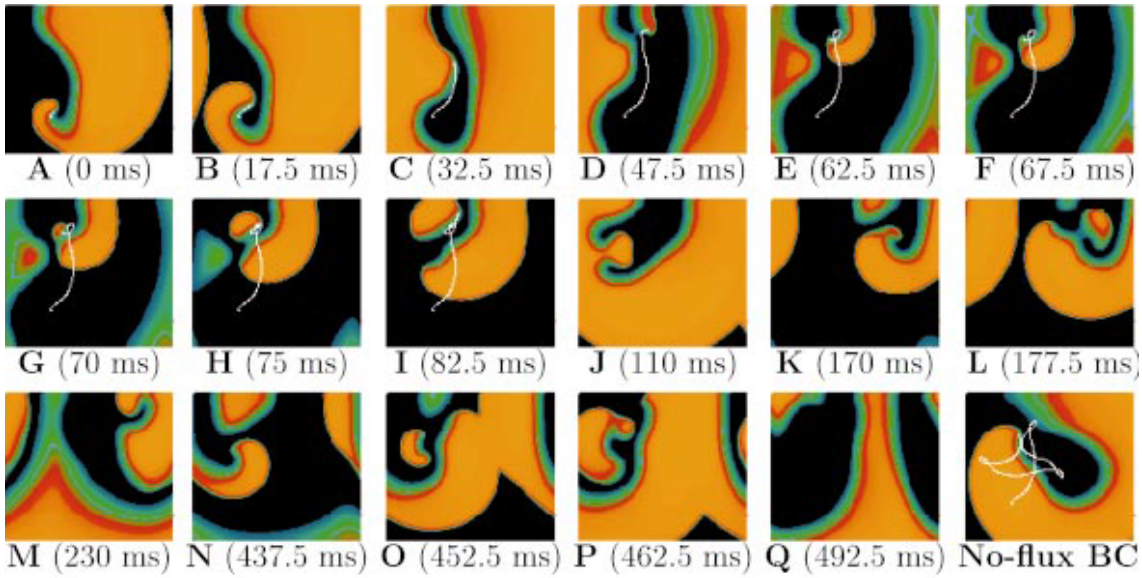

Figure 2.11: Mechanism 6: Periodic Boundary Conditions. From Ref. [5].

Figure 2.11 was generated using parameter set 5 from Table 3.1 with a spatial resolution $\Delta x = 0.0316cm$ and time step $\Delta t = 0.2ms$ in a $7.11cm \times 6.32cm$ domain. The last panel of this figure demonstrates how no breakup occurred when no-flux boundary conditions were implemented for this parameter set. During this simulation, we observed that implementing periodicity created uneven regions of refractory tissue that prevented the propagation of waves, leading to wave break. In the panels C-F, the wave encountered refractory tissue and disintegrated. This process of breakup continued until it terminated, resulting in numerous broken waves that were eventually absorbed by the no-flux boundaries on the top and bottom, as seen in Panel Q.

Chapter 3

Methods

In this chapter, we provide a detailed description of the Fenton-Karma model used here to describe the dynamics of the heart. As mentioned in Chapter 2, there are many different ionic channels present in cardiac cells. This particular model is limited to considering a subset of these and only delves into the details of the sodium, potassium and calcium currents at a phenomenological level. It has been shown previously [5] that the Fenton-Karma model is capable of producing breakup via all the different mechanisms that we intend to study, which forms the main motivation behind using it. The model only includes the minimum set of currents and ionic complexities making it simpler to understand. Another benefit of the model is that it is computationally efficient for large spatial domains. The chapter also includes the numerical methods that were employed to implement this model. The chapter concludes with a description of how to track spiral tip locations over time as well as an overview of the boundary conditions that were implemented for the model.

3.1 Fenton-Karma Model

The main model that has been used throughout this thesis in order to illustrate the complexity of the cardiac cells and to better understand the dynamics of cardiac restitution is the Fenton-Karma model. This model makes it easier to understand the properties of the action potential that was explained in Chapter 2 without delving too far into the ionic complexities of cardiac cells. It

incorporates three basic ionic currents—fast inward (sodium), slow outward (potassium) and slow inward (calcium) currents. The model uses three variables—membrane voltage V, fast ionic gate variable v and slow ionic gate variable w [5] [6].

According to the model, the time rate of change of the transmembrane potential or membrane voltage V is given by the following equation:

$$\partial_t V(x,t) = D\Delta V - (I_{fi}(V,v) + I_{so}(V) + I_{si}(V,w))/C_m, \tag{3.1}$$

where C_m is the membrane capacitance set to $1\mu F/cm^2$ and D is the diffusion coefficient that does not vary spatially. I_{fi} is the fast inward current, I_{so} is the slow outward current and I_{si} is the slow inward current. v and w are the gating variables [5] [6].

The three currents are responsible for the electrophysiological effects in the cells and are discussed in detail below.

- Fast inward current, denoted by $I_{fi}(V;v)$.

  When an excitation or a stimulus that exceeds a threshold is applied to the membrane, the membrane is subsequently depolarized by the fast inward (sodium) current. This current depends on the gating variable v. The gating variable carries out the function of inactivation of the fast inward current after depolarization. This gating variable v is characerized by the Heaviside functions $H(V_c)$ and $H(V_m)$.

$$H(V_c) = \begin{cases} 1, & \text{if } V \geq V_c \\ 0, & \text{if } V > V_c \end{cases} \tag{3.2}$$

$$H(V_m) = \begin{cases} 1, & \text{if } V \geq V_m \\ 0, & \text{if } V > V_m \end{cases} \tag{3.3}$$

  Here, V_c and V_m are the two thresholds that define the range of the membrane potential [5].

  The rate of change of the gating variable v is defined as

$$\partial_t v(x,t) = (1 - H(V_c))(1-v)/\tau_v^-(V) - H(V_c)v/\tau_v^+(V), \tag{3.4}$$

where $\tau_v^-(V) = (1-H(V_m))\tau_{v1}^-(V)+H(V_m)\tau_{v2}^-(V)$. τ_v^+, τ_{v1}^-, τ_{v2}^- correspond to the inactivation and recovery from inactivation time constants for the gating variable v.

The fast inward current is defined as

$$I_{fi}(V,v) = -vH(V_c)(V-V_c)(1-V)/\tau_d, \tag{3.5}$$

where τ_d is the time constant associated with the upstroke.

- Slow outward current, denoted by $I_{so}(V)$.

  This current is used to repolarize the membrane to its resting potential and corresponds to the potassium current. It is further balanced by the slow inward current explained next. This current is given by

$$I_{so}(V) = V(1-H(V_c))/\tau_0 + H(V_c)/\tau_r, \tag{3.6}$$

  where τ_r and τ_0 are the time constants for the slow outward current.

- Slow inward current, denoted by $I_{si}(V;w)$.

  This current is responsible for the plateau in the action potential, by balancing the slow outward current. This current corresponds to the calcium current and it depends on the inactivation gating variable w. This variable, like v, is responsible for the inactivation of the slow inward current [29] [30] [31] [32] [33] [34]. w is defined as

$$\partial_t w(x,t) = (1-H(V_c))(1-w)/\tau_w^-(V) - H(V_c)w/\tau_w^+(V), \tag{3.7}$$

  where τ_w^- and τ_w^+ correspond to the inactivation and recovery from inactivation time constants for the slow gating variable w.

  The slow inward current is given by

$$I_{si}(V,w) = -w(1+tanh(k(V-V_c^{si})))/(2\tau_{si}), \tag{3.8}$$

  where V_c^{si} refers to a threshold potential, τ_{si} is the time constant for the slow inward current, and k is an activation parameter for the the current.

The three currents discussed above form the total membrane current denoted by I_m:

$$I_m = I_{fi}(V; v) + I_{so}(V) + I_{si}(V; w) \tag{3.9}$$

This ionic model simulates the dynamics of the action potential in a more efficient and simplified manner as compared to the more complex mathematical models. With the presence of the three membrane variables and three currents in the model, it incorporates the functions of the transmembrane currents, i.e. sodium, potassium and calcium currents.

Table 3.1 lists the parameter sets that were used in conjunction with the Fenton-Karma model in order to produce the data and figures used in this thesis. This data was obtained directly from Ref. [5] and then a few modifications were made to some of the parameters like τ_d, in order to obtain desired spiral wave patterns. For each of these sets, simulations were carried out for 2000ms including the initiation (of reentrant waves) phase. In some cases, breakup was not sustained for the whole simulation. These included mechanisms like discordant alternans and bistability. Figure 3.1 is a snapshot of the different mechanisms of breakup, that were obtained using the parameter sets in Table 3.1. Both, figures 3.1c and 3.1d, were obtained using parameter set 3. The τ_d values used to produce the two figures were 0.395 and 0.38, respectively.

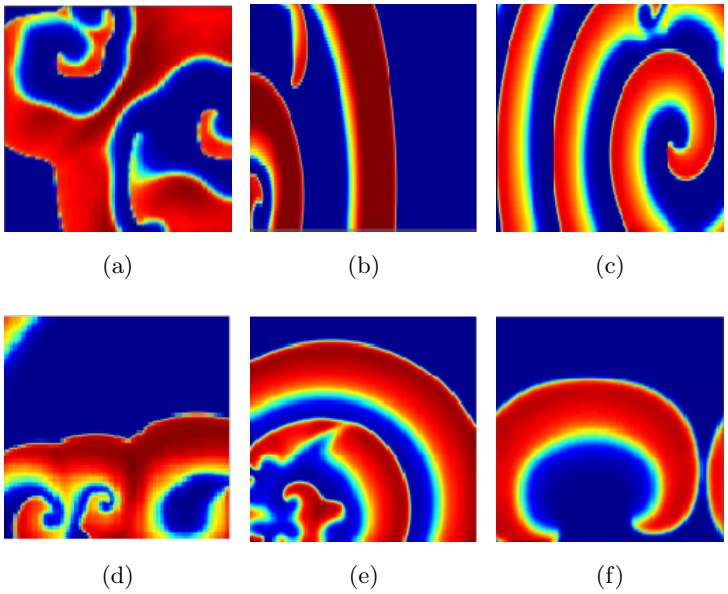

Figure 3.1: Types of Spiral Wave Breakup obtained using parameter sets in Table 3.1. (a)Steep APD restitution (b)Discordant alternans (c)Bistability (d)Doppler effect (e)Supernormal conduction velocity (f)Periodic boundary conditions

Table 3.1: Parameter Sets

Parameter	*Set*1	*Set*2	*Set*3	*Set*4	*Set*5
τ_v^+	3.33	3.33	3.33	3.33	13.03
τ_{v1}^-	19.6	15.6	9	45	19.6
τ_{v2}^-	1250	5	8	2	1250
τ_w^+	870	350	250	670	800
τ_w^-	41	80	60	61	40
τ_d	0.25	0.407	0.395	0.25	0.45
τ_o	12.5	9	9	12.5	12.5
τ_r	33.33	34	33.33	28	33.25
τ_{si}	29	26.5	29	29	29
k	10	15	15	10	10
V_c^{si}	0.85	0.45	0.50	0.45	0.85
V_c	0.13	0.15	0.13	0.13	0.13
V_v	0.04	0.04	0.04	0.05	0.04

3.2 Computational Methods

As seen previously, Eq. 3.1 describes the transmembrane potential. The three variables were discretized on a uniform mesh and were integrated using a semi-implicit Alternating Direction Implicit(ADI) method derived from the Crank-Nicholson scheme. For each parameter set, we selected appropriate spatial and temporal resolutions that differed from one set to the next. We will first look at the ADI method briefly before moving on to its application to our partial differential equations.

3.2.1 Alternating Direction Implicit Method

The Alternating Direction Implicit (ADI) method is a finite-difference method used to numerically solve partial differential equations. Its most common application is to solve parabolic, hyperbolic

and elliptic PDEs. Given an equation, finite differences are used to replace any derivatives and boundary conditions appearing in the equation, following which the equation is substituted with a set of linear equations [35]. We start off with some basic definitions to understand ADI. If $u(x, y)$ is a function of two variables x and y where $u_{i,j}$ represents the value of $u(x, y)$ at (i,j), then we have the following:

- Forward Difference Formula
$$u_x = \frac{u_{i+1,j} - u_{i,j}}{h} \tag{3.10}$$
- Backward Difference Formula
$$u_x = \frac{u_{i,j} - u_{i-1,j}}{h} \tag{3.11}$$
- Centered Difference Formula
$$u_x = \frac{u_{i+1,j} - u_{i-1,j}}{2h} \tag{3.12}$$

In the above case, h represents the spatial resolution in the x-direction.

Similarly, for the Y-direction,

- Forward Difference Formula
$$u_y = \frac{u_{i,j+1} - u_{i,j}}{k} \tag{3.13}$$
- Backward Difference Formula
$$u_y = \frac{u_{i,j} - u_{i,j-1}}{k} \tag{3.14}$$
- Centered Difference Formula
$$u_y = \frac{u_{i,j+1} - u_{i,j-1}}{2k} \tag{3.15}$$

In the above case, k represents the spatial resolution in the y-direction.

We can also apply finite difference approximations to higher-order derivatives and differential operators. The second-order partial derivatives of u are defined as:

$$u_{xx} = \frac{u_{i-1,j} - 2u_{i,j} + u_{i+1,j}}{h^2} \tag{3.16}$$

$$u_{yy} = \frac{u_{i,j-1} - 2u_{i,j} + u_{i,j+1}}{k^2} \tag{3.17}$$

$$u_{xy} = \frac{1}{4}[u_{i+1,j+1} - u_{i+1,j-1} - u_{i-1,j+1} + u_{i-1,j-1}] \tag{3.18}$$

The ADI method is often used to solve the diffusion equation. We will now define the ADI method applied to the diffusion equation below.

$$\frac{\partial u}{\partial t} = \left(\frac{\partial^2 u}{\partial x^2} + \frac{\partial^2 u}{\partial y^2}\right) = u_{xx} + u_{yy} = \Delta u \tag{3.19}$$

Applying the ADI method to equations such as Eq.3.19 has many advantages. At each step, the set of equations that has to be solved is simple, and in the course of solving it, a tridiagonal matrix is obtained. The computational complexity of solving tridiagonal matrices is considerably lesser than solving by Gaussian elimination, which makes them more efficient. The ADI method has been shown to be unconditionally stable [36]. With the ADI method, two equations are obtained, one with the x-derivative taken implicitly and the other with the y-derivative taken implicitly. Taking a half step in the x-direction and a half step in the y-direction culminates in the full step used alternatively in other difference equations. When equations are solved implicitly, the equations that are solved at time step $n+1$ invlove a combination of known quantities at the time n and unknown quantities at $n+1$. The solutions computed through the implicit method are stable due to the fact that even as the time increases, there is always a solution for the unknown quantities of the $n+1$ period.

For the above diffusion equation, the ADI method is applied to get the following two equations [37].

$$\frac{u_{i,j}^{n+\frac{1}{2}} - u_{i,j}^{n}}{\frac{\Delta t}{2}} = \delta_x^2 u_{i,j}^{n+\frac{1}{2}} + \delta_y^2 u_{i,j}^{n} \tag{3.20}$$

$$\frac{u_{i,j}^{n+1} - u_{i,j}^{n+\frac{1}{2}}}{\frac{\Delta t}{2}} = \delta_x^2 u_{i,j}^{n+\frac{1}{2}} + \delta_y^2 u_{i,j}^{n+1} \tag{3.21}$$

where δ represents the Dirac delta function.

Given,

$$\partial_t V(x,t) = D\Delta V - (I_{fi}(V,v) + I_{so}(V) + I_{si}(V,w))/C_m \tag{3.22}$$

our first step is to define all the partial derivatives using the centered difference formula. The x-axis is indexed with i and the y-axis with j. $\Delta x = \Delta y = \Delta$ are the lattice spacings with n measuring

the time $t = n\Delta t$. We have the following partial derivatives after discretizing the PDE by defining V_α^n where $\alpha = (i, j)$ is the two-dimensional index.

$$\delta_x^2 V_\alpha^n = V_{i+1,j}^n + V_{i-1,j}^n - 2V_{i,j}^n \tag{3.23}$$

$$\delta_y^2 V_\alpha^n = V_{i,j+1}^n + V_{i,j-1}^n - 2V_{i,j}^n \tag{3.24}$$

$$\delta_{xy}^2 V_\alpha^n = \frac{1}{4}[V_{i+1,j+1}^n - V_{i+1,j-1}^n - V_{i-1,j+1}^n + V_{i-1,j-1}^n] \tag{3.25}$$

We now solve the first part of the cable equation,

$$\partial_t V(x,t) = D\Delta V - (I_{fi}(V,v) + I_{so}(V) + I_{si}(V,w))/C_m \tag{3.26}$$

This gives,

$$D\left(\frac{\delta^2 V}{\delta x^2} + \frac{\delta^2 V}{\delta y^2}\right), \tag{3.27}$$

where in cardiac muscle, D is of the order $0.001 cm^2/ms$.

Applying the forward Euler scheme for the purpose of time integration gives

$$\frac{V_\alpha^{n+1} - V_\alpha^n}{\Delta t} = \frac{\delta_x^2 V_\alpha^n}{\Delta x^2} + \frac{\delta_y^2 V_\alpha^n}{\Delta y^2}. \tag{3.28}$$

Using $\Delta x = \Delta y = \Delta$ and making the substitution $\beta = \frac{\Delta t D}{\Delta^2}$, we obtain

$$V_\alpha^{n+1} - V_\alpha^n = \beta[\delta_x^2 V_\alpha^n + \delta_y^2 V_\alpha^n]. \tag{3.29}$$

$\delta_x^2 V_\alpha^n + \delta_y^2 V_\alpha^n$ represents a 2D Laplacian in the x-y plane, to which the 2D ADI scheme is applied. Using a semi-implicit ADI scheme as explained earlier gives,

$$V_\alpha^{n+\frac{1}{2}} - V_\alpha^n = \frac{\beta}{2}[\delta_x^2 V_\alpha^{n+\frac{1}{2}} + \delta_y^2 V_\alpha^n] \Rightarrow V_\alpha^{n+\frac{1}{2}} = V_\alpha^n + \frac{\beta}{2}[\delta_x^2 V_\alpha^{n+\frac{1}{2}} + \delta_y^2 V_\alpha^n] \tag{3.30}$$

$$V_\alpha^{n+1} - V_\alpha^{n+\frac{1}{2}} = \frac{\beta}{2}[\delta_x^2 V_\alpha^{n+1} + \delta_y^2 V_\alpha^{n+\frac{1}{2}}] \Rightarrow V_\alpha^{n+1} = V_\alpha^{n+\frac{1}{2}} + \frac{\beta}{2}[\delta_x^2 V_\alpha^{n+1} + \delta_y^2 V_\alpha^{n+\frac{1}{2}}]. \tag{3.31}$$

The two equations above are identical and are solved by alternatively incrementing x and y implicitly every two time steps. At each iteration, an equation of the form $LV = R$ is solved, L being a tridiagonal matrix, V being an unknown vector and R being a known vector [6]. Similar to the Crank-Nicholson scheme, a second order Adams-Bashforth scheme is used to solve for the membrane currents in Eq. 3.1 [6].

3.3 Spiral Tips and Tip Locations

Several methods have been employed to identify spiral wave tips. In our implementation, we use a method which involves first finding an isopotential line and then identifying the points with zero normal velocity on it [6]. An isopotential line is defined as a line that has a constant membrane potential. Thus, a spiral tip would be identified at points where the depolarization wave front meets the repolarization wave back, the boundaries between which are marked by an appropriate isopotential line. In our problem, after identifying an isocontour of the transmembrane potential, the next step was to find a point on it where the time derivative is zero [6] [12] [18] [38] [39].

As described by Fenton et al. in [6], this is the procedure that is followed to find a spiral tip. Let V_{iso} denote an isopotential line such that $V(\mathbf{x}, t) = V_{iso}$ and $\mathbf{x}$ represents the position vector which separates the depolarized region of the tissue from the repolarized region. Thus, in order to look for a spiral tip, which is a point of zero normal velocity, the intersection point of the lines $V = V_{iso}$ and $\partial_t V = 0$ with $\mathbf{x}$ is identified such that

$$V(\mathbf{x}, t) - V_{iso} = \partial_t V(\mathbf{x}, t) = 0 \tag{3.32}$$

This denotes the point where the excitation wave front meets the repolarization wave back of the action potential. The V_{iso} value that was used in our implementation was 0.55.

The shapes traced out by the spiral wave tips are often useful in studying the stability of spiral waves. Several factors determine the shape traced out by these tips. Some of them include the threshold of excitation, wavelength of the spiral waves, radius of curvature and the duration between depolarization and repolarization, to name a few. Figure 3.2 shows some of the trajectories traced out by the spiral wave tips that include circular, epicycloidal, cycloidal, hypocycloidal, hypermeandering and linear trajectories [5] [40] [41] [42].

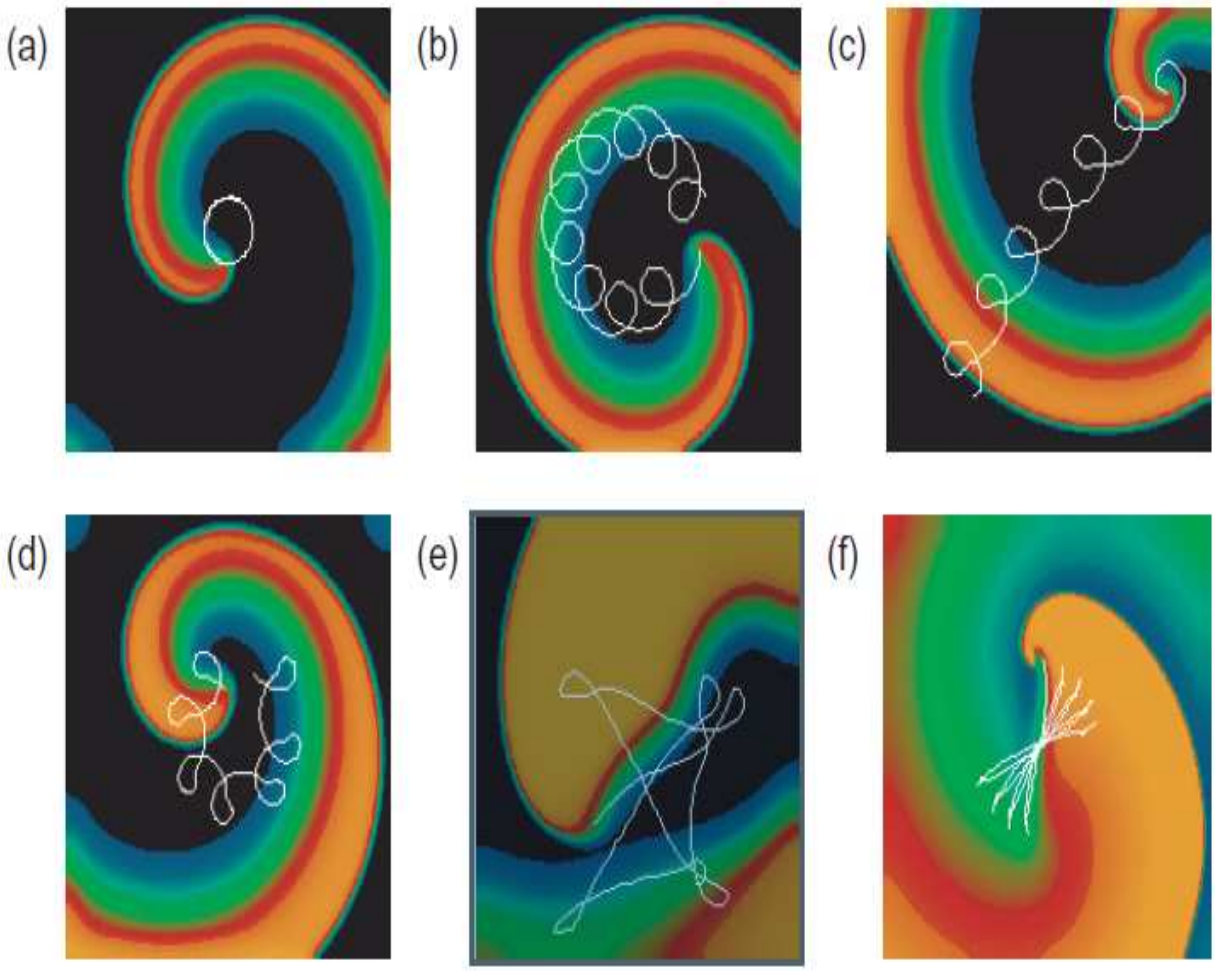

Figure 3.2: Types of tip trajectories: (a) circular (b) epicycloidal (c) cycloidal (d) hypocycloidal (e) hypermeandering and (f) linear. From Ref. [43].

3.4 Boundary Conditions

Boundary conditions (BC) can have a significant effect on the behavior of spiral waves. In our implementation of the Fenton-Karma model, homogenous Neumann boundary conditions were used to enforce a rigid boundary and prevent any leak of currents. They are also referred to as no-flux boundary conditions, since the main requirement that is implemented by these BC is that the flux is zero on the boundaries. This would translate into the following:

$$\frac{\partial V}{\partial x} = 0 \text{ on the right and left side boundaries,} \tag{3.33}$$

$$\frac{\partial V}{\partial y} = 0 \text{ on the top and bottom boundaries.} \tag{3.34}$$

Similarly, for the implementation of periodic boundary conditions, homogenous Neumann boundary conditions were retained in the x-direction, and periodicity was administered in the y-direction to emulate a cylindrical ventricle. So, if the solution domain is characterized by $u(0 : nx+1, 0 : ny+1)$ such that there are $nx * ny$ points in our solution domain, for the y-direction to be periodic the conditions $u(1, j) = u(nx, j)$ and $u(0, j) = u(nx-1, j)$ would be enforced, where $j \in (1, ny)$. In this case, the points along the lines $x = 0$, $x = nx + 1$, $y = 0$ and $y = ny + 1$ represent the ghost/buffer points.

Chapter 4

Metrics and Implementation

This chapter is an introduction to the metrics that we believed could effectively capture the dynamics of the heart undergoing fibrillation and allow us to differentiate among spiral wave breakup mechanisms. From a mathematical point of view, knowing that spiral wave breakup is often considered to be a chaotic process aided us in choosing metrics such as Lyapunov exponents, which are often used to quantify the chaos in a system. In addition to this, measuring the linear and non-linear dependencies in a system is often served by computing the mutual information and correlation for the various spatial points in the domain under consideration, the results of which indicate how much information is shared within the system and demonstrate the existence of any sort of deterministic relationship accompanied by how these dependencies may change over time. This chapter also includes other metrics that are more specific to our problem, some of which are measuring the number of spiral waves, the speed of the spiral wave tips as well as properties such as the birth rate, death rate and spiral wave lifetimes. These properties are computed to determine whether they are more indicative of the mechanism under consideration.

4.1 Number of Spiral Waves

We calculated the number of spiral waves by computing the spiral wave tip locations over time. As explained in Chapter 3, spiral tips were identified at points where the depolarization wave front met

the repolarization wave back. The coordinates of each of these spiral tips were recorded for every time step such that for every time step we had a set of 2D coordinates representing all the spiral waves that were in existence. We then found the number of coordinate pairs written, which was the number of spiral waves in existence for each time step. The time step chosen in all the simulations was 0.25ms. This number was then plotted against time to illustrate how the distribution changed over time.

4.2 Lyapunov Exponents

The electric signals derived from a heart undergoing ventricular fibrillation are very chaotic and complex, making it difficult to derive any form of significant spatiotemporal organization. A significant measure of this chaos can be found by the calculation of the largest Lyapunov exponent for the system. According to Devaney [44], a dynamical system is said to be chaotic if it displays long-term aperiodicity and a sensitive dependence to initial conditions. In addition to this, a dynamical system may also be chaotic if it has a positive Lyapunov exponent. Lyapunov exponents in the simplest terms are a measure of how two orbits that start with almost the same initial conditions differ over time. The separation between the orbits would grow over time if there is a positive exponent. This definition can be explained using Figure 4.1.

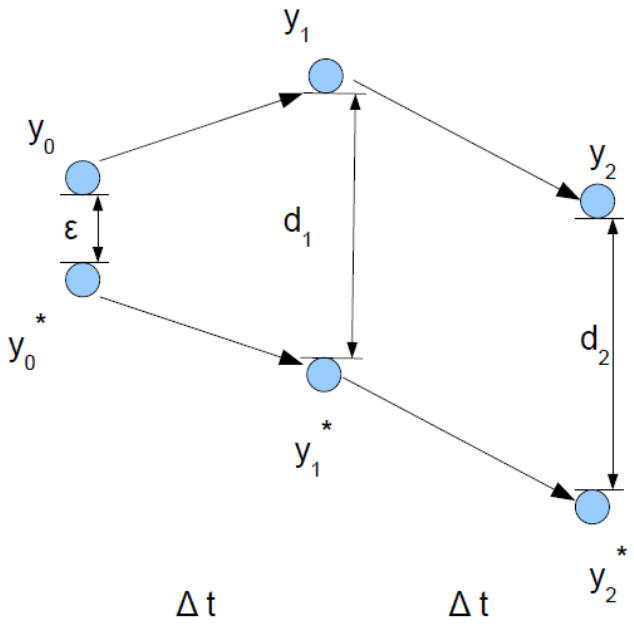

Figure 4.1: Divergence of orbits over time. From Ref [45].

As shown, we start off with two orbits y_0 and y_0^* that are initially separated by ϵ. After an iteration, the perturbed orbits y_1 and y_1^* are at a distance of d_1 from each other. Similarly, after a second iteration they are at a distance d_2 apart. If the system is governed by a positive Lyapunov exponent, then the separation between the two orbits grows over time, whereas if the system had a negative exponent, a periodic cycle or an attracting fixed point would be observed [45]. The reason Lyapunov exponents are usually used is because they are not only an indicator of chaos in the system but also a measure of the level of chaos. If we consider two trajectories that are separated by a very small distance which is denoted by the vector $\delta X(0)$, then after some time t the separation between these trajectories can be written as

$$\| \delta X(t) \| = e^{\lambda t} \| \delta X(0) \| . \tag{4.1}$$

In Eq. 5.1, $\delta X(t)$ is the separation vector of the state vectors of the two trajectories and λ is the Lyapunov exponent that changes over time. As seen above, the Lyapunov exponent represents the average exponential rate of divergence or convergence for two infinitesimally close orbits. For our

discrete system, the Lyapunov exponent is defined as

$$\lambda_i = \lim_{N\to\infty} \frac{1}{N} \sum_{n=1}^{N} \log \frac{x_i(n+1)}{x_i(n)}. \tag{4.2}$$

In summary, for a system with a value of zero for the Lyapunov exponent, the system is said to be in a steady state and exhibits Lyapunov stability. For non-zero Lyapunov exponents, the more negative the exponent is, the higher is the stability demonstrated by the system, and for a system with a positive exponent, the more unstable and chaotic the system is. Below, we have described the algorithm that was used to compute the exponent for our system [46]. The main steps involved were the following.

1. Select any two points separated by d_0.

2. Iterate both the orbits by one step and calculate their new separation, which is denoted as d_1. The separation is calculated as

$$d_1 = \sqrt{(x_1 - x_2)^2 + (y_1 - y_2)^2}. \tag{4.3}$$

   The subscripts above denote the two orbits whose separation is being calculated.

3. Calculate $\log \frac{d_1}{d_0}$.

4. Restore one of the orbits so that they are back to a separation of d_0 and in the same direction as d_1, as we wish to calculate the average rate of convergence or divergence.

5. Repeat the above steps and finally calculate the average of the values obtained in Step(3). This gives the largest Lyapunov exponent for the system [47].

In our implementation of calculating the largest Lyapunov exponent, we start off with data consisting of the voltage values over the entire domain, over time. Since the calculation of the Lyapunov exponent over the entire range of values is not computationally feasible (especially not for the type of experimental system to which we hope to apply our results), the exponent is computed for a subset of spatial points taken from the whole tissue we are examining. The points were selected from the boundaries and the centre of the domain so as to cover the entire region of

the 2D sheet. After the initial sampling, one point is set as the reference and we then iterate over the remaining range to find which point is the closest to the point of reference. Once this is found, we renormalize along the line between the two previous points. Calculating the average logarithmic rate of separation is the next step in the process, which eventually gives the maximum Lyapunov exponent for the system.

4.3 Mutual Information

Mutual information is used to measure the statistical dependence between two variables, x and y, to quantify to what degree knowing the value of x reduces the uncertainty in the value of y or vice versa [48]. It mainly gives the non-linear relationship between two random variables—in other words, how much information one random variable holds about another. Since the calculation of mutual information mostly involves the concept of entropy, in such a case entropy would signify the information that a random variable holds of itself. In addition, mutual information, which quantifies the distance between two random variables, is a form of relative entropy. Calculating the mutual information in the case of ventricular fibrillation (VF) would help in understanding its underlying spatial organization, which is known to be very complex. Cover and Thomas provide us with the following definitions, which highlight the relationship between mutual information and entropy [49].

4.3.1 Entropy

We begin by defining entropy, which quantifies the uncertainty of a random variable X.

Let X be a discrete random variable with a probability mass function

$$p(x) = Pr\{X = x\}, x \in \chi. \tag{4.4}$$

Thus, the probability mass functions for two discrete random variables X and Y are denoted by $p(x)$ and $p(y)$.

The entropy H(X) of a discrete random variable X is defined as

$$H(X) = -\Sigma_{x\in\chi} p(x) \log_2 p(x). \tag{4.5}$$

The entropy is a functional of the distribution of X. It is only related to the probability of X and not the actual values taken by X.

4.3.2 Joint Entropy

Joint entropy quantifies the amount of information shared between two discrete random variables X and Y. The joint entropy H(X,Y) of two discrete random variables X and Y which have a joint distribution $p(x, y)$ is defined as

$$H(X, Y) = -\Sigma_{x\in\chi}\Sigma_{y\in\Upsilon}p(x, y)\log p(x, y). \tag{4.6}$$

According to the chain rule of conditional entropy which can be used to find the relationship between the entropy and joint entropy,

$$\begin{aligned} H(X, Y) =& -\Sigma_{x\in\chi}\Sigma_{y\in\Upsilon}p(x, y)\log p(x, y) \\ =& -\Sigma_{x\in\chi}\Sigma_{y\in\Upsilon}p(x, y)\log p(x)p(y|x) \\ =& -\Sigma_{x\in\chi}\Sigma_{y\in\Upsilon}p(x, y)\log p(x) - \Sigma_{x\in\chi}\Sigma_{y\in\Upsilon}p(x, y)\log p(y|x) \\ =& -\Sigma_{x\in\chi}p(x)\log p(x) - \Sigma_{x\in\chi}\Sigma_{y\in\Upsilon}p(x, y)\log p(y|x) \\ =& H(X) + H(Y|X). \end{aligned} \tag{4.7}$$

4.3.3 Mutual Information

Let X and Y be two discrete random variables with a joint probability mass function $p(x, y)$ and marginal probability mass functions $p(x)$ and $p(y)$. The mutual information $I(X; Y)$ is the relative entropy between the joint distribution and the product distribution $p(x)p(y)$, i.e.,

$$I(X; Y) = \Sigma_{x\in\chi}\Sigma_{y\in\Upsilon}p(x, y)\log\frac{p(x, y)}{p(x)p(y)}. \tag{4.8}$$

4.3.4 Relationship between Entropy and Mutual Information

The mutual information $I(X; Y)$ can be rewritten as

$$I(X; Y) = \Sigma_{x,y}p(x, y)\log\frac{p(x, y)}{p(x)p(y)}$$

$$
\begin{aligned}
&= \Sigma_{x,y} p(x,y) \log \frac{p(x|y)}{p(x)} \\
&= -\Sigma_{x,y} p(x,y) \log p(x) + \Sigma_{x,y} p(x,y) \log p(x|y) \\
&= -\Sigma_{x} p(x) \log p(x) - (-\Sigma_{x,y} p(x,y) \log p(x|y)) \\
&= H(X) - H(X|Y). \qquad (4.9)
\end{aligned}
$$

The mutual information $I(X;Y)$ is the reduction in the uncertainty of X due to the knowledge of Y. By symmetry, we have,

$$I(X;Y) = H(Y) - H(Y|X). \qquad (4.10)$$

Since $H(X,Y) = H(X) + H(Y|X)$, we obtain,

$$I(X;Y) = H(X) + H(Y) - H(X,Y). \qquad (4.11)$$

Also note that

$$
\begin{aligned}
I(X;X) &= H(X) - H(X|X). \\
&= H(X) \qquad (4.12)
\end{aligned}
$$

Eq. 4.11 is applied to derive the mutual information for our system. We start off with a discretized spatial domain that has a record of the voltage values V_m measured every Δt ms. Once again, for computational purposes, only a sample of points in the domain is considered to give us a broad view of how much information is shared between various parts of the domain. The mutual information values derived for the system are scaled between the values of 0 and 1 for ease of comparison of the results obtained in Chapter 5, for each of the different mechanisms, as we are not concerned with the actual values of mutual information, but rather how the information shared changes over time. To track the change of information over time, the total duration of the simulation is also divided into four subsets. Doing so reveals which time interval has the most information being shared. We try to relate this to the kind of breakup that occurs and the related mechanism that is responsible for the breakup. A plot of this mutual information shows which parts of the domain share the most information and when. Values of mutual information closer to 1 indicate a high amount of mutual information shared between spatial points and values of

information closer to 0 indicate less information shared between spatial points in the domain. It would be expected that the time steps with the most breakup, is exhibited to lead to a more chaotic environment and in general, would have spatial points that do not share much information, making them largely independent of each other.

4.4 Spatial Correlation

The extent of spatial organization of ventricular fibrillation is a basic attribute of an arrhythmia. Measuring the spatial organization can also be used to trace any patterns in how the arrhythmia progresses over time. The change in the correlation observed between measurements is also used to outline the spatial organization of the system, which has been shown to be an effective way of characterizing the behaviour during ventricular fibrillation. Bayly et al gives us the following formulation that can be used to calculate the cross-correlation [50].

In order to calculate the correlation we make use of the cross-correlation function R that is measured for a signal at two locations, x_i and x_j. The number of samples in the time series is signified by M. The time lag is a multiple of the sampling interval $\tau = k\Delta T$.

$$R(\tau; x_i, x_j) = \frac{1}{M-k} \sum_{m=1}^{M-k} f(x_i, t_m) f(x_j, t_m + \tau) \tag{4.13}$$

The cross-correlation function is then normalized to a range from 0 to 1 as shown below.

$$R(\tau; x_i, x_j) = \frac{R(\tau; x_i, x_j)}{\sqrt{R(0; x_i, x_i) R(0; x_j x_j)}} \tag{4.14}$$

Applying the above formulation to our problem produces a plot that exhibits the complexity of the spatial organization as well as how the correlation between the V_m time series changes over time [50] [51]. We begin with a discretized spatial domain that has a record of V_m values for each time step. The total duration of the simulation is once again divided into four subsets in order to track how the correlation changes over time and particularly which time ranges have a higher dependency compared to others. Values of correlation closer to 1 indicate that spatial points are dependent on each other (in cases where there is less breakup observed) and values of correlation

closer to 0 indicate lesser dependencies between spatial points which could be observed in cases where there is more breakup and irregularities in the system.

4.5 Birth Rate, Death Rate and Spiral Wave Lifetime

The rate at which spiral waves are born or die or the amount of time for which they persist form some important features that could help to classify mechanisms for spiral wave breakup.

Calculating the birth rate, death rate and lifetime of the spiral waves is a challenge mostly because there is no standard method to detect the birth of a new wave or the death of a previously existing wave. Our approach involved tracking the spiral wave tip locations over time, as we were able to detect and record the coordinates of spiral tips using the method that was mentioned in Chapter 3. Iterating over discrete time periods, we used the proximity of the new waves to previously existing waves to decide whether we were looking at the birth of a new wave, death or the survival of an existing wave. The algorithm consisted of the following steps.

1. Iterate over each time step to record the number of waves and their respective x-y coordinates.

2. Starting at time step t, iterate over all the spiral tip coordinates recorded for each time step and record the following:

$$X_t = \vec{x_1}, \vec{x_2}, ..., \vec{x_n} \tag{4.15}$$

$$X_{t-1} = \vec{x_1}, \vec{x_2}, ..., \vec{x_m}, \tag{4.16}$$

   where X_t and X_{t-1} represent the new and old spiral tip coordinates respectively, and each $\vec{x_i} = (x, y)$ represents the coordinates of the spiral tips recorded for that time step.

3. Next, create a distance matrix of points as shown:

$$D_t = \begin{bmatrix} d_{1,1} & d_{1,2} & . & . & . & d_{1,m} \\ d_{2,1} & d_{2,2} & & & & \\ . & & . & & & \\ . & & & . & & \\ . & & & & . & \\ d_{n,1} & & & & & d_{n,m} \end{bmatrix}$$

.

Here, $d_{\alpha,\beta} = ||x_\alpha - x_\beta||$ such that $x_\alpha \in X_t$ and $x_\beta \in X_{t-1}$.

4. From this matrix, find the minimum entry $\overline{d}$ and the corresponding indices (j, k) where $j \in [1, n]$ and $k \in [1, m]$.

5. If $\overline{d} < r_t$, where r_t is the threshold radius, then remove the j^{th} row and k^{th} column from the matrix. Subsequently, $x_j \in X_t$ and $x_k \in X_{t-1}$ are the surviving tips and are stored in two vectors, $X_{new\_surviving}$ and $X_{old\_surviving}$. If there exists no other $\overline{d} < r_t$, execute Step 5. r_t in this case is a value that is chosen based on the spatial resolution of the domain over which we are iterating. If the movement of the spiral wave is restricted to a part of the domain, then a smaller radius may be considered whereas, if the movement of the wave is such that it covers different regions of the domain, a larger radius may be required.

6. After taking into account all the points that are less than r_t, the rest of the points are handled as follows.

   (a) All $x \in X_{t-1}/X_{old\_surviving}$ are counted as deaths and stored as X_{death}.

   (b) All $x \in X_t/X_{new\_surviving}$ are counted as births and stored as X_{birth}.

   The purpose of this is to remove all the coordinates of the surviving waves to avoid any double-counting.

7. For the next time step, repeat step 1 and continue the same for all other time steps.

4.6 Spiral Wave Tip Speed

Tracing out the spiral wave tip locations over time and writing out the coordinates formed the basis of deriving most of the characteristics like the speed, birth rate, death rate and lifetime of the waves. Unlike calculating the number of waves, deriving the speed from these coordinates posed more of a challenge. The challenge mostly lay in the fact that at any given time step, the coordinates for multiple waves were recorded. Also, after the onset of breakup, the short lifetimes of the spiral waves made it nearly impossible to trace a single trajectory that could be used to compute the speed. The assumption that was made in this case was to not consider the births and deaths at each time step. The following algorithm was used to calculate the speed of the spiral waves and its changes over time.

The main steps involved were the following.

1. Iterate over each time step to record the number of waves and their respective x-y coordinates.

2. Starting at time step t, iterate over all the coordinates recorded for each time step and record the following:

$$X_t = \vec{x_1}, \vec{x_2}, ..., \vec{x_n} \tag{4.17}$$

$$X_{t-1} = \vec{x_1}, \vec{x_2}, ..., \vec{x_m}, \tag{4.18}$$

   where X_t and X_{t-1} represent the new and old spiral wave tip coordinates respectively, and each $\vec{x_i} = (x, y)$ represents the coordinates of the spiral tips recorded for that time step.

3. Next create a distance matrix of points as shown:

$$D_t = \begin{bmatrix} d_{1,1} & d_{1,2} & . & . & . & d_{1,m} \\ d_{2,1} & d_{2,2} & & & & \\ . & & . & & & \\ . & & & . & & \\ . & & & & . & \\ d_{n,1} & & & & & d_{n,m} \end{bmatrix}$$

Here, $d_{\alpha,\beta} = ||x_\alpha - x_\beta||$ such that $x_\alpha \in X_t$ and $x_\beta \in X_{t-1}$.

4. From this matrix, find the minimum entry $\overline{d}$ and the corresponding indices (j, k) where $j \in [1, n]$ and $k \in [1, m]$. Up to this point, we follow the same steps described by the algorithm in Section 4.5.

5. If $\overline{d} < r_t$, where r_t is the threshold radius, then remove the j^{th} row and k^{th} column from the matrix. Subsequently, $x_j \in X_t$ and $x_k \in X_{t-1}$ are the surviving tips and are stored in a new vector, $\vec{t_s} = [\vec{x_1}, \vec{x_2}, ...\vec{x_l}]$ where $s \in [1, t_t]$, t_t being the total number of tips, and $\vec{x_i} = (x, y), i \in [1, l]$. The r_t in this case was selected using the same concept as described in Section 4.5.

6. From this vector, the speed is computed as

$$V_i = \frac{||x_i - x_{i+1}||}{\Delta t}. \tag{4.19}$$

We end up with $\vec{V_s} = [V_1, V_2, ...V_{l-1}]$, from which the average speed can be calculated by

$$V_{average} = \frac{1}{l-1} \sum_{i}^{l-1} V_i. \tag{4.20}$$

Chapter 5

Results

In this chapter, we show the results of applying the metrics to the spiral wave breakup scenarios obtained using the different breakup mechanisms we consider. Given a time series of the V_m values measured every 0.25ms for a total duration of 2s, and the spiral wave tip coordinates recorded every 1ms obtained from experimental simulations using the Fenton-Karma model, a step-by-step procedure enables us to apply the metrics in a logical order so that each metric can be studied together with the results of the previous metric. We found that strategy was useful for interpreting the output of some of the metrics and enabled us to understand more clearly the events that took place during the course of the simulation for the specific breakup scenarios studied.

Our first step is to produce a plot of the number of spiral waves over time. This plot gives us a high-level understanding of how spiral wave breakup proceeds over time and particularly when is the simulation characterized by more or less disorder. With this plot in place, the next step is to quantify any chaos present in the system. These metrics include the largest Lyapunov exponent, mutual information and spatial correlation. Finally, we characterize properties of the spiral waves, including the birth rate, death rate, lifetime of the spiral waves and the distribution of the spiral wave tip speeds over time. In the next chapter we will show how these results can be used to classify mechanisms purely by the application of the metrics.

5.1 Number of Spiral Waves

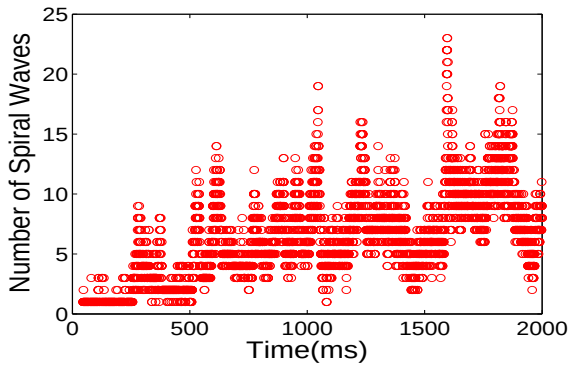

(a) Steep APD Restitution

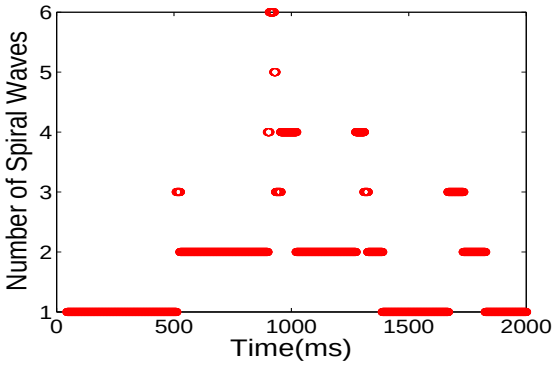

(b) Discordant Alternans

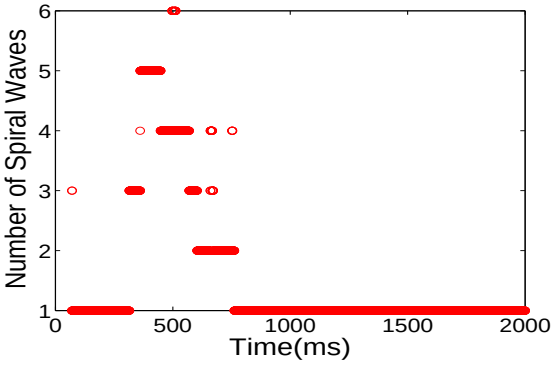

(c) Bistability

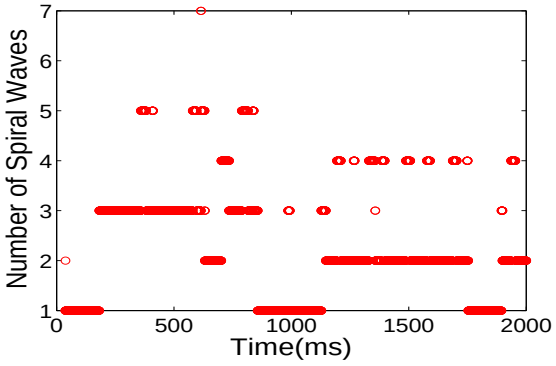

(d) Doppler Effect

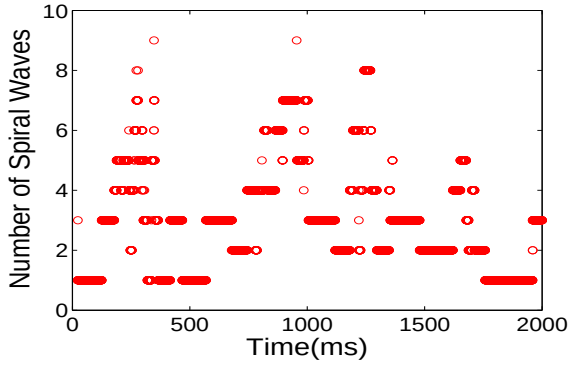

(e) Supernormal Conduction Velocity

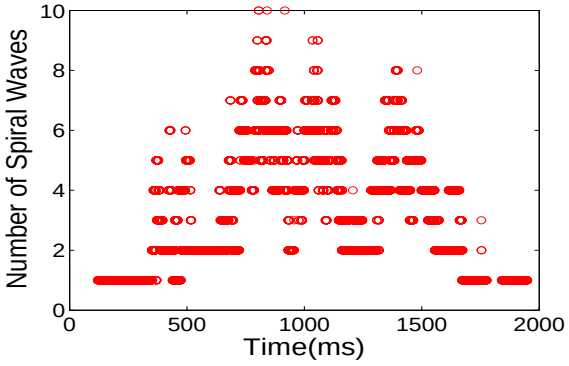

(f) Periodic Boundary Conditions

Figure 5.1: Distribution of number of spiral waves over time.

First, we consider how the number of spiral waves changes over time for each breakup mechanism, as shown in Figure 5.1. For the case of steep APD restitution, starting from the beginning of the simulation, the number of waves steadily increases over time, displaying an alternating pattern, with a maximum value of around 20 spiral waves. For discordant alternans, we observe a stable spiral wave until t=500ms, after which breakup is induced such that around t=1000ms, we see a maximum of 6 waves in existence. From this time step onwards, the number of waves decreases until the system goes back to being stable towards the end of the simulation with the presence of a single wave.

For bistability, the plot shows a rapid growth in the number of waves around 250ms with a maximum of 6 spiral waves, but the system quickly goes back to exhibiting a stable spiral wave, as soon as around 750ms.

In the case of the Doppler effect, we observe more uniform activity throughout the simulation. The number of waves rarely remains at a constant value for more than a few hundreds of ms before it exhibits either an increase or a decrease. The maximum number of waves observed in this case is 7.

Supernormal conduction velocity shows varied activity over the range of 0-1700ms, where between 2 and 8 spiral waves are present. From t=0-500ms, the number of spiral waves increases, with a maximum value of 8. After this, there is a drop in the value for a few hundred ms before a sudden spike occurs in the number of waves until t=1700ms.

The last case of periodic boundary conditions can be described as a stable wave which shows rapid breakup after t=250ms. The entire simulation is characterized by a large number of spiral waves, with a maximum value of 10. As in the Doppler effect mechanism, the number of waves does not remain constant for more than a few hundered ms before it changes.

5.2 Lyapunov Exponents

Table 5.1 lists the largest Lyapunov exponent for each mechanism under consideration. The positive values indicate irregular behaviour or the presence of wave breakup in the system. Steep APD restitution and discordant alternans yielded more positive values than the rest of the mechanisms.

Breakup through bistability did not yield an exponent indicative of irregular behaviour, which may be justified by the distribution that we saw earlier for the number of spiral waves in Figure 5.1. The Doppler effect showed a fairly positive value, consistent with the breakup that was observed for this mechanism. Supernormal conduction velocity seemed to demonstrate an almost stable system, which could be attributed to the rise and fall in the number of spiral waves and the value almost becoming constant toward the end of the simulation. Periodic boundary conditions showed a positive value. However, based on the breakup that took place, we expected a larger value, owing to the irregular behaviour that was observed for this mechanism.

Table 5.1: Largest Lyapunov exponent.

Mechanism	Largest Lyapunov Exponent Value
Steep APD restitution	0.1741
Discordant alternans	0.4645
Bistability	-0.2528
Doppler effect	0.0706
Supernormal conduction velocity	0.0005
Periodic boundary conditions	0.0022

5.3 Mutual Information

The results of calculating the mutual information for each mechanism are shown below.

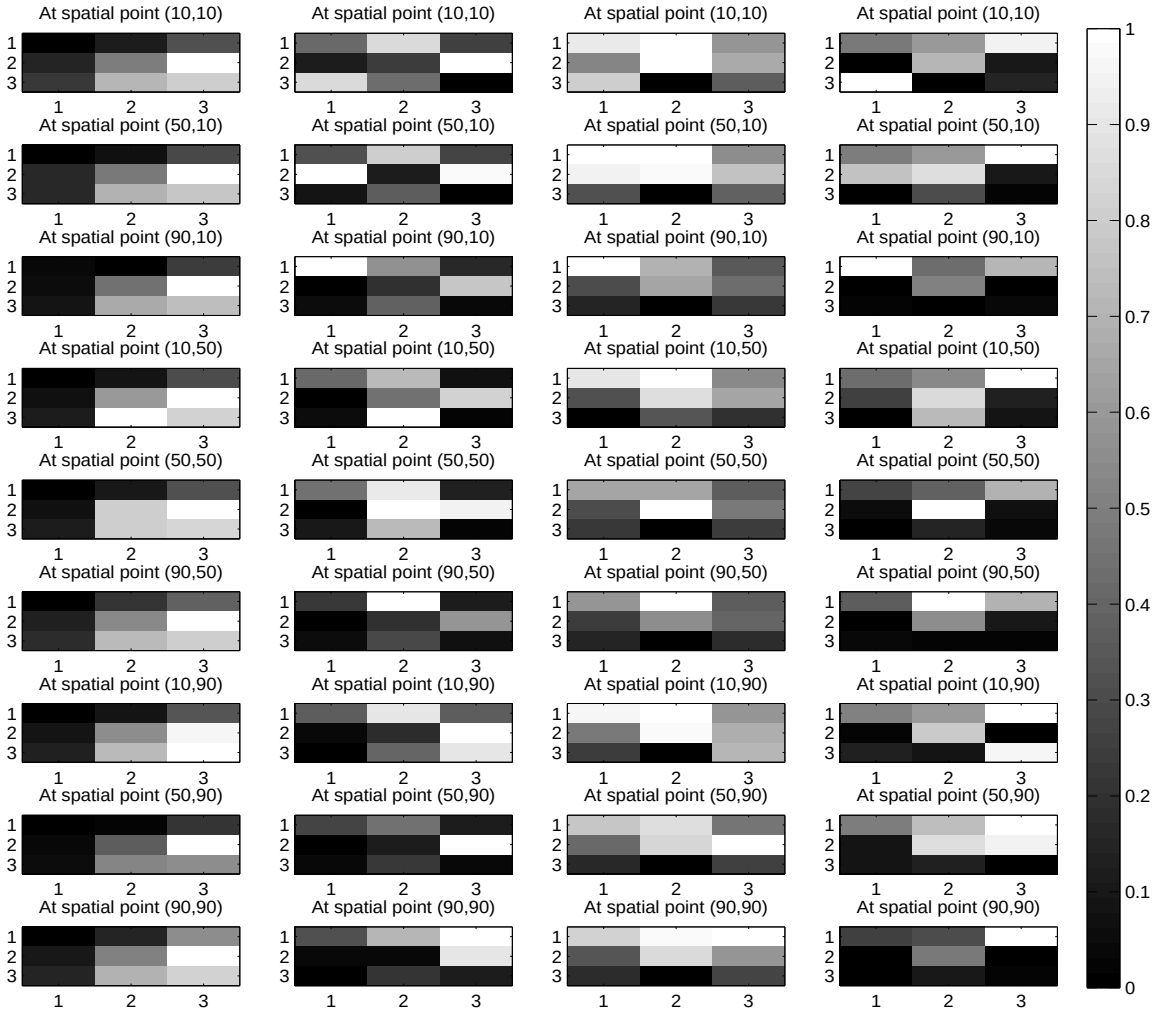

Figure 5.2: Mutual information for steep APD restitution.

Figure 5.2 shows the change in mutual information over time when spiral wave breakup occurs by steep APD restitution. As mentioned in Section 4.3.3, we consider a sample of points in the domain to give us a broad view of how much information is shared between various spatial points in the domain. The nine rows correspond to the nine points that were considered. The points

were chosen along the boundaries as well as from the centre of the domain so as to cover the entire region. The four columns represent the duration of the simulation i.e. 2000ms split into four time ranges: 0-500ms, 500-1000ms, 1000-1500ms, and 1500-2000ms, from left to right. Dark colors, with mutual information values close to 0 either represent very little information being shared, implying irregular activity due to wave breakup, or indicate that not much activity was present in the domain. The light colors corresponding to mutual information values close to 1 are indicative of stable behaviour and the absence of wave breakup in the system. As mentioned in Chapter 4, we are concerned less with the absolute values of mutual information and more with the changes in the information shared between spatial points over time. Another key to understanding the concept of mutual information is the fact that spatial points share the most amount of information with themselves. This is best observed in the last three time ranges, once breakup has been initiated and sustained.

Relating the plot of mutual information shown in Figure 5.2 to Figure 5.1a, we see that in the time range 0-500ms, the information that is shared is more localized, but a majority of the domain has low mutual information. The regions of the domain that are not dark indicate the presence of spiral waves that did not break up in those parts of the domain. Over the next time interval, we observe that the value of the information shared by the spatial point decreases, which is in tandem with the growth in the number of spiral wave over time. Between 1000ms and 1500ms, there is a slight increase in the mutual information values, but during the next 500ms, the figure is mostly dark. This is once again consistent with the alternating patterns that we observed in the distribution of the number of spiral waves over time.

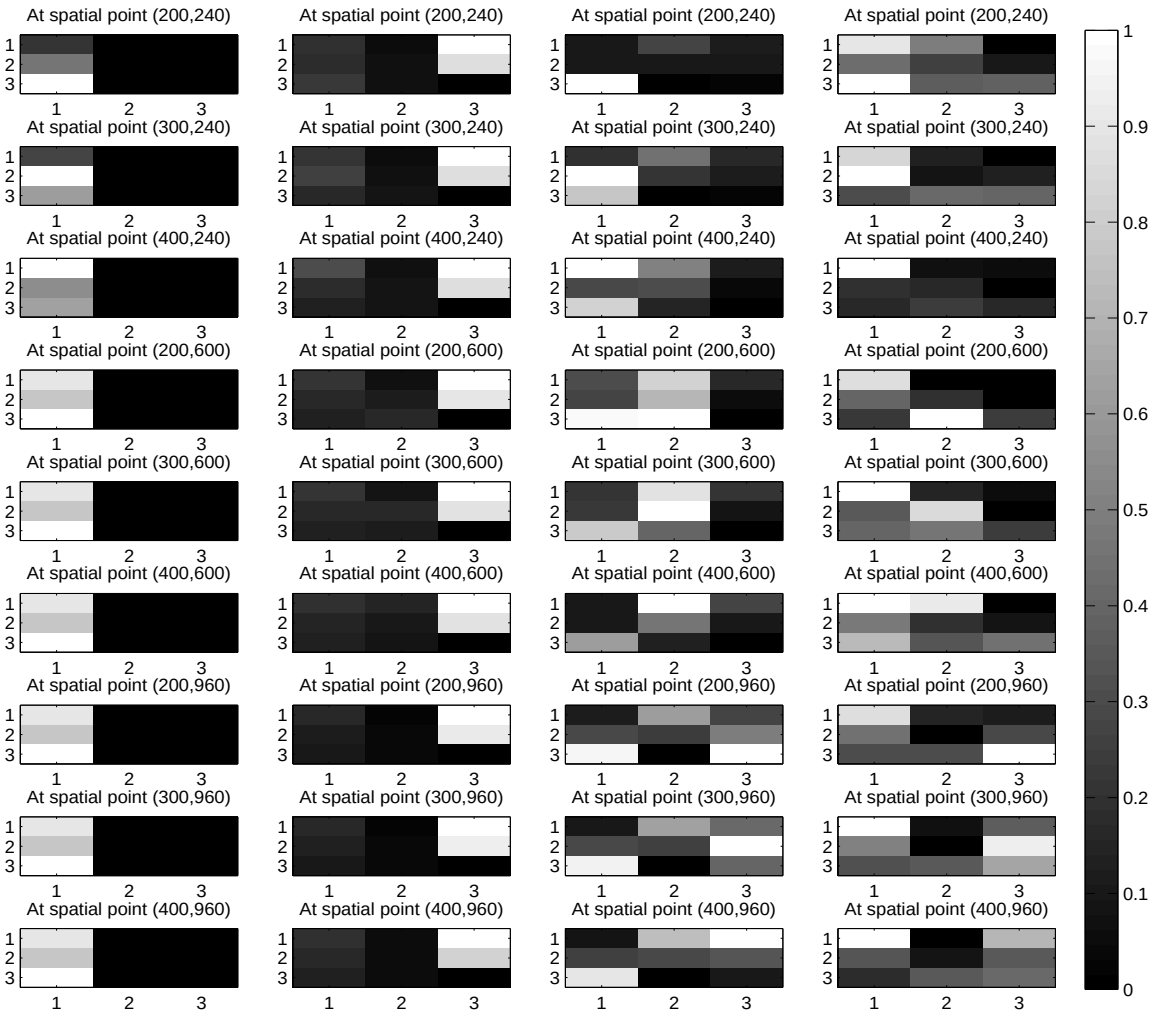

Figure 5.3: Mutual information for discordant alternans.

When breakup is induced by discordant alternans, different patterns in the mutual information occur. Between 0 and 500ms, some parts of the domain have high mutual information values, similar to the behaviour that was observed for steep APD restitution. From Figure 5.1b, we also know that during this interval, a single spiral wave was present in the system. From 500ms to 1500ms, the information shared by the spatial points decreases due to the initiation of breakup. Close to 1500ms and continuing on to the next time interval, the system starts to display an increase in the mutual

information as the breakup begins to subside. This behaviour is consistent with the distribution that was observed for the distribution of spiral waves over time when breakup was induced by discordant alternans. Steep APD restitution and discordant alternans behaved similarly in the first 500ms of the simulation with respect to mutual information.

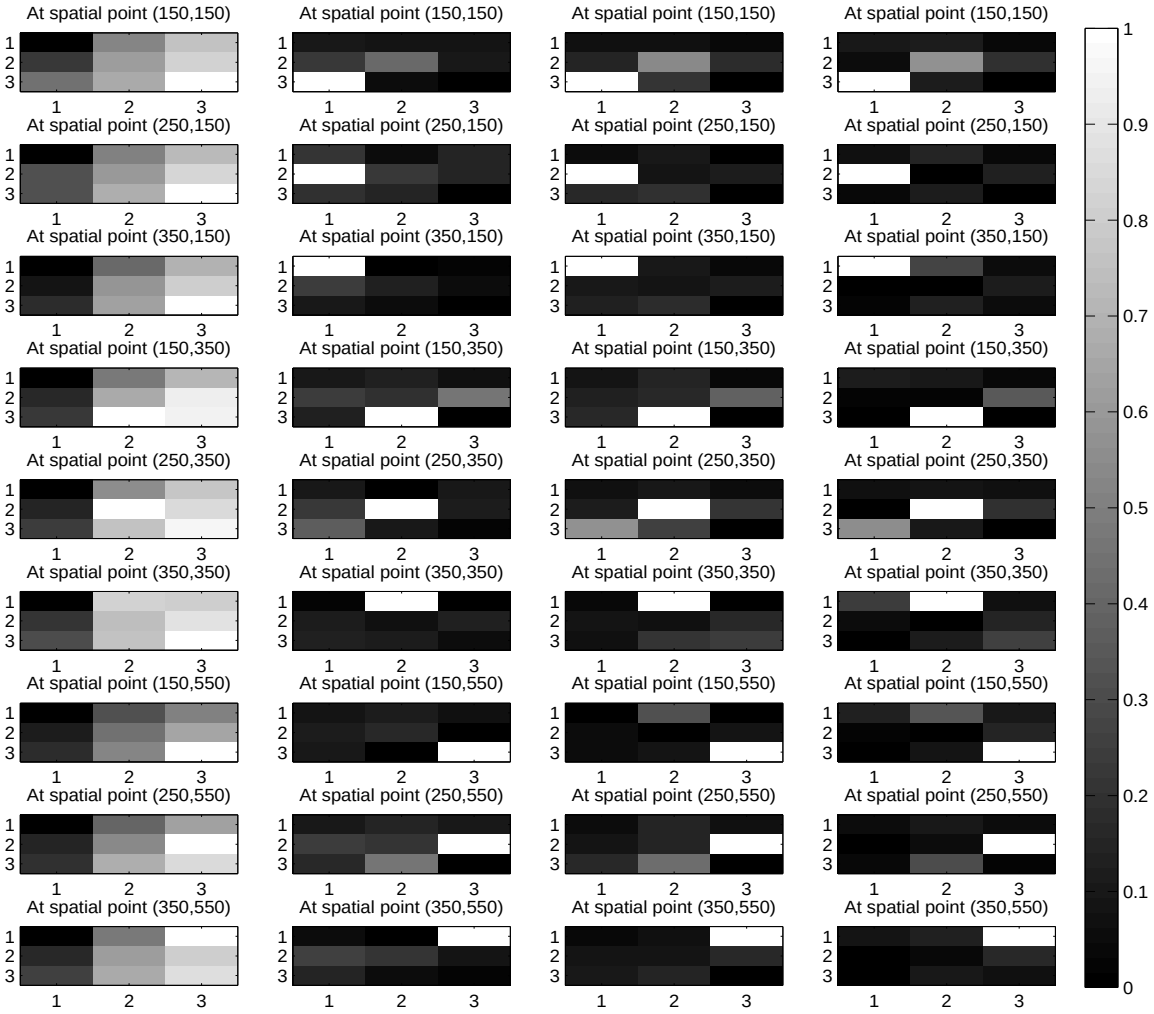

Figure 5.4: Mutual information for bistability.

The bistability mechanism exhibited different mutual information properties.In the range of 0-500ms, a combination of high and low values for mutual information are present. From Figure

5.1c, we know that most of the breakup occured within the first 750ms. Despite there being breakup, there is still a fair amount of information that is shared, but over the next three time intervals we see a majority of the domain is governed by low values of mutual information. The combination of high and low values of information during 0-500ms can be explained by the presence of the 2:1 conduction block that was described in Section 2.2. The high information regions possibly represent the stable part of the system which conduct every incoming impulse, whereas the regions with low information values represent parts of the domain where breakup occurred.

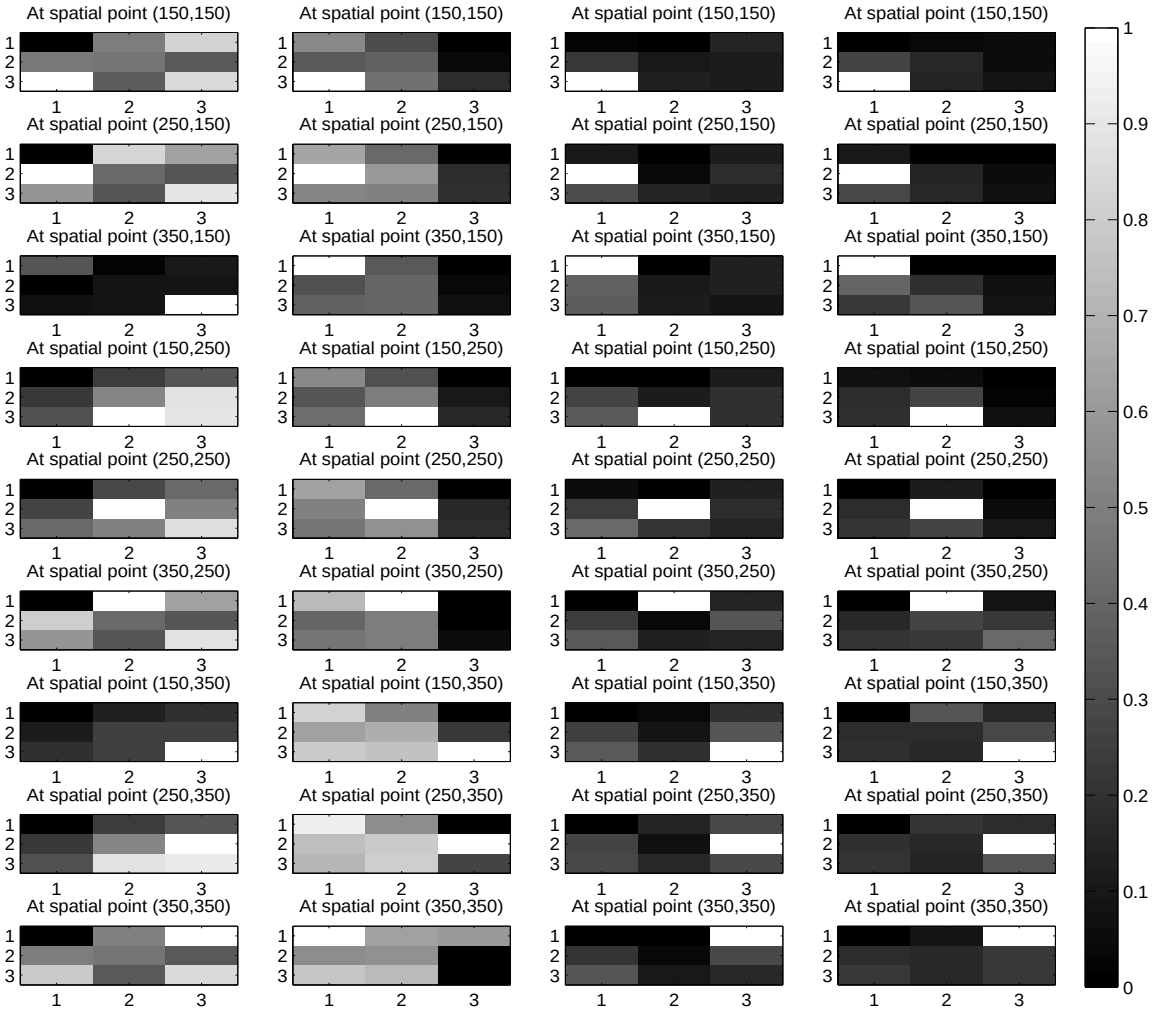

Figure 5.5: Mutual information for Doppler effect.

The Doppler effect showed considerably different behaviour, as seen in Figure 5.5. In the range 0-500ms, the amount of information shared is considerably low, evidenced by the predominance of dark gray in most of the domain. From the distribution of the number of waves in Figure 5.1d, by t=1000ms, there was a single spiral wave present, which the mutual information plot conveys by the pockets of white during this time of the simulation. As the breakup increases over the rest of the simulation, there is a decrease in the mutual information values.

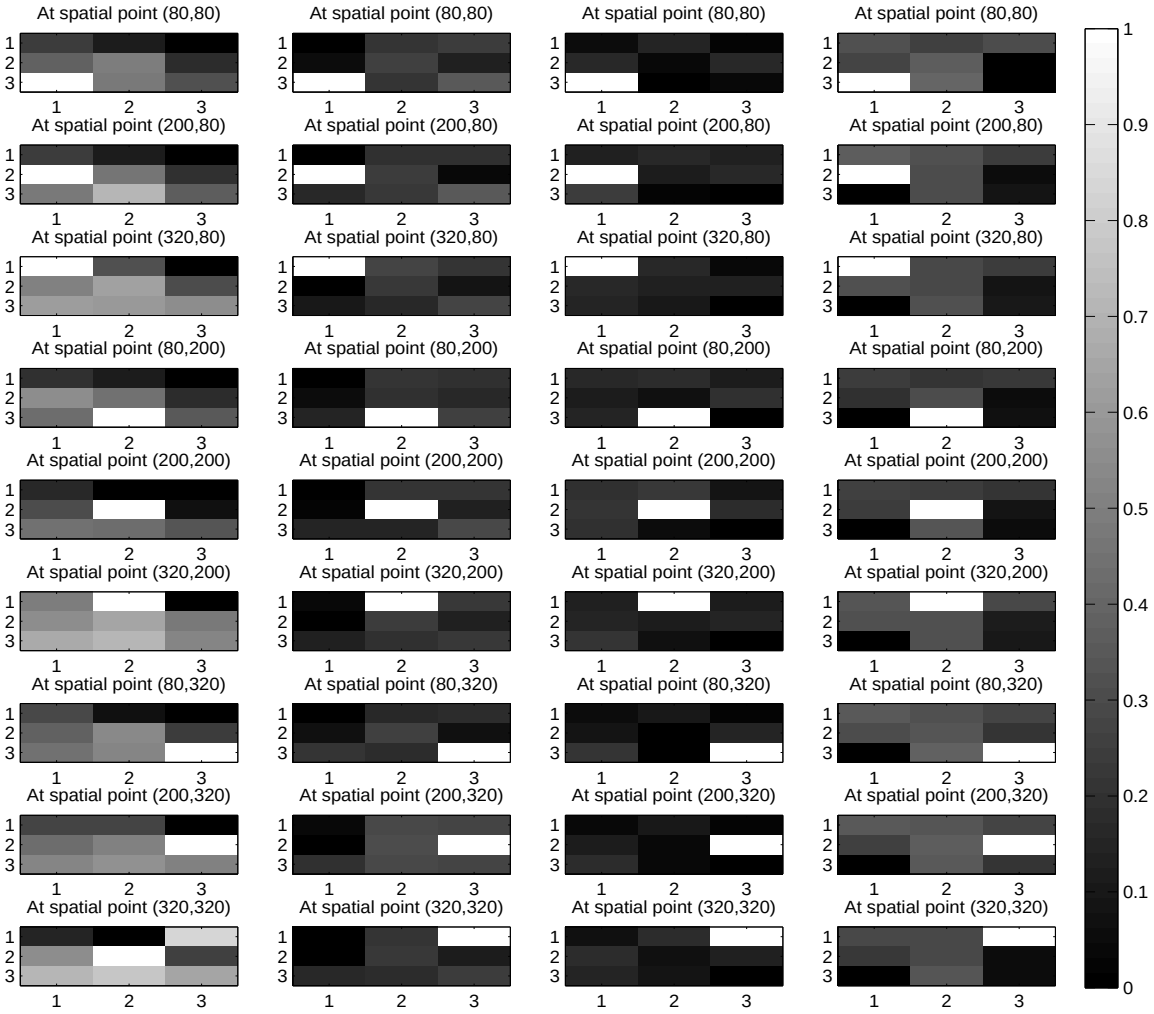

Figure 5.6: Mutual information for supernormal conduction velocity.

The behaviour observed for mutual information when breakup was induced by supernormal conduction velocity was consistent with Figure 5.1e. During the interval 0-500ms, the mutual information values are relatively higher when compared with the next three intervals. As the simulation progresses and the amount of breakup increases, the mutual information values decrease, as observed between 500ms and 1500ms of Figure 5.6. When the breakup begins to subside over the last interval, the mutual information values corrspondingly increase, as evidenced by the gray regions of the figure toward the end of the simulation.

Figure 5.7: Mutual information for periodic boundary conditions.

When breakup was induced by periodic boundary conditions, during the interval 0-500ms, a combination of high and low information values were present. This stems from the fact that until t=1000ms not much activity occurred as gathered from Figure 5.1f, but after this time, breakup is initiated. Between 500ms and 1000ms, mutual information values decrease, indicating a significant increase in the number of waves. For the interval 1000-1500ms, the information decreases even more, suggesting the existence of a large number of spiral waves. Toward the last interval of the simulation, mutual information values for the system increase slightly. This corresponds to a decrease in the number of spiral waves during this part of the simulation.

5.4 Spatial Correlation

Next, we considered the spatial correlation for each of the mechanisms.

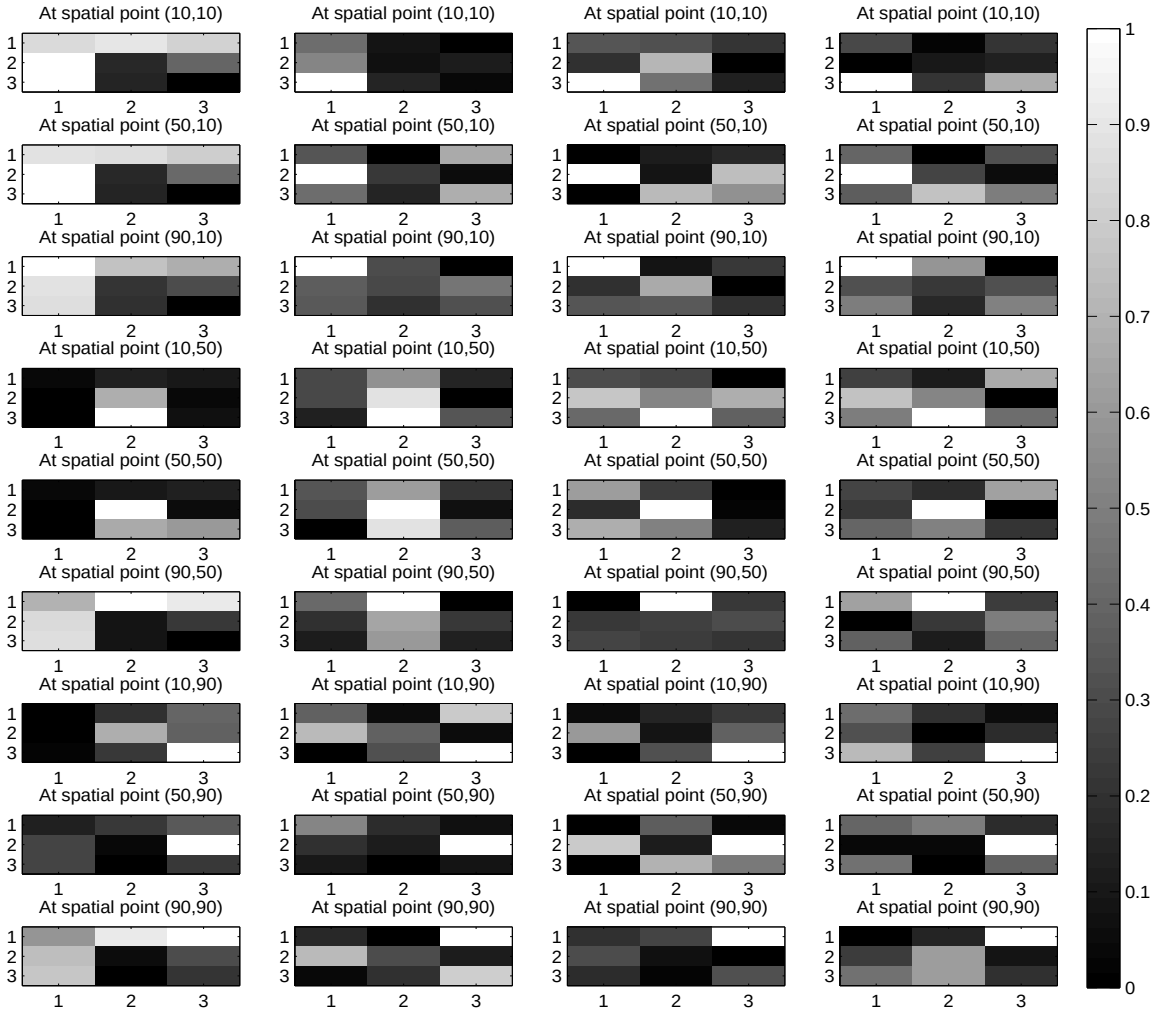

Figure 5.8: Spatial correlation for steep APD restitution.

Figure 5.8 shows the spatial correlation over time for the case of steep APD restitution. As before, the nine rows correspond to the nine spatial points in the domain that were considered, and the four columns show the spatial correlation in each of the four time intervals considered: 0-500ms, 500-1000ms, 1000-1500ms, and 1500-2000ms. Low correlation values between points, shown in black

or dark gray and indicated by values close to 0, correspond to irregular or limited wave activity, whereas high correlation values, shown in white and corresponding to correlation values close to 1, indicate that wave activity is more closely correlated between the two sites. Once again, we are less concerned with the absolute values of correlation, and more with the changes in the correlation and dependencies between spatial points, observed over time.

For steep APD restitution, dependencies are higher in the first part of the simulation between 0 and 500ms. As the simulation proceeds, the dependency values decrease. From 1000-2000ms, the correlation values are lower, which fits with the fact that as the time increased, the number of spiral waves also increased, leading to more irregularities, less information in the system, and hence reduced dependencies.

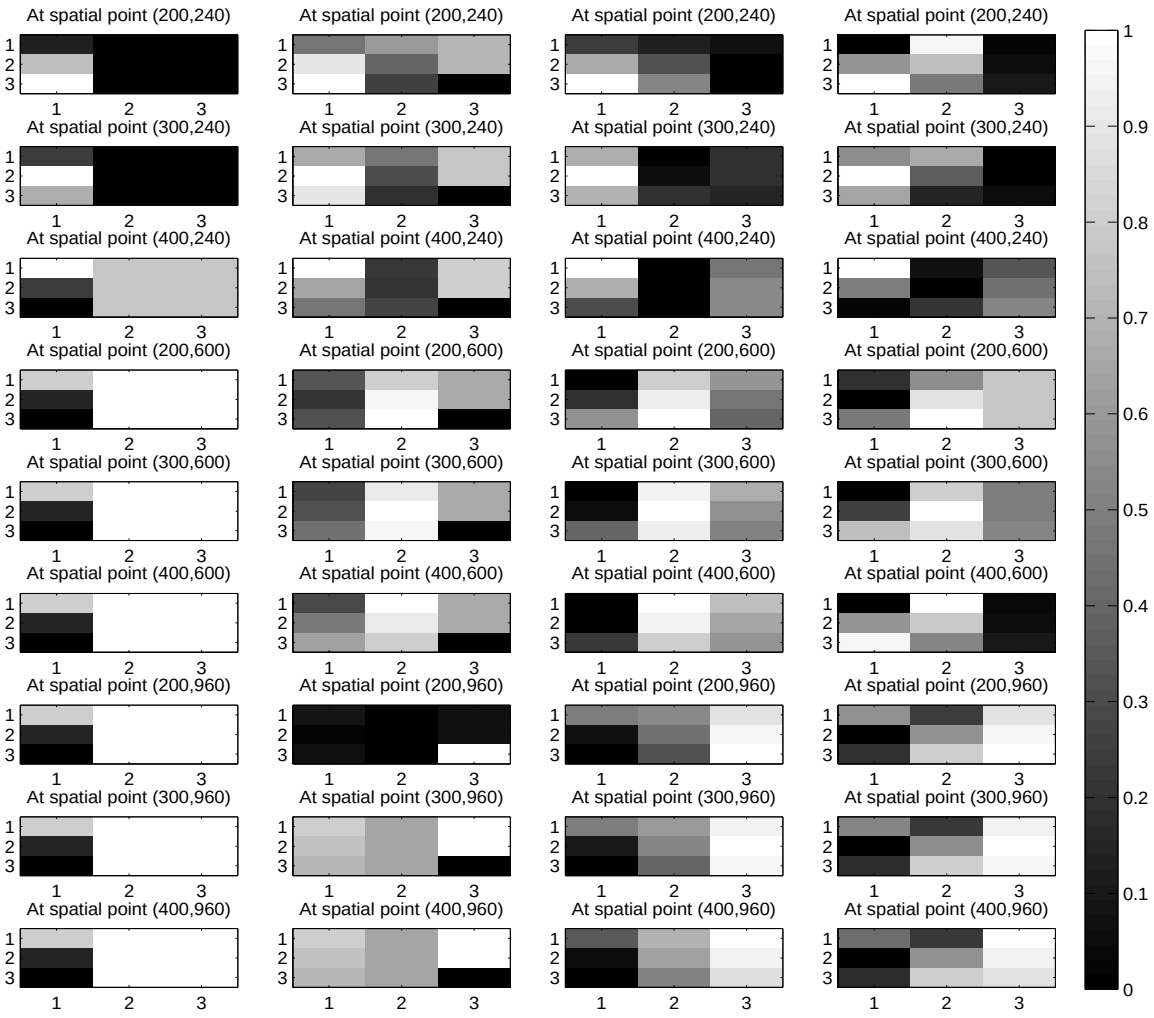

Figure 5.9: Spatial correlation for discordant alternans.

Figure 5.9 shows how the spatial dependencies changed when breakup was induced by discordant alternans. During the interval 0-500ms, extremely high correlation values are concentrated in some parts of the domain due to the fact that there was a single spiral wave present for the first part of the simulation, as observed from Figure 5.1b. During 500-1000ms, the dependency decreases, and as the simulation proceeds, the correlation values are seen to decrease further in some parts of the domain. During the last interval of the simulation, an increase in the correlation values are

observed as the amount of breakup in the system decreases.

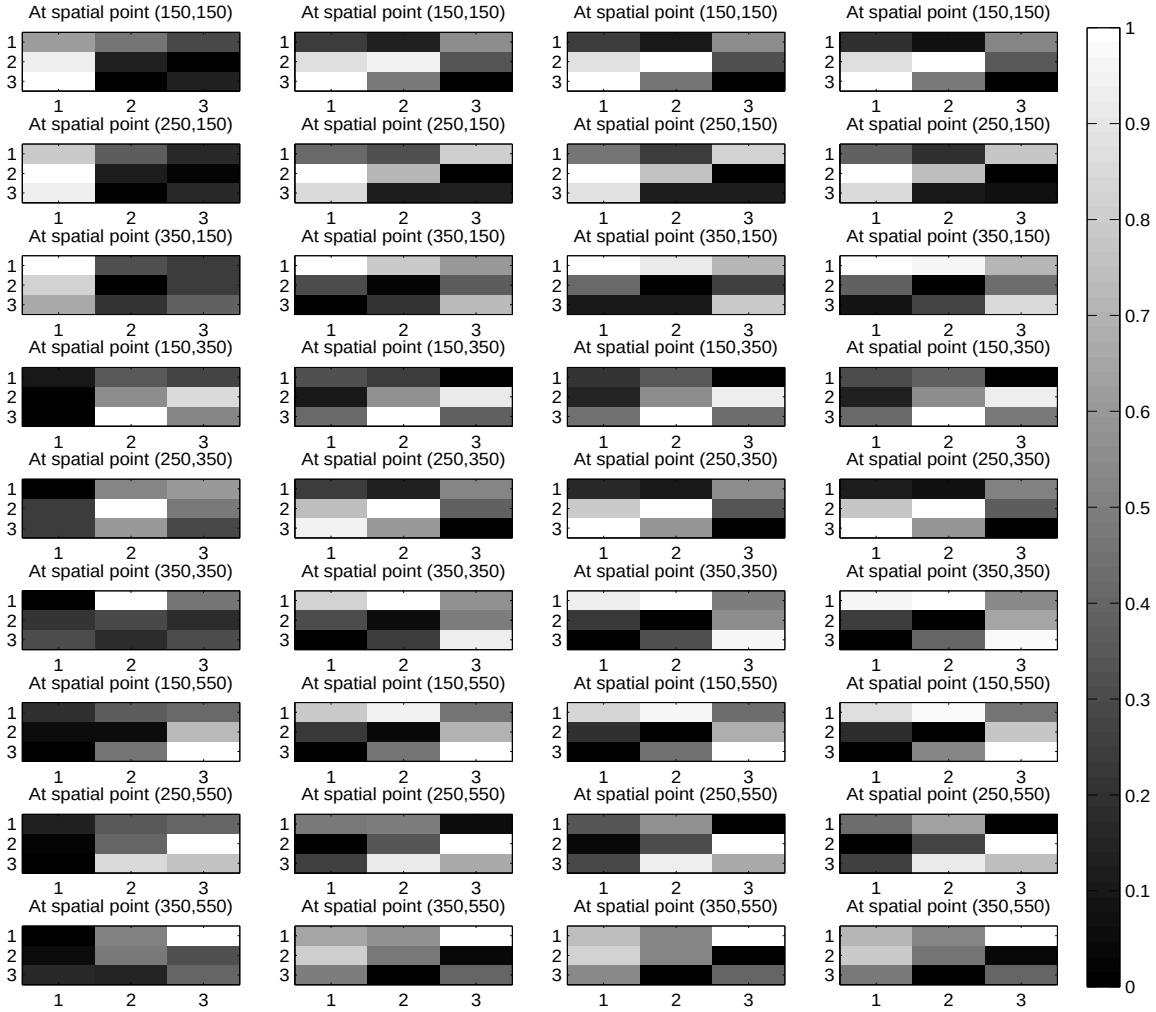

Figure 5.10: Spatial correlation for bistability.

For the case of breakup induced by bistability, from 0 to 500ms, where most of the breakup takes place, low correlation values are observed in most parts of the domain. For this mechanism of breakup, as we recall from Figure 5.1c, we know that around t=750ms, the dynamics started to stabilize as only a single spiral wave remained for the rest of the simulation. As a result, during 500-1000ms, the correlation values generally increase and remain almost constant for the rest of

the simulation.

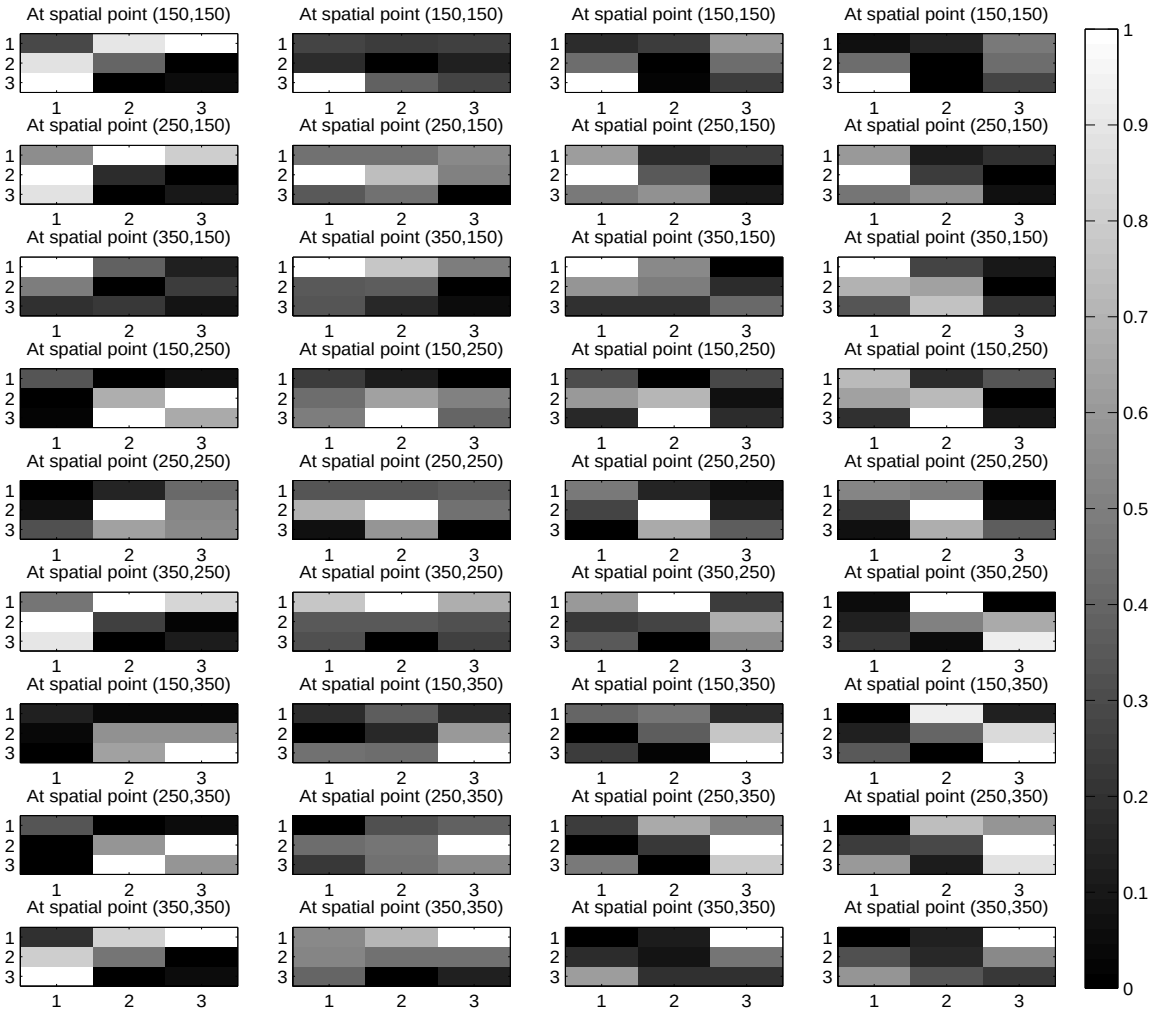

Figure 5.11: Spatial correlation for Doppler effect.

More activity was observed when the spatial correlation was studied for breakup induced by the Doppler effect, as seen in Figure 5.11. The interval 0-500ms includes a combination of high and low correlation values owing to the fact that breakup was initiated around t=250ms. As the simulation proceeds, the correlation values decrease, corresponding to an increase in breakup over time. As the breakup continues over the rest of the simulation as well, the correlation values are

lower over 1500-2000ms, which is consistent with the distribution of the number of spiral waves, as shown in Figure 5.1d.

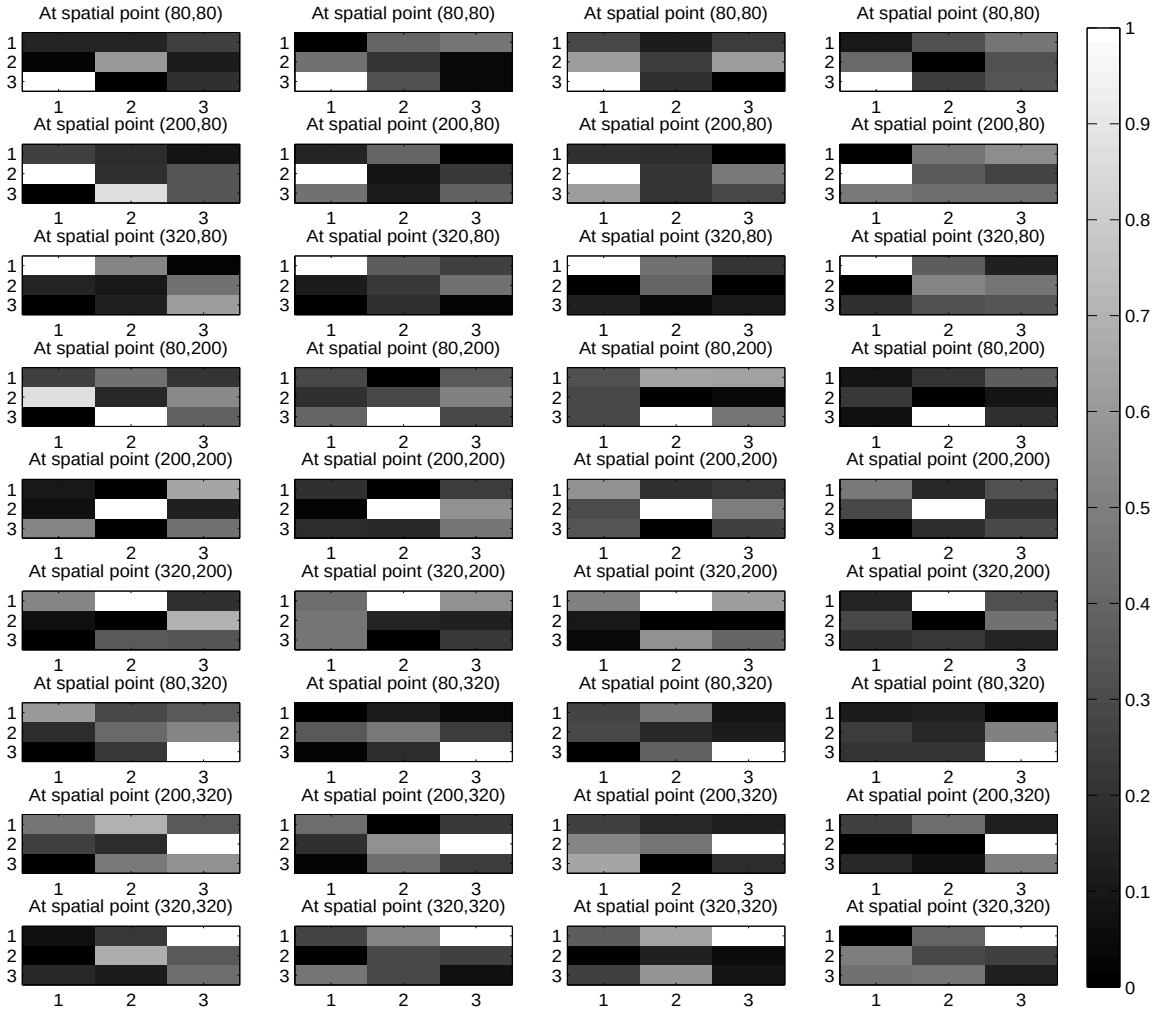

Figure 5.12: Spatial correlation for supernormal conduction velocity.

In the case of supernormal conduction velocity, during the interval 0-1000ms, we observe lower values of correlation. These correlation values are seen to continue over the rest of the simulation, which can be explained by the sustained breakup for the second half of the simulation.

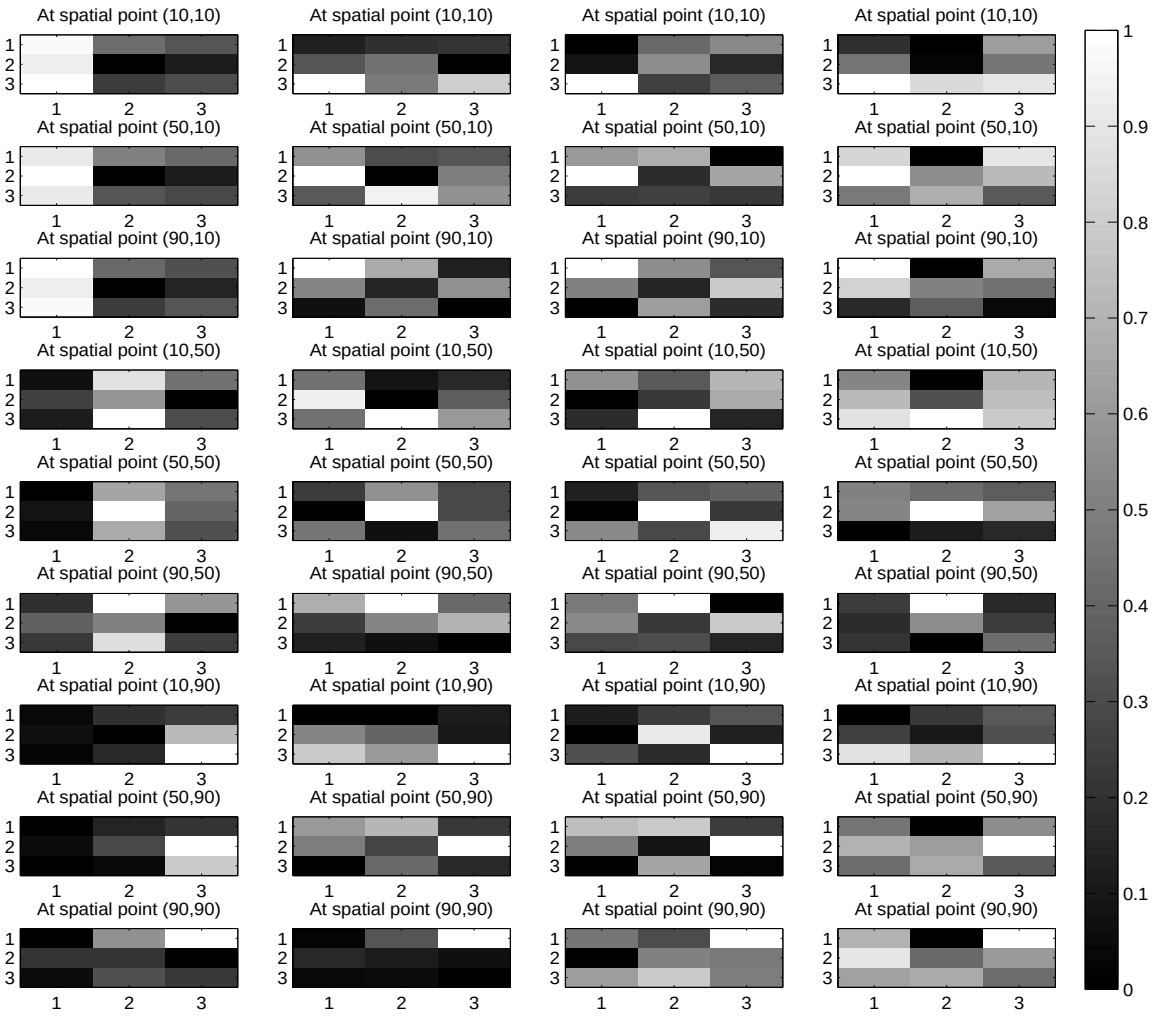

Figure 5.13: Spatial correlation for periodic boundary conditions.

In the case of periodic boundary conditions, during the interval 0-500ms, the presence of high correlation values are due to the fact that breakup was not really initiated until t=250ms. Upon the onset of breakup, correlation values decrease rapidly. From 500ms to 1500ms, we observe low correlation values which is indicative of the breakup that takes place during this time. Toward the end of the simulation, as observed in Figure 5.1f, the breakup decreased, which translates into high correlation values during this time.

5.5 Birth Rate, Death Rate and Spiral Wave Lifetime

Table 5.2 shows the calculated birth rate and death rate for each breakup mechanism.

Table 5.2: Birth rates and death rates.

Mechanism	Birth Rate	Death Rate
Steep APD restitution	$0.158824ms^{-1}$	$0.157928ms^{-1}$
Discordant alternans	$0.001535ms^{-1}$	$0.001407ms^{-1}$
Bistability	$0.037306ms^{-1}$	$0.037176ms^{-1}$
Doppler effect	$0.152357ms^{-1}$	$0.152102ms^{-1}$
Supernormal conduction velocity	$0.082912ms^{-1}$	$0.081395ms^{-1}$
Periodic boundary conditions	$0.413171ms^{-1}$	$0.413035ms^{-1}$

For almost all breakup mechanisms, the birth rate and death rate are almost equal, meaning that over time, the spiral waves die at almost the same rate that they are born. In all the cases, we also note that the birth rate is always larger than the death rate. However, these values as a whole do not give us much insight into the events that take place during breakup.

Next, we study the time series distribution of the spiral wave lifetimes along with the frequency distribution of the lifetimes for each of the mechanisms.

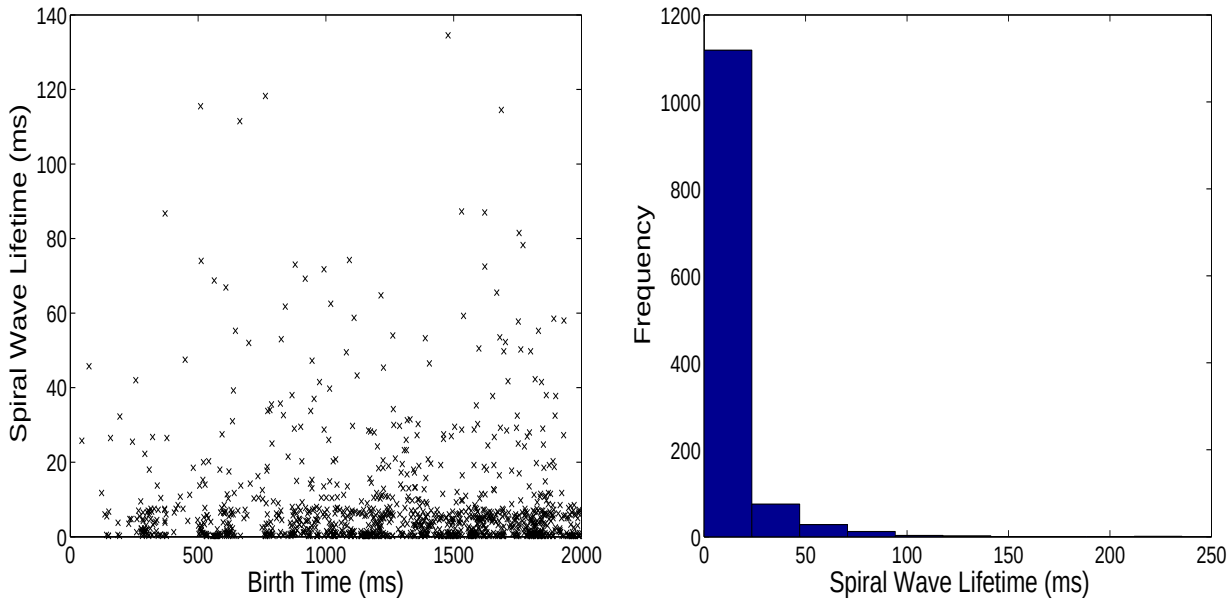

(a) Time series distribution of wave lifetime

(b) Histogram

Figure 5.14: Spiral wave lifetime for steep APD restitution.

Figure 5.14a shows the distribution of the spiral wave lifetimes as a function of their time of birth. Thus, for each time step, we are able to observe all the waves that were born during that time and for how long they survived. Figure 5.14b shows a histogram of the spiral wave lifetimes.

In this particular case of steep-APD-restitution-induced breakup, the average lifetime of the waves was very low; most waves had a lifetime that ranged between 0 and 50ms. This means that most of the tips were short-lived, but in terms of the breakup, this could be attributed to the fact that spiral waves would re-combine and break up in subsequent time steps if we take the alternating patterns in the distribution of waves into account.

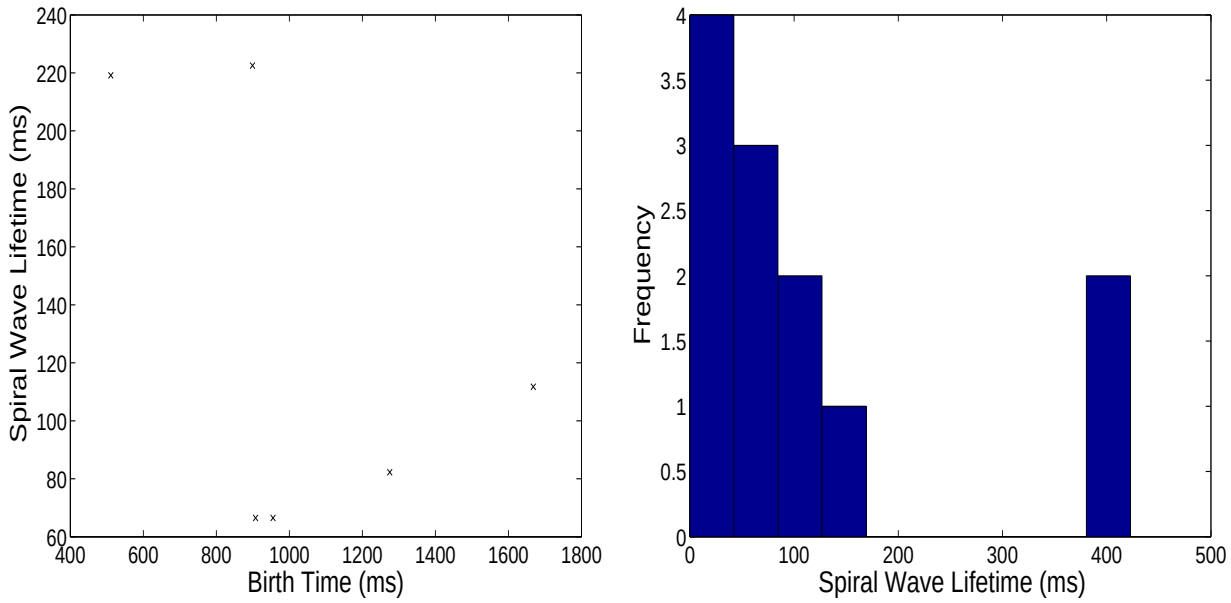

(a) Time series distribution of wave lifetime

(b) Histogram

Figure 5.15: Spiral wave lifetime for discordant alternans.

As shown in Figure 5.15, breakup from discordant alternans featured a smaller number of waves, but most of the waves had varied lifetimes that fell anywhere in the range 0-150ms. A minority of them were also seen to last as long as 400ms. It is important to note in this case that when the number of waves that is observed for a particular mechanism is very low, it is harder to characterize such behaviour accurately. Having access to more data that exhibits this particular mechanism of spiral wave breakup would help us study it in a more detailed manner.

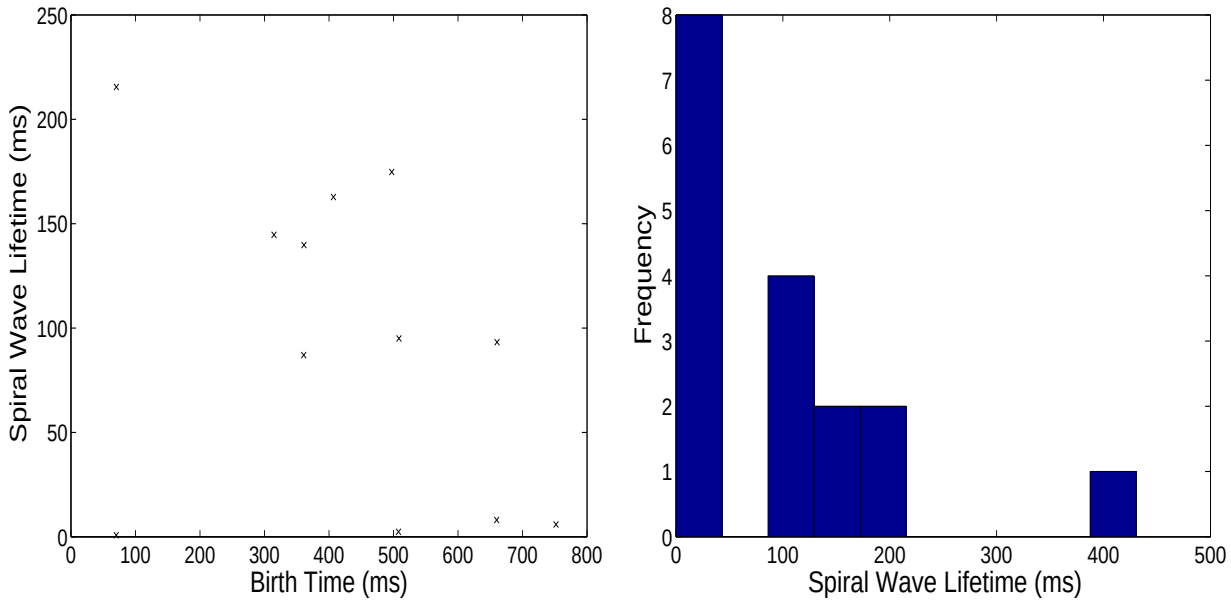

(a) Time series distribution of wave lifetime

(b) Histogram

Figure 5.16: Spiral wave lifetime for bistability.

Most of the spiral waves in the case of bistability, as shown in Figure 5.16, survived for a maximum time of 50ms, with the occurrence of longer-lasting waves falling off roughly exponentially. There were a number of waves that survived longer, with lifetimes varying between 100ms and 200ms.

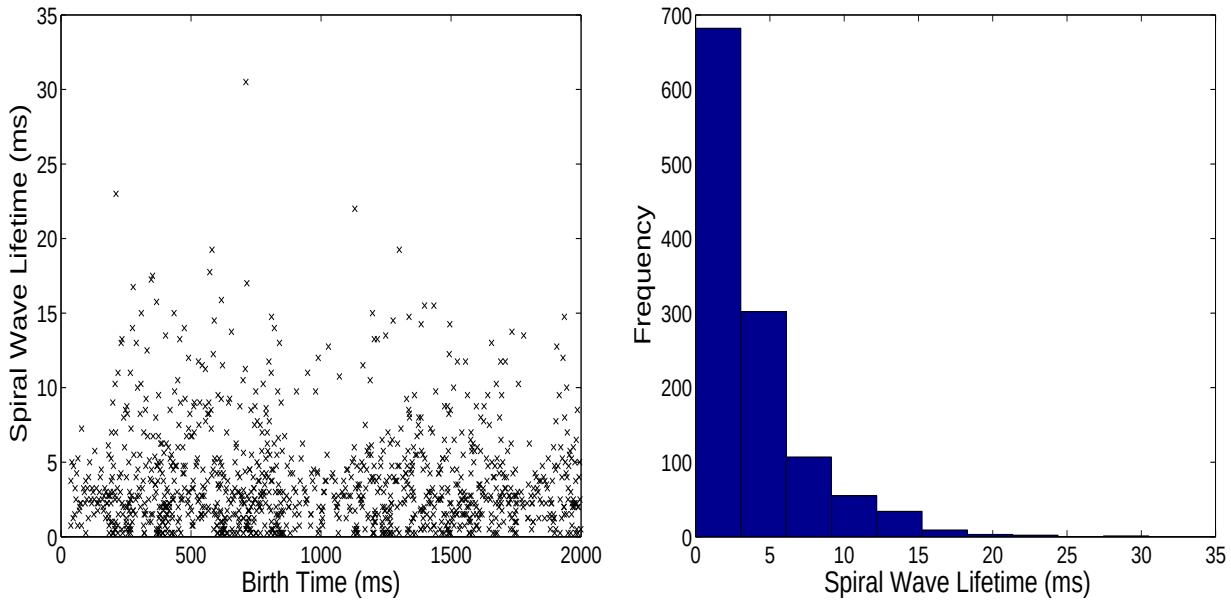

(a) Time series distribution of wave lifetime

(b) Histogram

Figure 5.17: Spiral wave lifetime for Doppler effect.

The time series plot in Figure 5.17 shows a very chaotic distribution of spiral wave lifetimes for the Doppler effect. From previous metrics, we know that the Doppler effect is known to exhibit more irregular behaviour than others, and these plots similarly convey that throughout the simulation there were a large number of waves that were born and died rapidly. These waves generally had a very short lifetime that was in the range 0-15ms.

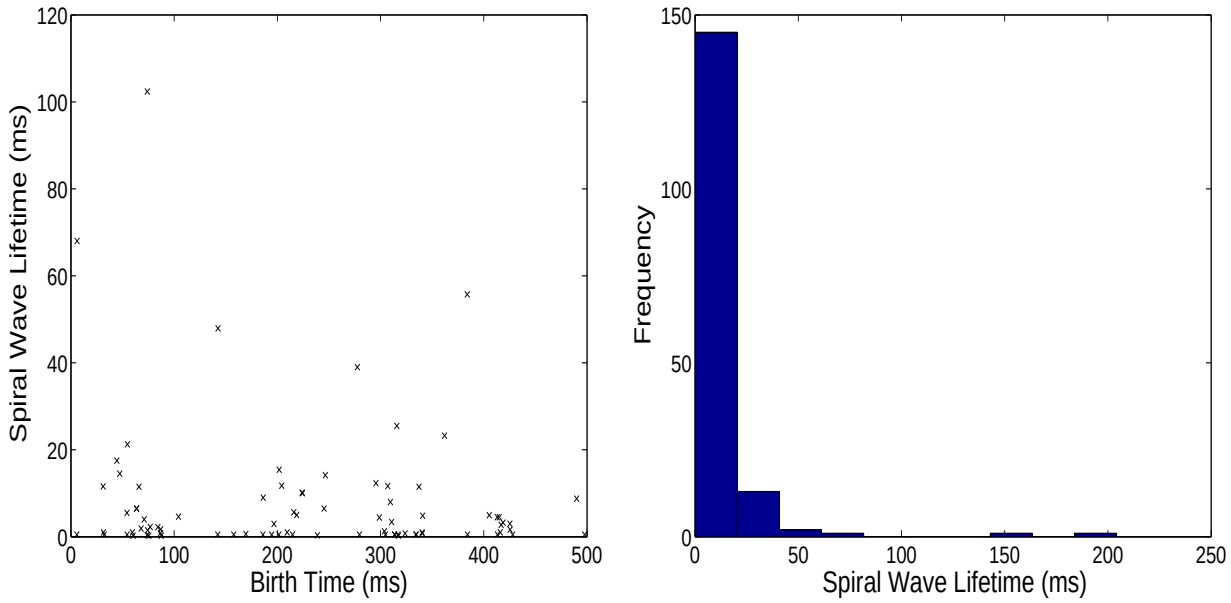

(a) Time series distribution of wave lifetime

(b) Histogram

Figure 5.18: Spiral wave lifetime for supernormal conduction velocity.

Figure 5.18 shows that most of the waves induced by supernormal conduction velocity had lifetimes that lasted between 0 and 25ms. There were also some waves that lasted for close to 50ms.

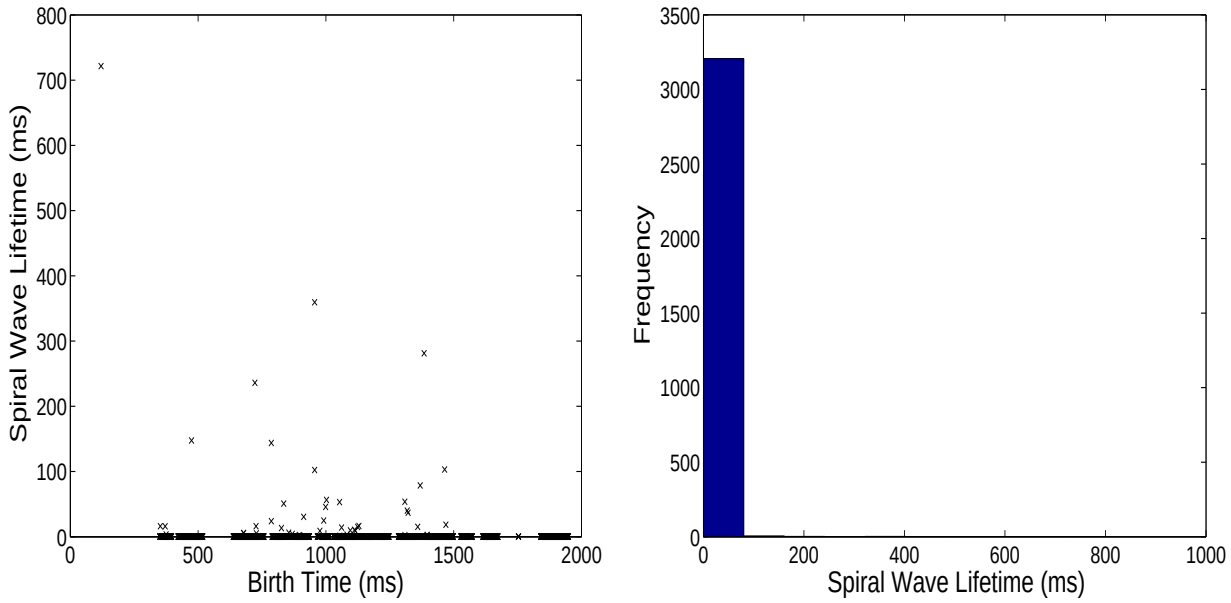

(a) Time series distribution of wave lifetime

(b) Histogram

Figure 5.19: Spiral wave lifetime for periodic boundary conditions.

From the distribution of lifetimes of spiral waves arising from periodic boundary conditions in Figure 5.19, we observed that most of the waves lasted for less than 100ms. There was a very large number of waves present during the simulation but with very small lifetimes. This is consistent with the large amount of breakup observed in Figure 5.1f.

5.6 Spiral Wave Tip Speed

Below, we present the spiral wave tip speeds for each of the mechanisms. Each case consists of a time series distribution and a frequency plot of the speed over time.

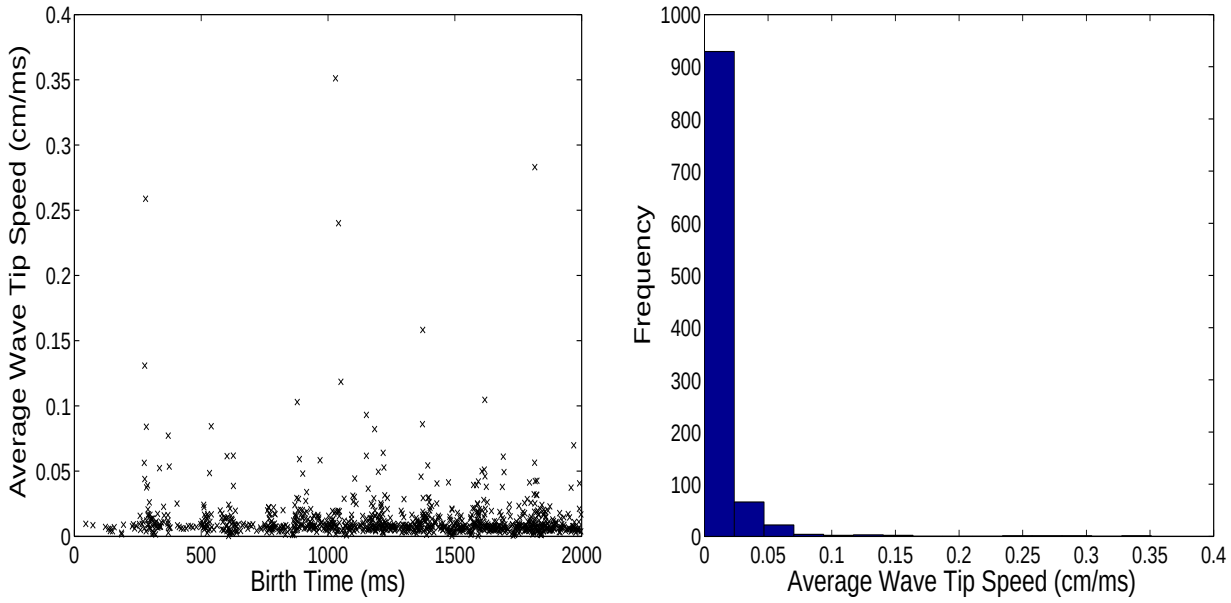

(a) Time series distribution of spiral wave tip speed

(b) Histogram

Figure 5.20: Spiral wave tip speed for steep APD restitution.

Figure 5.20a shows the distribution of the average spiral wave tip speeds for the case of steep APD rstitution, computed for the lifetime of each wave tip over time. Figure 5.20b shows the frequency distribution of these speeds.

For this particular case, a large number of spiral wave tips had an average speed that ranged between 0 and 0.05cm/ms. The maximum average speed that was observed during this simulation was close to 0.1cm/ms.

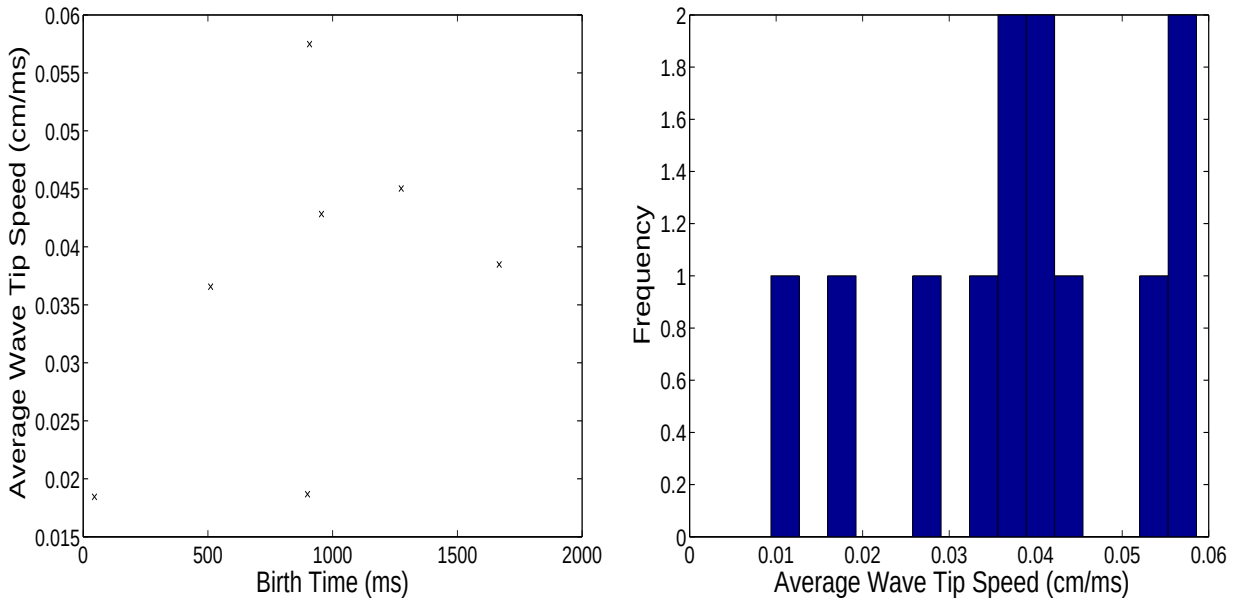

(a) Time series distribution of spiral wave tip speed

(b) Histogram

Figure 5.21: Spiral wave tip speed for discordant alternans.

Figure 5.21 shows that when breakup took place by the formation of discordant alternans, the range of speeds assumed by the spiral wave tips varied over a large range of values between 0.01cm/ms and 0.06cm/ms. The maximum speed observed for this case was almost 0.06cm/ms. Note how in both cases where breakup was induced by steep-APD-restitution, the range of average speeds of the spiral wave tips observed for the system were almost the same.

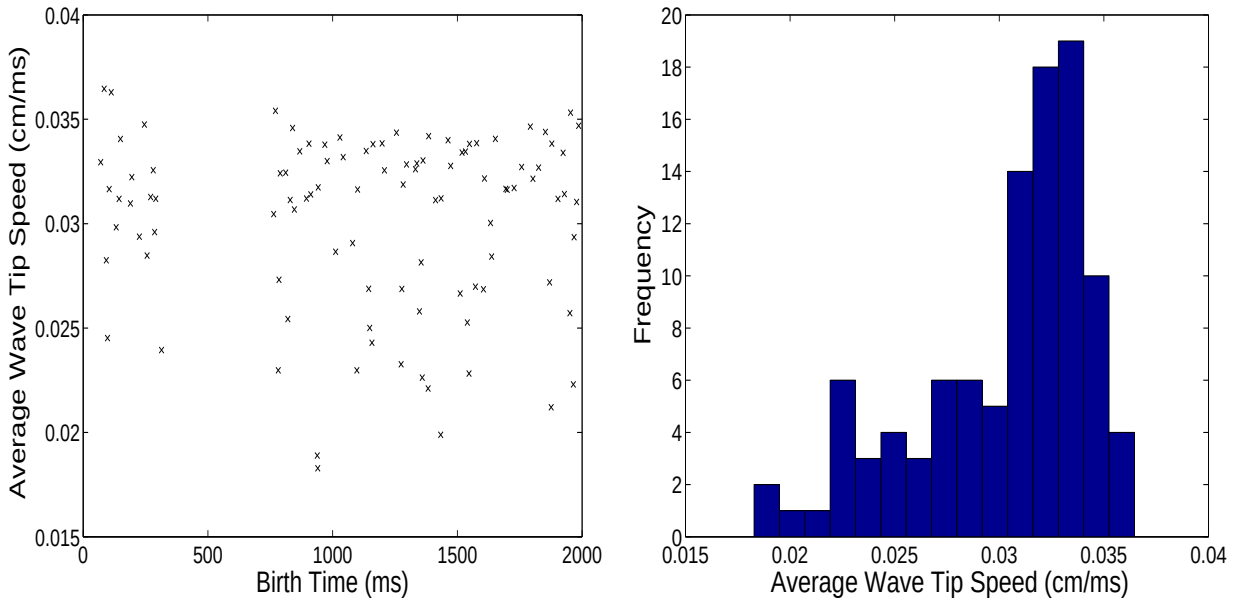

(a) Time series distribution of spiral wave tip speed

(b) Histogram

Figure 5.22: Spiral wave tip speed for bistability.

From Figure 5.22, it is observed that a majority of the spiral wave tips in the case of bistability had an average speed of 0.03cm/ms to 0.035cm/ms. A fair number of spiral wave tips also took on values between 0.02cm/ms and 0.03cm/ms. The maximum average speed of the spiral wave tips in this case was 0.036cm/ms.

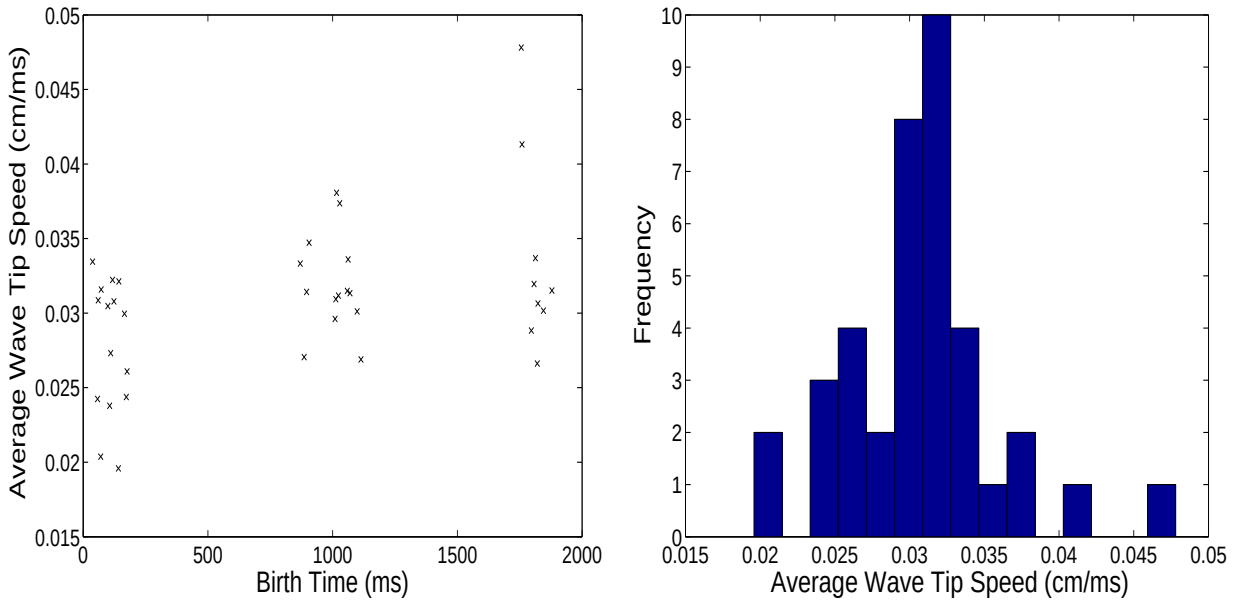

(a) Time series distribution of spiral wave tip speed

(b) Histogram

Figure 5.23: Spiral wave tip speed for Doppler effect.

Figure 5.23 shows that for the Doppler effect, a large number of spiral wave tips traveled at speeds of approximately 0.03cm/ms. The distribution of the spiral wave tip speeds appeared to be approximately normal with a minimum value of 0.02cm/ms and a maximum value of about 0.04cm/ms.

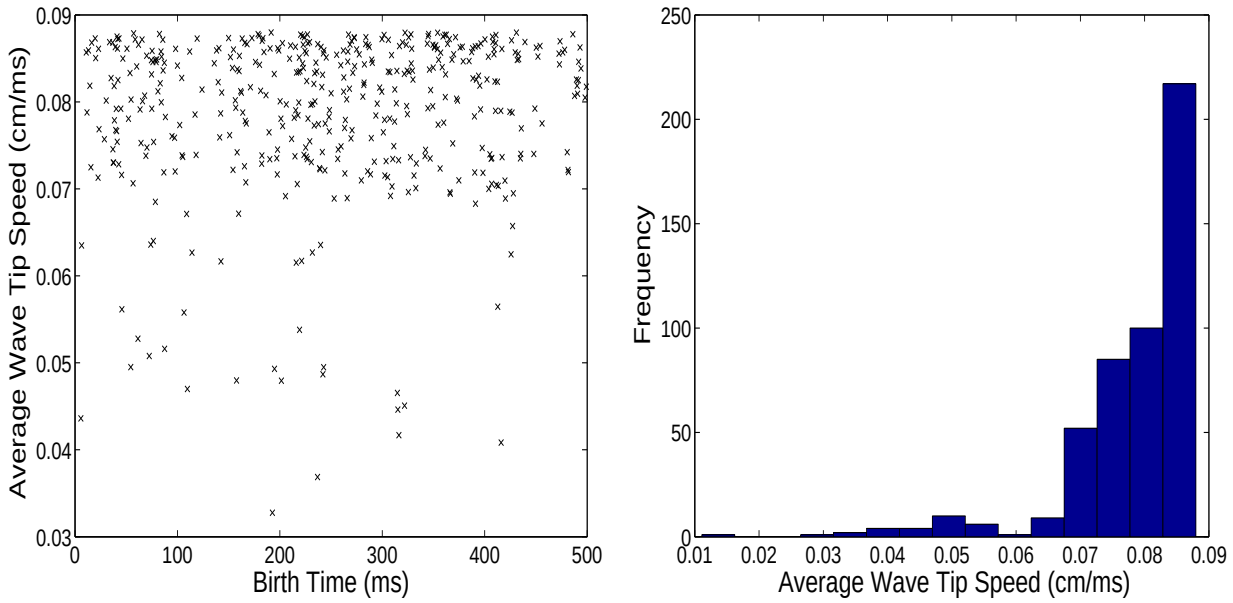

(a) Time series distribution of spiral wave tip speed

(b) Histogram

Figure 5.24: Spiral wave tip speed for supernormal conduction velocity.

From Figure 5.24, it is clear that the average spiral wave tip speed in the case of supernormal conduction velocity was higher when compared to the values obtained for the other mechanisms. The maximum average speed value obtained for this case was close to 0.09cm/ms, and there was also a fairly large number of waves that propagated at speeds between 0.07cm/ms and 0.09cm/ms.

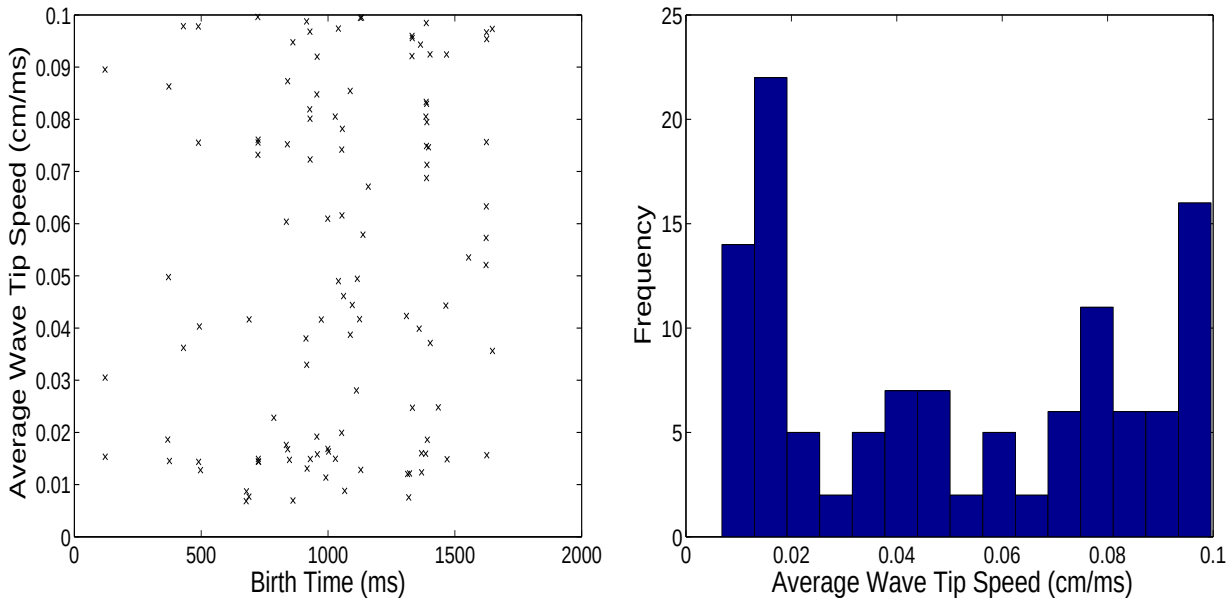

(a) Time series distribution of spiral wave tip speed

(b) Histogram

Figure 5.25: Spiral wave tip speed for periodic boundary conditions.

The average spiral wave speed for the case of periodic boundary conditions, as observed from Figure 5.25, appeared to fall in a range from 0.01cm/ms to 0.1cm/ms. The maximum average speed in the case of periodic boundary conditions was 0.1cm/ms, which was close to the value observed in the case of supernormal conduction velocity.

Chapter 6

Application of Metrics to Different Models

As seen in Chapter 5, we were able to quantify breakup using different metrics. Our next goal is to show that the results of applying the metrics to the cases where the breakup mechanisms are known can be used to identify the breakup mechansims in other scenarios for which they are not known. Toward that end, we carried out a blind test wherein given the time series of V_m values measured every 0.25ms for a total duration of 2s and the coordinates of spiral wave tips recorded every 1ms, corresponding to four different datasets from breakup scenarios with established breakup mechanisms withheld initially, we quantified breakup episodes using each of the methods discussed in Chapter 5. The purpose of this experiment was to determine whether we could successfully identify the mechanism responsible for breakup based solely on the quantification of observed properties. After considering the data and reaching a decision with regard to the underlying mechanism for each case, the initially withheld mechanisms were revealed. Figure 6.1 shows a snapshot of the breakup obtained using the given datasets.

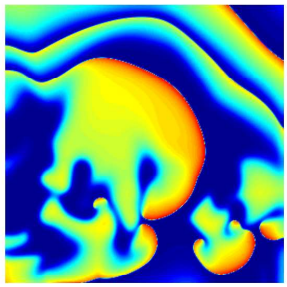

(a) Dataset 1

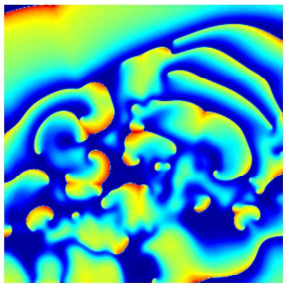

(b) Dataset 2

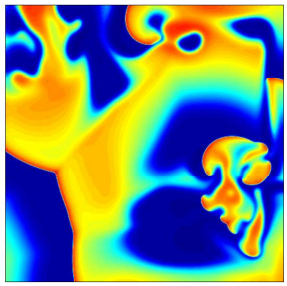

(c) Dataset 3

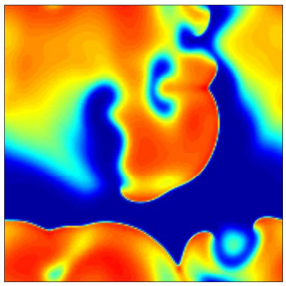

(d) Dataset 4

Figure 6.1: Snapshot of the breakup obtained using (a) Dataset 1 (b) Dataset 2 (c) Dataset 3 (d) Dataset 4.

Below we discuss the process followed for selecting a candidate mechanism for each given breakup scenario.

6.1 Dataset 1

1. Number of Spiral Waves

   Figure 6.2 shows the distribution of the number of spiral waves over time. Until t=1000ms, we see a very slight variation in the number of waves. From t=1000msec, a more rapid growth is seen in the number of spiral waves, which reaches a maximum value of 14. Also, past 1000ms, the number of waves does not remain constant for more than a few hundreds of ms. This behaviour makes the scenario seem similar to breakup induced by the Doppler effect or periodic boundary conditions.

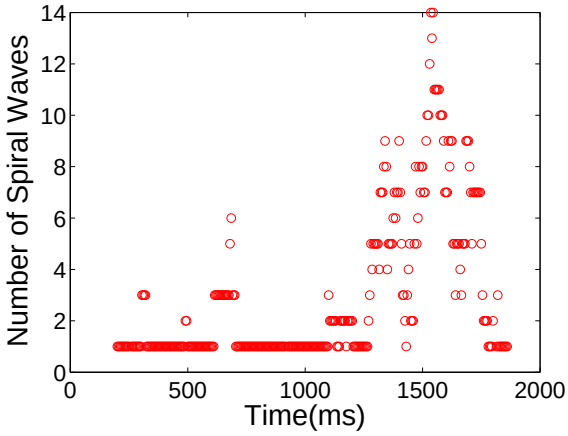

Figure 6.2: Dataset 1: Number of spiral waves.

2. Lyapunov Exponent

   The largest Lyapunov exponent that was obtained for this model was 0.0874. This value was closest to what we obtained previously for the Doppler effect.

3. Mutual Information

   Figure 6.3 shows the mutual information for Dataset 1. Much like Figure 5.5, during the interval 0-500ms, there is a combination of high and low mutual information values. The higher values of information are due to the fact that there is mostly a single wave present through most of this time interval with bouts of breakup. From 500ms to 1000ms, as the

breakup increases, a decrease in the mutual information values is observed which continues for the rest of the simulation. This transition from the beginning of the simulation to the end makes this scenario more likely to be caused by the Doppler effect, as it exhibited similar behaviour.

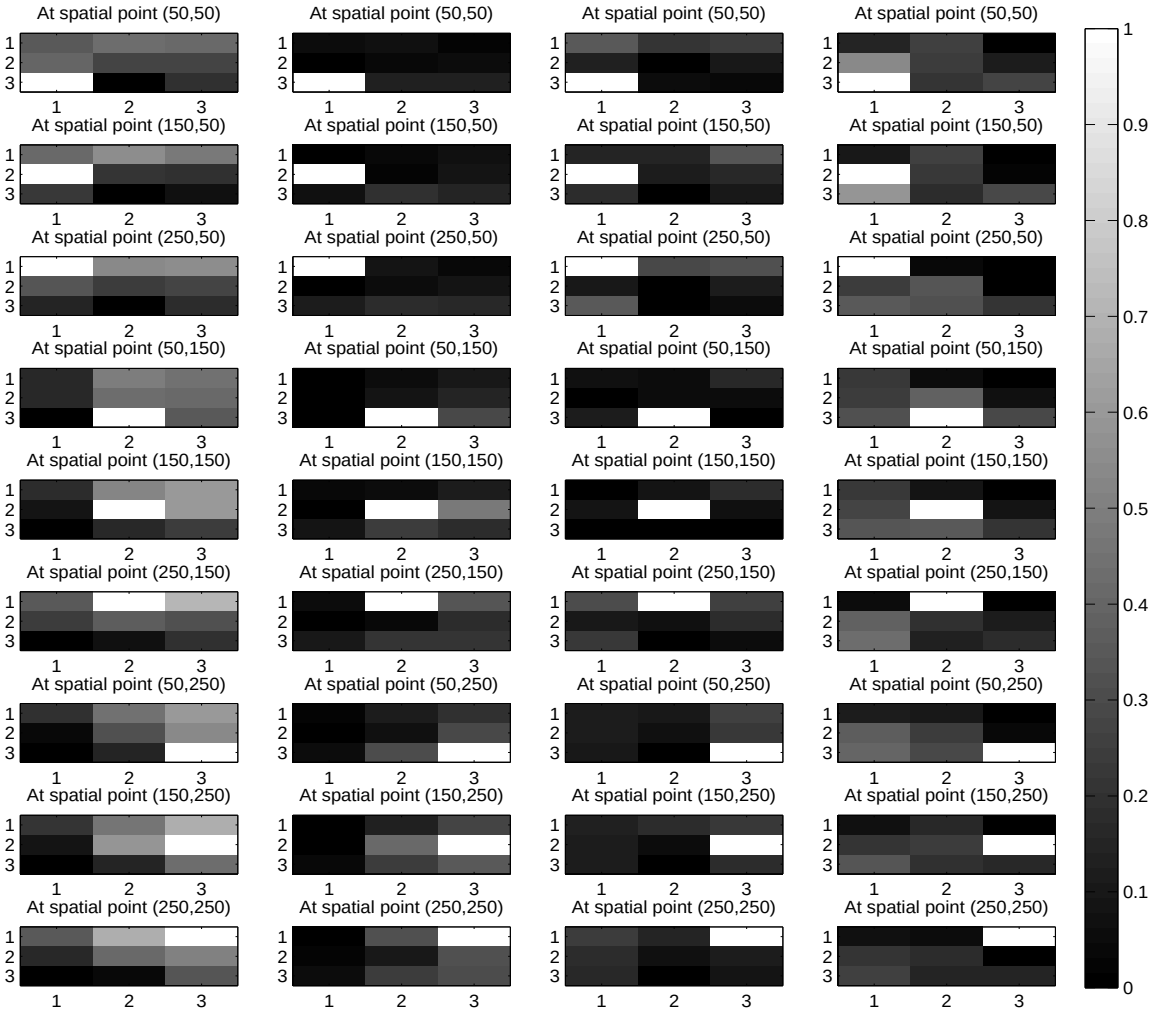

Figure 6.3: Dataset 1: Mutual information.

4. Spatial Correlation

Figure 6.4, showing the change in spatial correlation over time for Dataset 1, is characterized

by higher correlation values in the first time interval from 0 to 500ms. As the simulation proceeds over time, the dependency values become lower. Like our previous observations for Figure 6.3, this behaviour is consistent with what we saw earlier with the Doppler effect, i.e., starting off the simulation with fairly high correlation values which decrease over time.

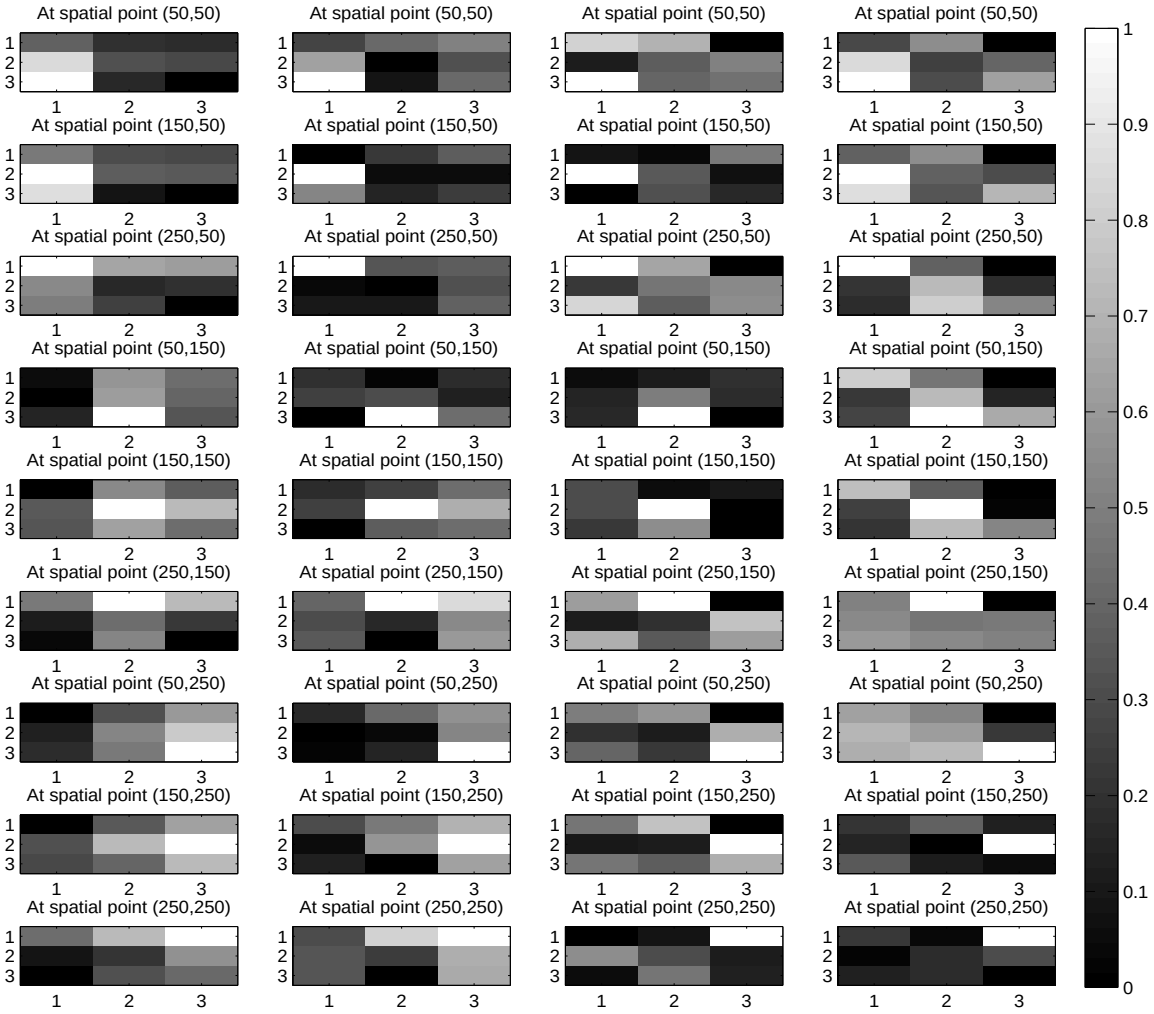

Figure 6.4: Dataset 1: Spatial correlation.

5. Birth Rate, Death Rate and Spiral Wave Lifetime

   The birth rate and death rate values obtained for this dataset are 0.216216ms $^{-1}$ and 0.213213ms^{-1}, respectively. Similar to our observations in Section 5.5, the birth and death rates for Dataset 1 are almost equal and lie in the same range as the values seen for steep APD restitution and Doppler effect.

   Figure 6.5 shows the distribution of spiral wave lifetimes as a function of their corresponding birth times along with the frequency distribution of the lifetimes.

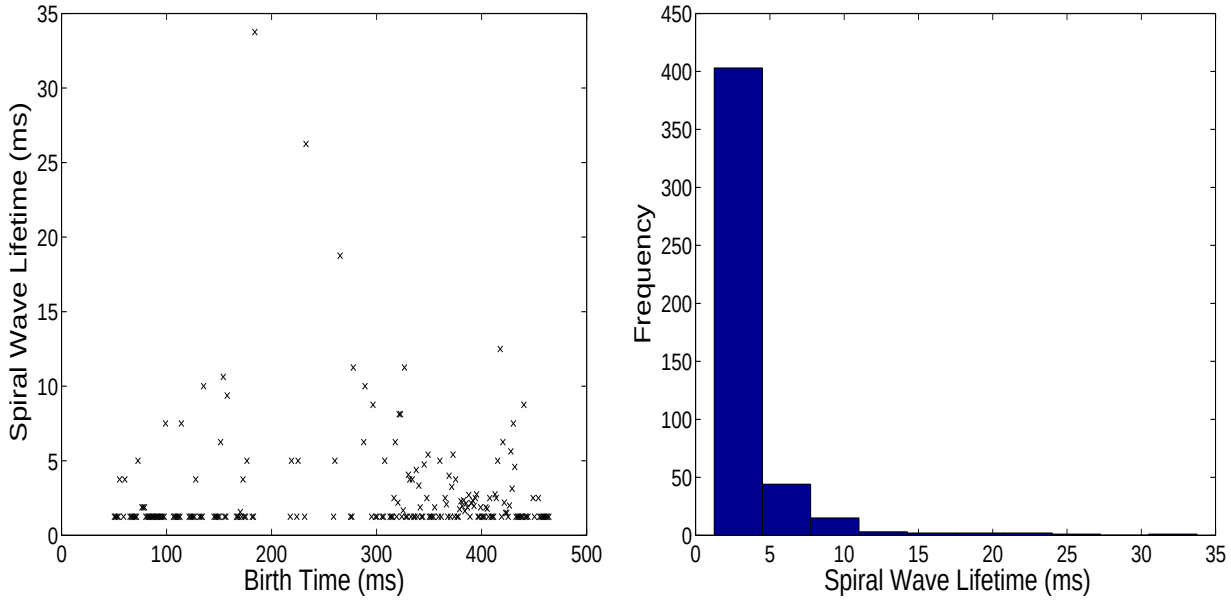

(a) Time series distribution of wave lifetime

(b) Histogram

Figure 6.5: Dataset 1: Spiral wave lifetime.

   For Dataset 1, most of the spiral waves were in existence for less than 20ms, much like the spiral wave lifetime values observed for the Doppler effect.

6. Spiral Wave Tip Speed

   Figure 6.6 shows the distribution of the average spiral wave tip speed over time along with the frequency distribution of the speeds.

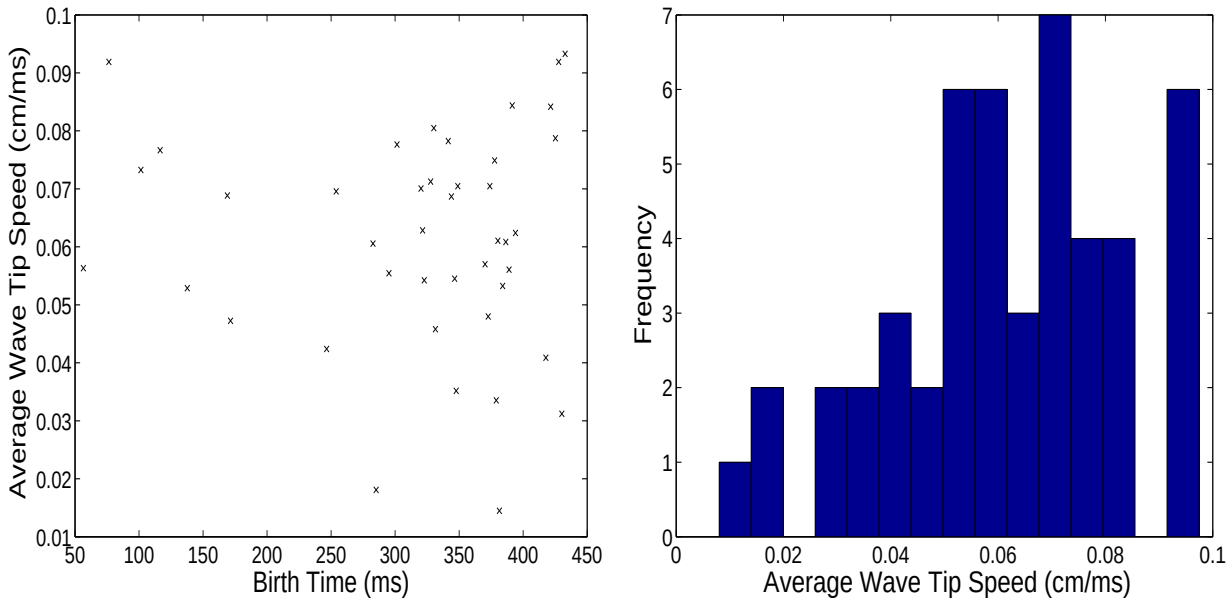

(a) Time series distribution of spiral wave tip speed

(b) Histogram

Figure 6.6: Dataset 1: Spiral wave tip speed.

Figure 6.6 shows that the average speed of the spiral wave tips was in the range 0.03-0.08cm/ms with some waves taking on higher and lower values. The range of the spiral wave tip speeds was mostly 0.01-0.1cm/ms, making it most similar to the distribution observed for periodic boundary conditions.

Based on all the plots, we narrowed down our results to looking at one mechanism that matched most closely with the results of Dataset 1, which was the Doppler effect. Seeing that a majority of the results from applying the metrics pointed towards the Doppler effect being the underlying mechanism of breakup, that was our classification for this dataset, which turned out to be correct. Dataset 1 was obtained using the Luo-Rudy model [52] with the calcium current time constants decreased to 0.8 times their original values, and it exhibited breakup by the Doppler effect [5].

6.2 Dataset 2

1. Number of Spiral Waves

   Figure 6.7 shows the distribution of the number of spiral waves over time.

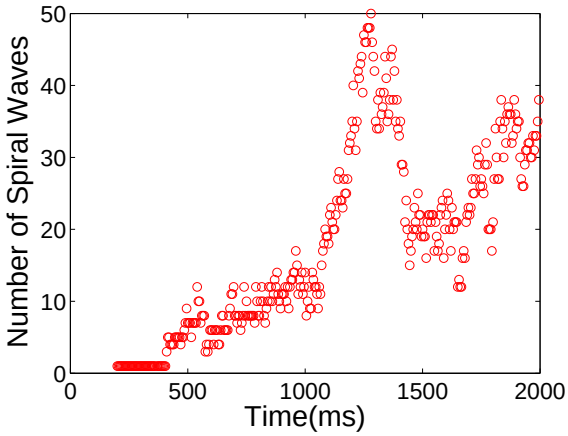

Figure 6.7: Dataset 2: Number of spiral waves.

   The distribution resembles very closely the behaviour that was observed in the case of steep APD restitution. As the figure makes clear, the number of waves increases over time with a spike in the time interval 1000-1500ms. The rest of the figure, if observed closely, also exhibits the alternating pattern that was seen previously for that mechanism.

2. Lyapunov Exponent

   The largest Lyapunov exponent obtained for this dataset was 0.0522. The positive value in this case is indicative of irregular behaviour present in the system, but is not particularly close to any of the Lyapunov exponent values seen previously for all the breakup mechanisms.

3. Mutual Information

   Figure 6.8 shows the plot of mutual information for Dataset 2.

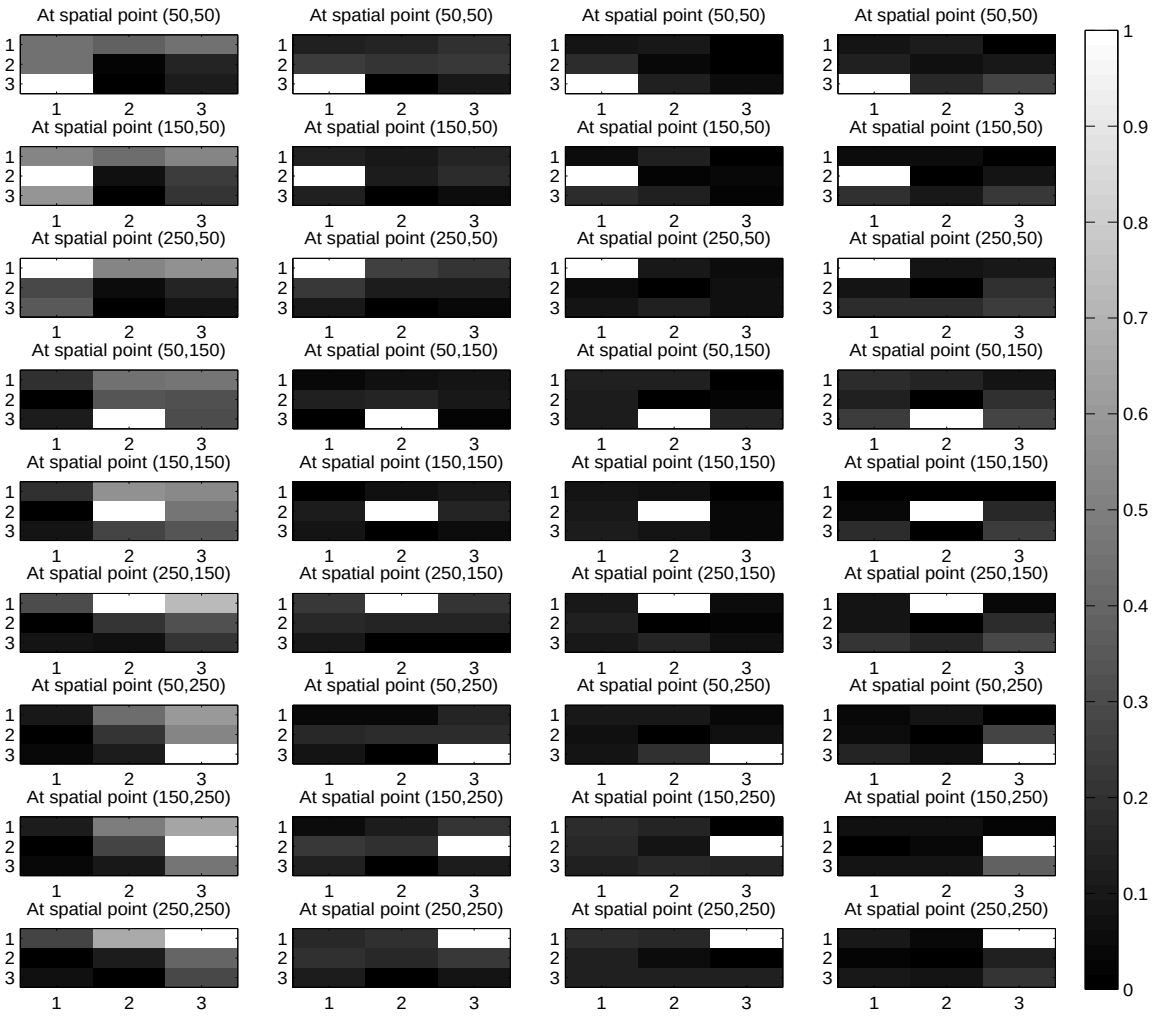

Figure 6.8: Dataset 2: Mutual information.

In the range 0 to 500ms, there is some amount of information that is shared. This is also due to the fact that in this initial time interval, there is not much breakup observed. As the time increases, breakup begins to take place and mutual information decreases correspondingly. Decreased mutual information values are present for the rest of the simulation as well, which is consistent with the irregular behaviour that is seen in the distribution of spiral waves due to an increase in spiral wave breakup. This behaviour is almost the same as that exhibited

by steep APD restitution.

4. Spatial Correlation

   Figure 6.9 shows the spatial correlation values measured for Dataset 2. Once again, just like in the case of steep APD restitution, the highest correlation values are observed in the first 500ms. As the simulation proceeds, the spatial correlation only decreases as the breakup in the system increases.

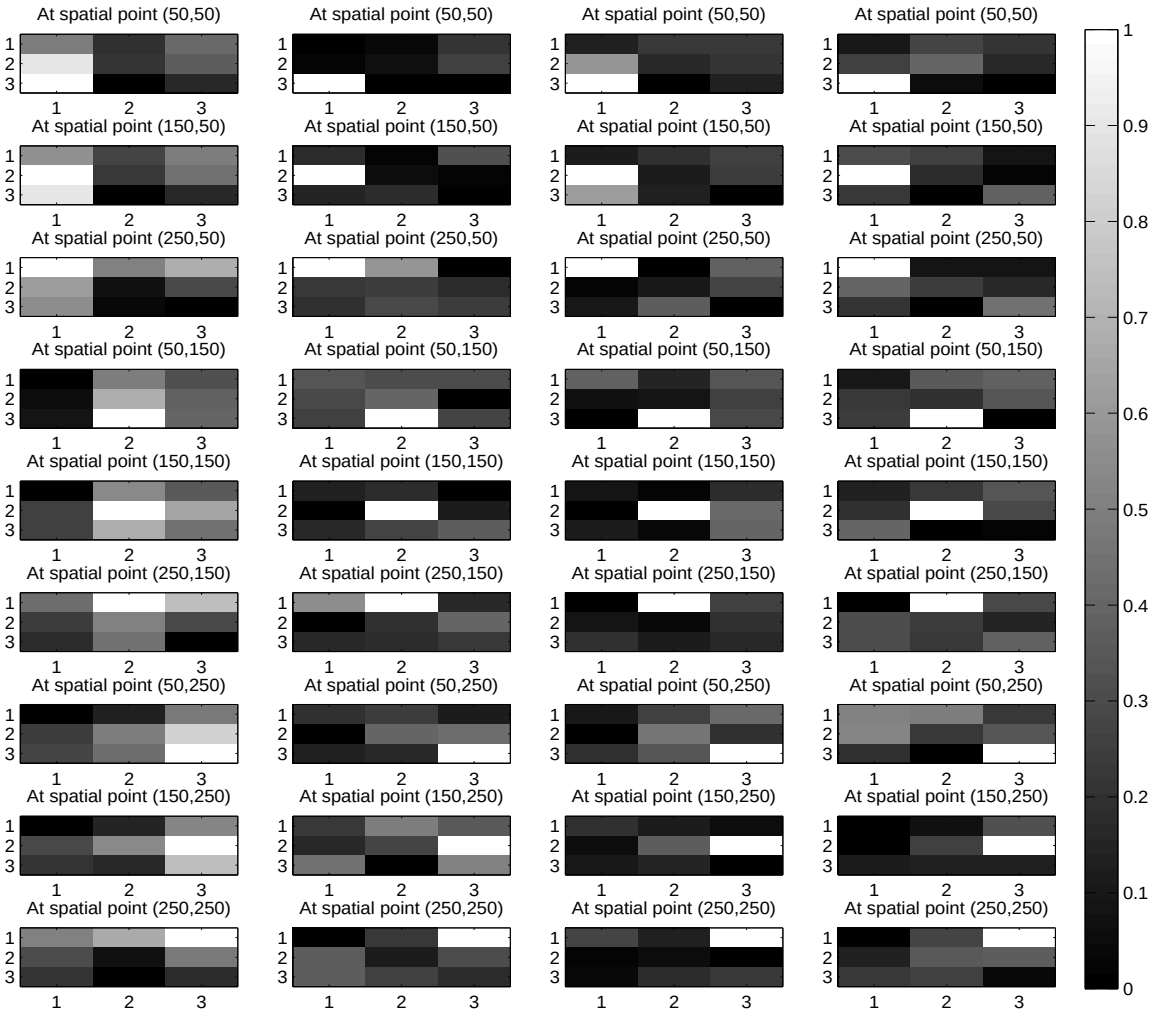

Figure 6.9: Dataset 2: Spatial correlation.

5. Birth Rate, Death Rate and Spiral Wave Lifetime

   For Dataset 2, the values that we obtained for the birth rate and death rate were $2.277778ms^{-1}$ and $2.172222ms^{-1}$, respectively.

   Figure 6.10 shows the distribution of spiral wave lifetimes along with the frequency distribution of the lifetimes.

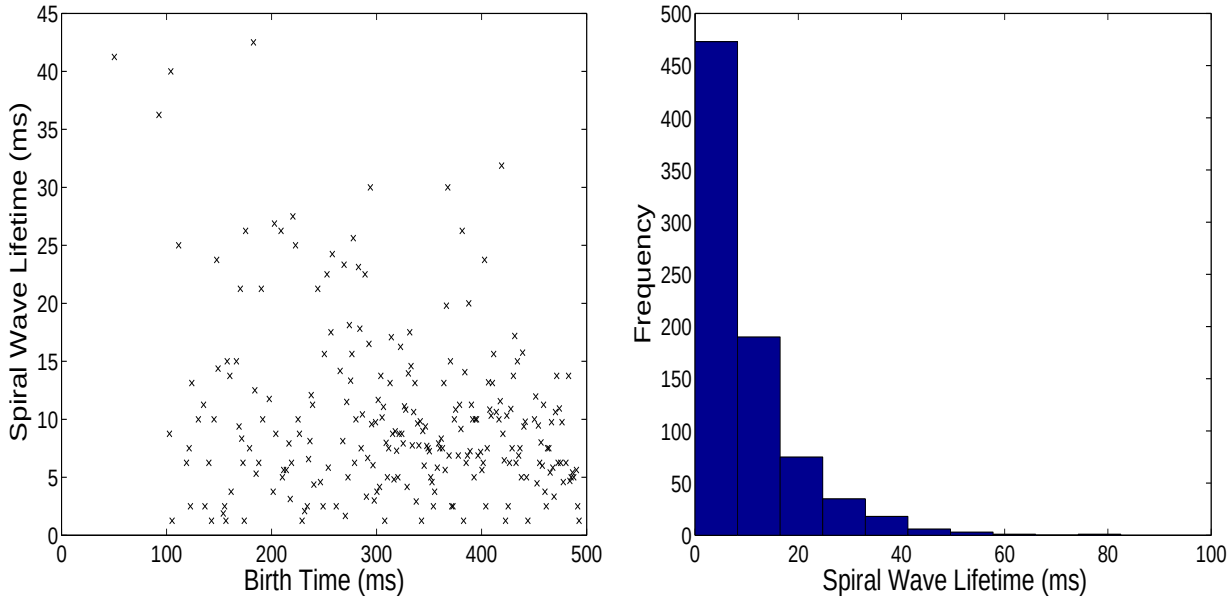

(a) Time series distribution of wave lifetime

(b) Histogram

Figure 6.10: Dataset 2: Spiral wave lifetime.

Dataset 2 showed very high values for birth and death rates that did not explicitly match any of the values that we observed previously, but the distribution of the spiral wave lifetimes was more helpful in this case. From Figure 6.10 , we were able to gauge that this dataset possessed similarities with the behaviour exhibited by steep APD restitution. Most of the spiral waves had a lifetime that ranged from 0 to 50ms.

6. Spiral Wave Tip Speed

   Figure 6.11 shows the distribution of the average spiral wave tip speeds over time along with

the frequency distribution of the speeds.

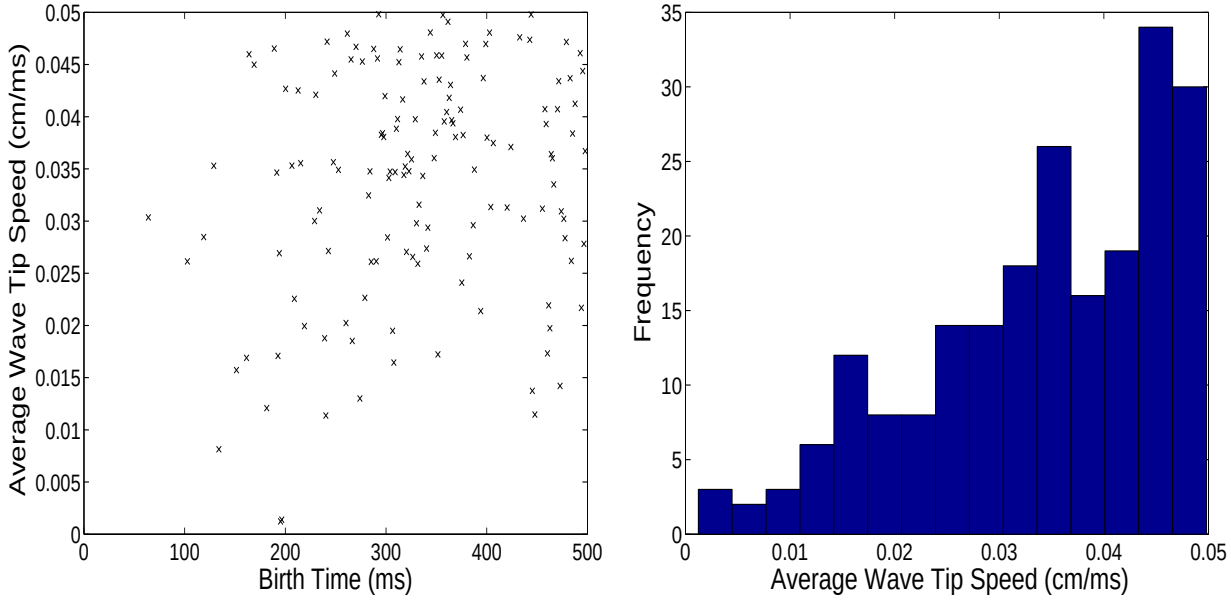

(a) Time series distribution of spiral wave tip speed

(b) Histogram

Figure 6.11: Dataset 2: Spiral wave tip speed.

The distribution of the spiral wave tip speeds matched very closely with the distributions observed for steep APD restitution and discordant alternans. Most of the speeds fell in the range of 0-0.05cm/ms.

Based on all the measurements, this dataset closely matched most of the metrics seen in the case of steep APD restitution. Although the Lyapunov exponent was not very helpful in this case, the other metrics agreed quite well. Dataset 2 was, in fact, the Luo-Rudy model [52] modified to have steep restitution, as specified in Ref. [5], with steep-APD-restitution-induced breakup close to the spiral tip.

6.3 Dataset 3

1. Number of Spiral Waves

   Figure 6.12 shows the distribution of spiral waves over time for Dataset 3. In this case, the growth in the number of waves is slow until t=750ms, after which the number of spiral waves primarily increases, possibly exhibiting an alternating-like pattern similar to what was observed for steep APD restitution.

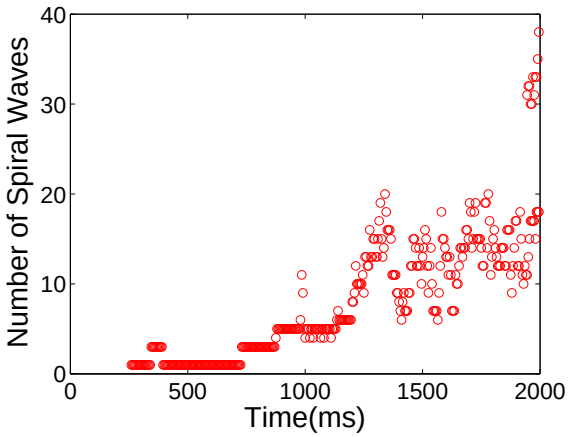

Figure 6.12: Dataset 3: Number of spiral waves

2. Lyapunov Exponent

   The largest Lyapunov exponent that was obtained for this model was -0.0274. The negative value suggests that the kind of breakup seen in this case is due to bistability.

3. Mutual Information

   Figure 6.13 shows the plot of mutual information for Dataset 3. Low values of mutual information are present in most parts of the domain between 0 and 500ms. Over the next few time intervals, the mutual information values are seen to increase, which is not consistent with the behaviour observed in Figure 6.12. Due to this inconsistent behaviour, we were not able to make any useful guess towards the breakup mechanism that was prevalent in Dataset 3 based on mutual information.

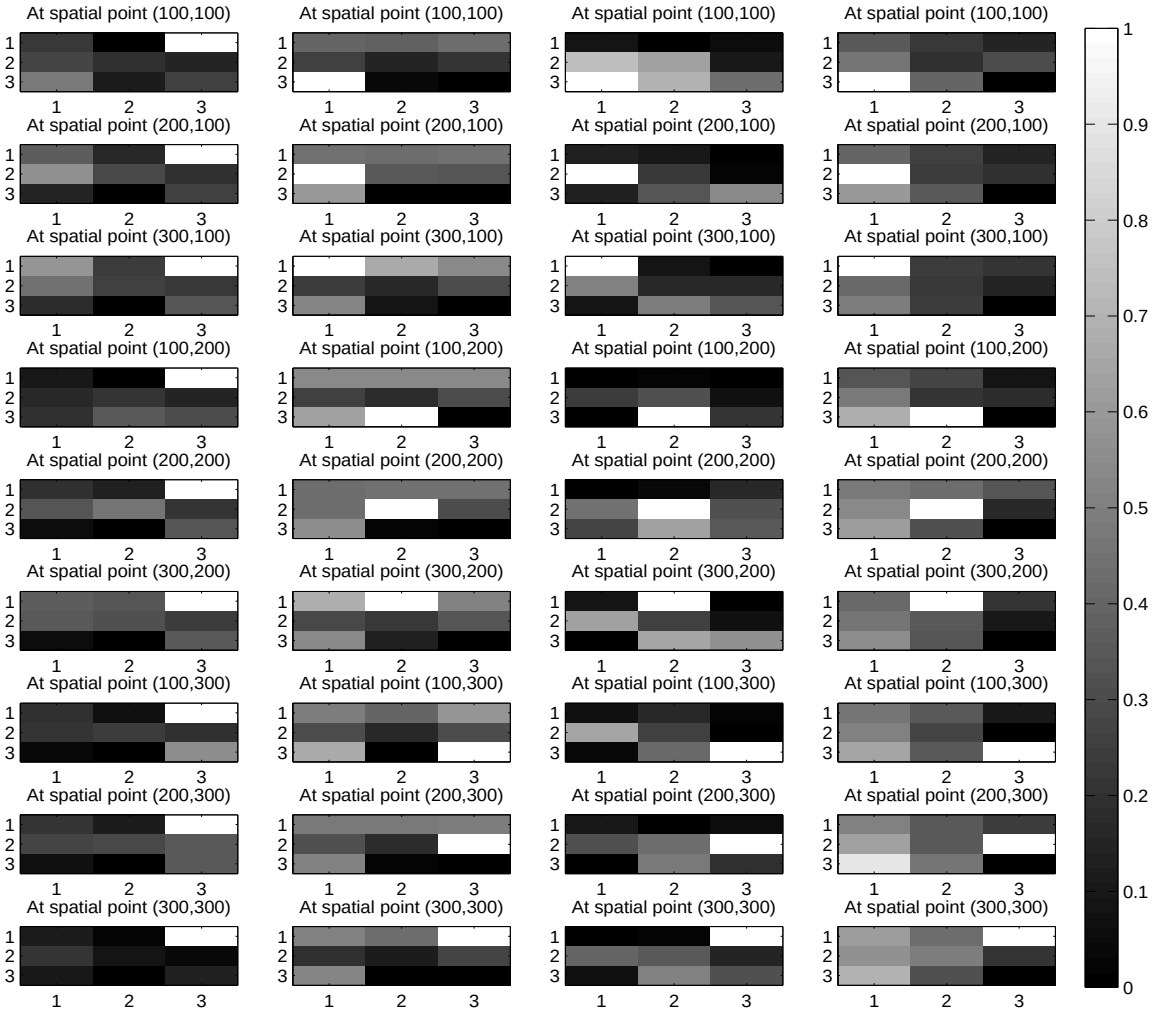

Figure 6.13: Dataset 3: Mutual information

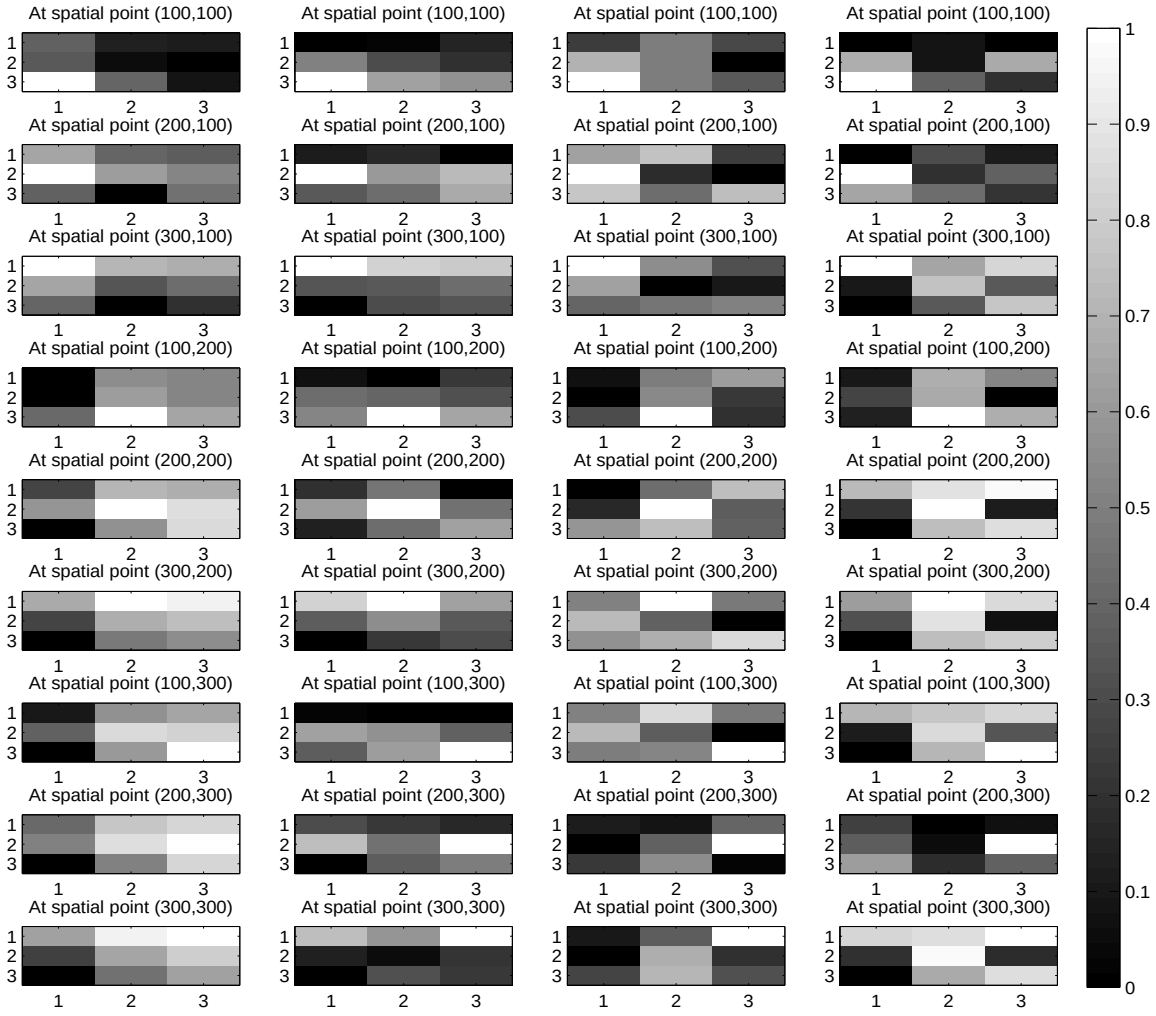

Figure 6.14: Dataset 3: Spatial correlation

From Figure 6.14, it can be seen that the correlation values in the range 0-500ms are higher when compared with the next time interval. Between 500ms and 1000ms, the correlation takes on comparatively lower values which continues on to the interval 1000-1500ms. There is a transition once again to higher correlation values in the last part of the simulation. This

behaviour appears to be similar to what was observed in Figure 5.13 for the case of periodic boundary conditions.

5. Birth Rate, Death Rate and Spiral Wave Lifetime

   The birth and death rates obtained for Dataset 3 were $0.801724ms^{-1}$ and $0.750000ms^{-1}$.

   Figure 6.15 shows the distribution of spiral wave lifetimes as a function of their birth times along with the frequency distribution of the lifetimes.

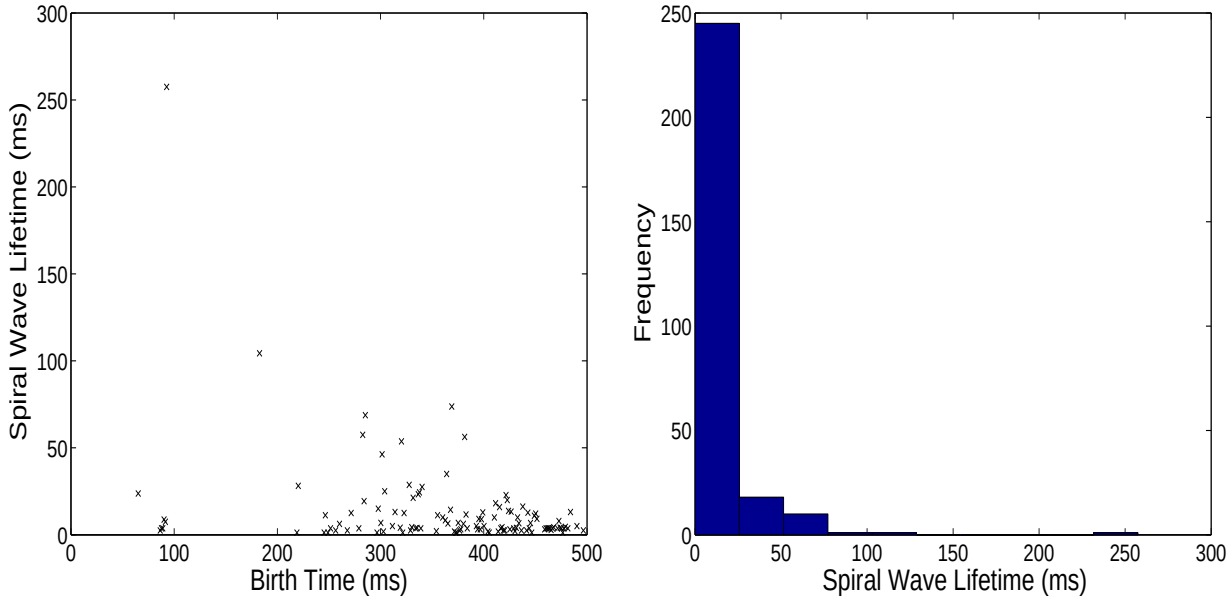

(a) Time series distribution of wave lifetime

(b) Histogram

Figure 6.15: Dataset 3: Spiral wave lifetime.

Dataset 3 showed high values for birth and death rates that did not match any of the values obtained for the mechanisms discussed in Chapter 5. Most of the spiral waves had a lifetime that was in the range 0-200ms, of which most of the waves lasted for less than 100ms, which made it seem similar to the behaviour observed for bistability.

6. Spiral Wave Tip Speed

Figure 6.16 shows the distribution of the average spiral wave tip speeds over time along with the frequency distribution of speeds.

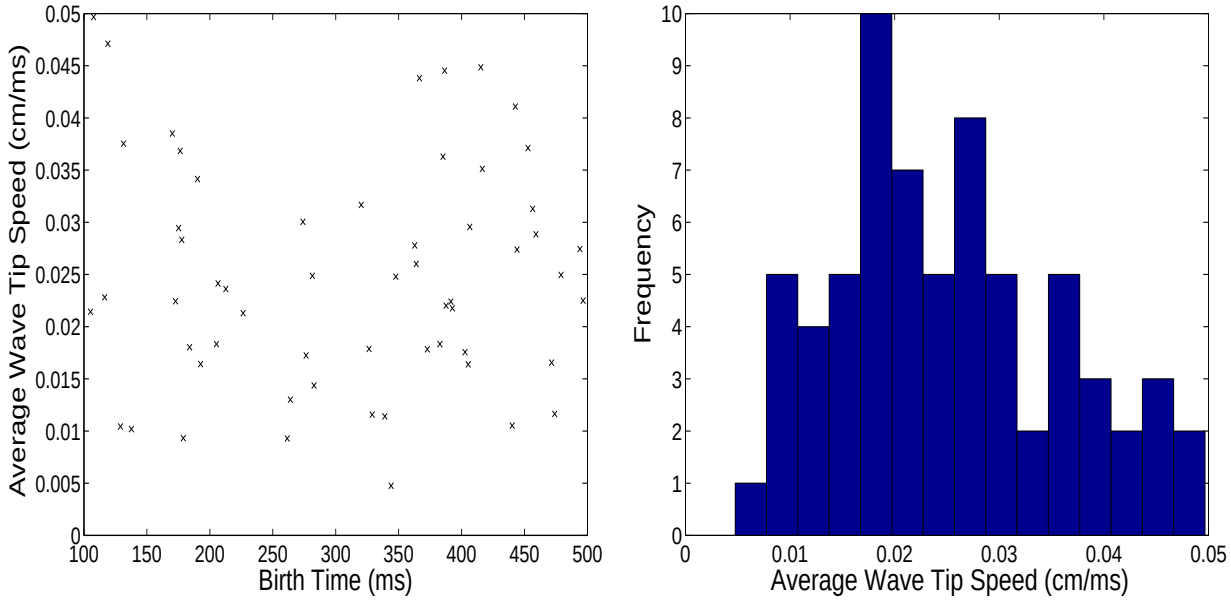

(a) Time series distribution of spiral wave tip speed

(b) Histogram

Figure 6.16: Dataset 3: Spiral wave tip speed

Most of the average spiral wave tip speeds fall within the range of 0.01-0.05cm/ms, which lies closest to the behaviour that was observed for steep APD restitution and discordant alternans.

Based on all the measurements, we found it particularly difficult in this case, to narrow down our results to looking at only certain mechanisms. From our observations of Dataset 3, we found that the measurements showed similarities with a large number of mechanisms, and the best guess that we were able to make as the mechanism responsible for the breakup observed in Dataset 3 was bistability. Our guess was incorrect in this case, as Dataset 3 was the original Beeler-Reuter model [25], which gives rise to steep-restitution-induced breakup close to the tip, as discussed in Ref. [5].

6.4 Dataset 4

1. Number of Spiral Waves

   As shown in Figure 6.17, there is varied activity in the distribution of the number of spiral waves over time. After t=250ms, rapid breakup occurs and is characterized by a large number of waves throughout the simulation, reaching a maximum of 10. This behaviour is almost the same as what we observed in the case of periodic boundary conditions (see Figure 5.1f).

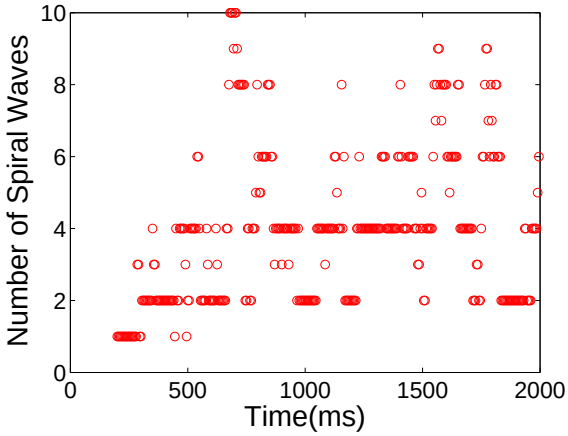

Figure 6.17: Dataset 4: Number of spiral waves

2. Lyapunov Exponent

   The largest Lyapunov exponent that was obtained for this model was 0.1189. This positive value puts it closest to the Lyapunov exponent obtained for steep APD restitution.

3. Mutual Information

   Similar to our observation for the mutual information plot for periodic boundary conditions in Figure 5.7, the time interval 0-500ms shows a combination of a small number of high but mostly low mutual information values. As the simulation proceeds and breakup increases, the values decrease further between 500ms and 1500ms. In the last time interval, we note a decrease in the number of waves, as indicated by the increase in the mutual information values.

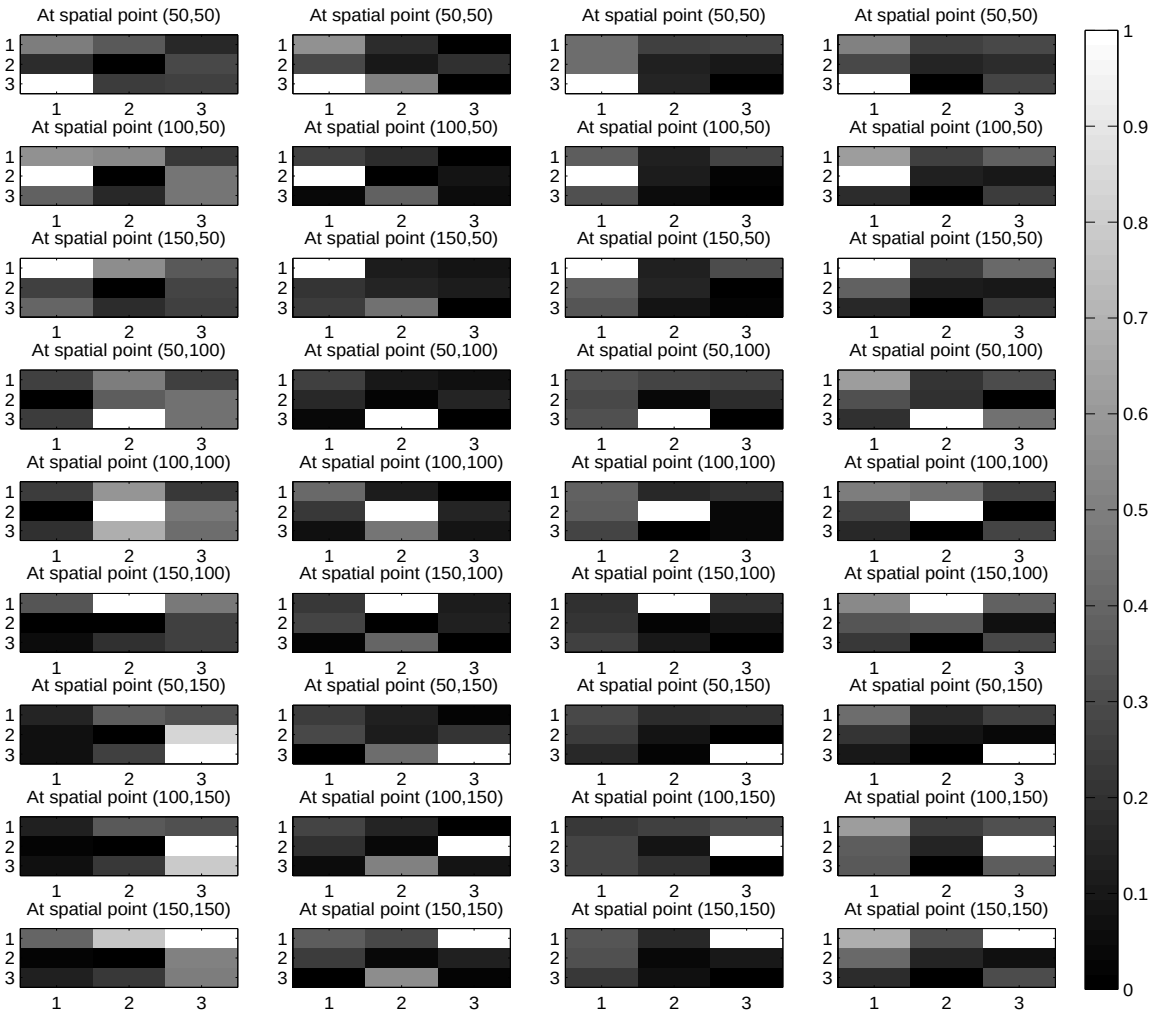

Figure 6.18: Dataset 4: Mutual information

4. Spatial Correlation

   In Figure 6.19, from 0 to 500ms, there is a presence of higher correlation values. About halfway through the simulation, most of the domain is governed by low values of correlation. From 1000-1500ms, higher values of correlation return in some parts of the domain; however, most of the domain still has low values due to the breakup. The last interval of the simulation shows some increase in the correlation values similar to what was seen in the case of periodic

boundary conditions.

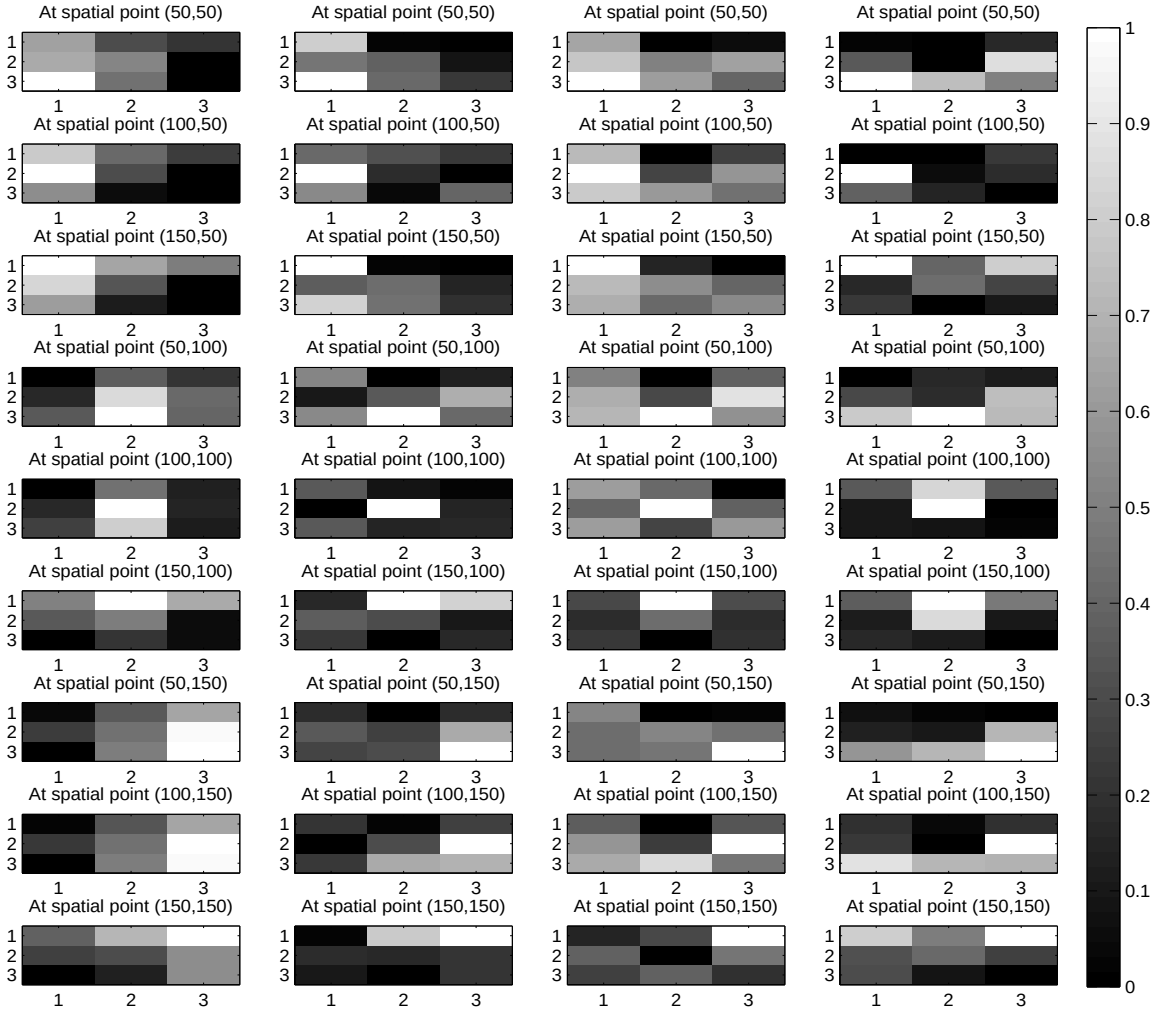

Figure 6.19: Dataset 4: Spatial correlation

5. Birth Rate, Death Rate and Spiral Wave Lifetime

   The birth and death rates obtained for Dataset 4 were $0.433333ms^{-1}$ and $0.416667\ ms^{-1}$, respectively.

   Figure 6.20 shows the distribution of spiral wave lifetimes as a function of the birth times along with the frequency distribution of the lifetimes.

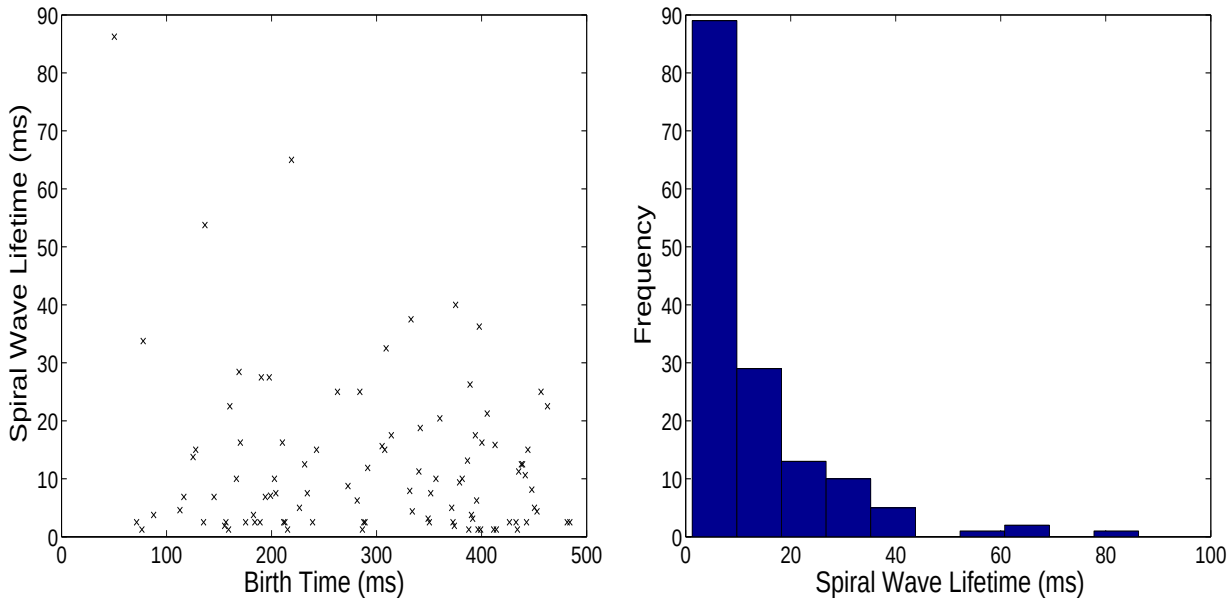

(a) Time series distribution of wave lifetime

(b) Histogram

Figure 6.20: Dataset 4: Spiral wave lifetime

For Dataset 4, the birth and death rate values matched very closely with the values that were obtained for periodic boundary conditions. In addition to this, the lifetime of the waves mostly revolved around the range 0-100ms, which was again a property that was observed for periodic boundary conditions.

6. Spiral Wave Tip Speed

   Figure 6.21 shows the distribution of the average spiral wave tip speeds over time along with the frequency distribution of speeds.

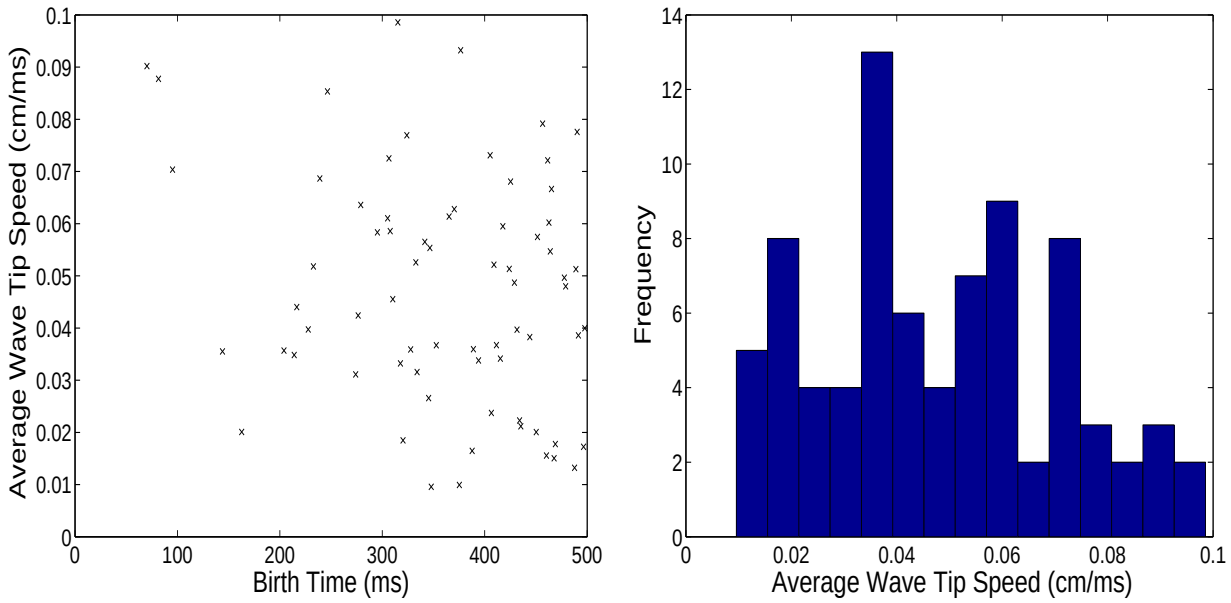

(a) Time series distribution of spiral wave tip speed

(b) Histogram

Figure 6.21: Dataset 4: Spiral wave tip speed

In this case, the distribution of the spiral wave tip speeds resembles the behaviour that was seen in the case of periodic boundary conditions very closely, as the average speed for both cases lies in the range of 0.01cm/ms to 0.1cm/ms.

Based on all the measurements, with the exception of the Lyapunov exponent, all the metrics pointed towards periodic boundary conditions being the mechanism behind the breakup observed in the case of Dataset 4. Dataset 4 was the modified Beeler-Reuter model [25] with the time constants for the calcium current doubled, and as discussed in Ref. [5], it gave rise to breakup with (and not without) periodic boundaries.

Chapter 7

Discussion and Conclusion

Ventricular fibrillation (VF) is known to be the most dangerous type of arrhythmia; it can cause sudden cardiac death. Understanding the intricacies of this condition would help in developing better prevention strategies and cures. Despite the extensive research in this field, the exact mechanisms behind the breakup of spiral waves and the initiation of fibrillation are still not clearly understood. Various mathematical modeling and computational approaches have been helpful in demonstrating a number of different dynamical mechanisms that could give rise to breakup, but classifying these in an experimental setting has been a challenge in part due to limitations in obtaining data. Discerning among different mechanisms of breakup visually is nearly impossible. Thus, being able to narrow down possible mechanisms based on measurable properties would be very useful. Our work forms a preliminary step in this direction and was developed with the idea that all results could be extended to experimental results in a straightforward manner; all data used in quantifying breakup would be accessible from standard optical-mapping experiments.

In this thesis, we studied the electrical system of the heart focusing on different aspects of fibrillation like the action potential, reentry and the dynamics of the fibrillating heart. Visual representations of the various breakup mechanisms helped us understand how fibrillation occurs under different initial conditions like steep APD restitution, supernormal conduction of action potentials and periodic boundary conditions. The Fenton-Karma model aided in simulating the breakup mechanisms because it has been shown previously to give rise to breakup by each mechanism

considered in specific parameter ranges, independently of other mechanisms. Studying the different types of spiral wave breakup helped in choosing certain metrics that were utilized to enhance our understanding of how fibrillation develops and how it proceeds over time. The metrics studied were the number of spiral waves, Lyapunov exponents, mutual information, spatial correlation, spiral wave lifetimes and spiral wave tip speeds. Some of these metrics were used to measure the irregularities of the system during wave breakup while others were used to measure the properties of spiral waves. The metrics were applied to cases in which the breakup mechanism was known to study the results produced by each mechanism and particularly how different they were from each other. To check the robustness and effectiveness of the metrics, they were subsequently applied to different models such that the results of the metrics in cases where the breakup mechanism was known was used to identify the underlying breakup mechanisms in cases for which they were not known beforehand but were verified subsequently.

7.1 Usefulness of Metrics

Through the application of the metrics to different models, it was found that not all the metrics provided the same degree of information and insight into the underlying mechanisms present during the breakup of spiral waves. Certain metrics were more essential than others, in providing a direction towards the classification. The metric that was, in isolation, able to provide the most information about the underlying mechanism was the distribution of the number of spiral waves over time. The manner in which the distribution changed over time helped in narrowing down our the options while trying to differentiate among different mechanisms of breakup. Steep APD restitution almost always showed an increase in the number of waves over time; on the other hand, discordant alternans did not show as much breakup, which could perhaps change if the mechanism of discordant alternans was implemented using different initial conditions. Doppler effect, supernormal conduction velocity and periodic boundary conditions showed a similar distribution of spiral waves over time, where the wave breakup was irregular. In these cases, breakup was observed throughout the simulation unlike, in the cases of bistability or discordant alternans. So, to summarize, if the number of waves changes significantly through the course of the simulation, we expect it to exhibit

the Doppler effect, supernormal conduction velocity or periodic boundary conditions. If the number of waves increases over the simulation, it possibly exhibits steep APD restitution. If the number of waves is constant during some parts and changing through the rest of the simulation, it could be expected to have discordant alternans or bistability as the underlying breakup mechanism.

The largest Lyapunov exponent for the system, in principle, is an effective way of capturing quantifying the chaos in the system; however, when this metric was applied to our data, it did not match our expectations based on the voltage images. It was clear that steep APD restitution showed more irregular behaviour in comparison with discordant alternans, but on computing the largest Lyapunov exponent values for the two, the latter seemed to have a higher value. While positive exponents are said to indicate chaos in the system, this may not always be true in experimental settings, as noisy data can also lead to falsely positive exponent values [53]. As a result, given these limitations, we found that this metric is not useful for classifying breakup mechanisms.

The mutual information and spatial correlation were useful metrics to determine the breakup mechanism under consideration. They are indicative of how, dynamics of the system change during the simulation and . They are useful to determine when and how the breakup proceeds over time. These metrics are especially useful when studied in context of the distribution of spiral waves over time. In isolation, the plots of mutual information and spatial correlation are difficult to interpret, as phases of the simulation characterized by limited wave activity or no activity at all can result in low mutual information and correlation values, and this may be confused with the system exhibiting lots of significant breakup, which can also results in low values. Using the distribution of the number of waves can help in discerning between the two situations and understanding the plots more accurately. Of the two metrics, mutual information is more reliable as it involves calculating the entropy and does not use the absolute values of voltage. The calculation of spatial correlation, on the other hand, involves using the absolute values of the voltage which may leave room for error if the simulation data has any outliers. In summary, mutual information, when studied together with the distribution of spiral waves over time, presents a more accurate picture of the breakup that occurs during simulations than when it is studied in isolation.the distribution of spiral waves alone .

Different properties of spiral waves were also examined to determine whether they would be useful in classifying underlying breakup mechanisms, and these properties varied in their usefulness. The birth and death rates for various datasets did not provide any useful results and their values were not indicative of any particular mechanism. In each case of breakup mechanisms, it was found that the birth and death rates were almost equal, and their absolute values were not very informative. Computing the lifetimes of the waves, however, was more useful, as some mechanisms like the Doppler effect had waves that were short-lived, whereas some mechanisms like discordant alternans and bistability had longer-lasting waves. Chapter 6 shows how two datasets operating under the same mechanism of spiral wave breakup exhibit similar values for spiral wave lifetimes (See Figures 6.5, 6.10, 6.20). Unlike spiral wave lifetimes, spiral wave tip speeds were not very useful in determining breakup mechanisms. The reason for this lies in the fact that two or more mechanisms exhibited a range of spiral wave tip speeds that overlapped, making it difficult to strictly classify mechanisms based on the values obtained for the speed.

7.2 Limitations

One of the main limitations faced during this thesis was the lack of training data. The availability of more data along with information about the breakup mechanism in each case would have enabled us to use a machine-learning algorithm to classify mechanisms based on other properties. These properties could be tested on data with known breakup mechanisms to check their robustness and the effectiveness of the classification scheme. Following this, the classification scheme could then be tested on datasets where the mechanisms are not known. However, a given breakup mechanism typically has not been established for more than 5-10 different models (or significantly different parameter regimes of a single model). Thus, using a machine-learning algorithm for our problem was not a viable option due to the lack of test data.

The use of only one dataset for each mechanism in Chapter 2 and one model for developing the metrics makes it more challenging to use our metrics for classifying mechanisms, because the robustness of our findings is not clear. Accessibility to more datasets for each of the mechanisms of spiral wave breakup will improve our understanding of how the breakup proceeds during simulations

and, in addition, will help in characterizing properties of the mechanisms like how the distribution of waves changes over time or the ranges of values that can be taken on by the spiral wave average tip speeds or lifetimes.

Other discrepancies arise from the challenges faced in identifying and tracking spiral wave locations during simulations. Inability to trace the trajectory of a single spiral wave over time leads to difficulties in computing metrics like spiral wave tip speeds and lifetimes. The method presented in this thesis for tracking a spiral wave tip trajectory depends on the usage of a threshold radius, a user- defined value. Depending on the radius selected, results could vary immensely and, for this purpose, a trial-and-error method has to be used to correctly select the threshold radius. If the radius is too large, not all the spiral waves in existence may not be counted, and if the radius is too small, it may result in double-counting. More effective waves techniques for of tracking spiral wave tip locations may eliminate the need to carry out a trial-and-error procedure, to correctly select the threshold radius.

In Chapter 6, we carried out a blind test on four given datasets, of which three were and classified three correctly. In the case of Dataset 3, for which we were unable to correctly identify the underlying breakup mechanism, the results of applying the different metrics yielded results that pointed towards 3-4 mechanisms. Under such circumstances, it is nearly impossible to make an initial guess towards the operating mechanism of breakup.

In experimental contexts, it may also be possible for 2 or more mechanisms to operate in concert to produce spiral wave breakup. Although this scenario was not explored in detail, we obtained some results from considering the combination of two mechanisms. A simple case in this direction involved implementing periodic boundary conditions with other mechanisms like steep APD restitution and the Doppler effect.

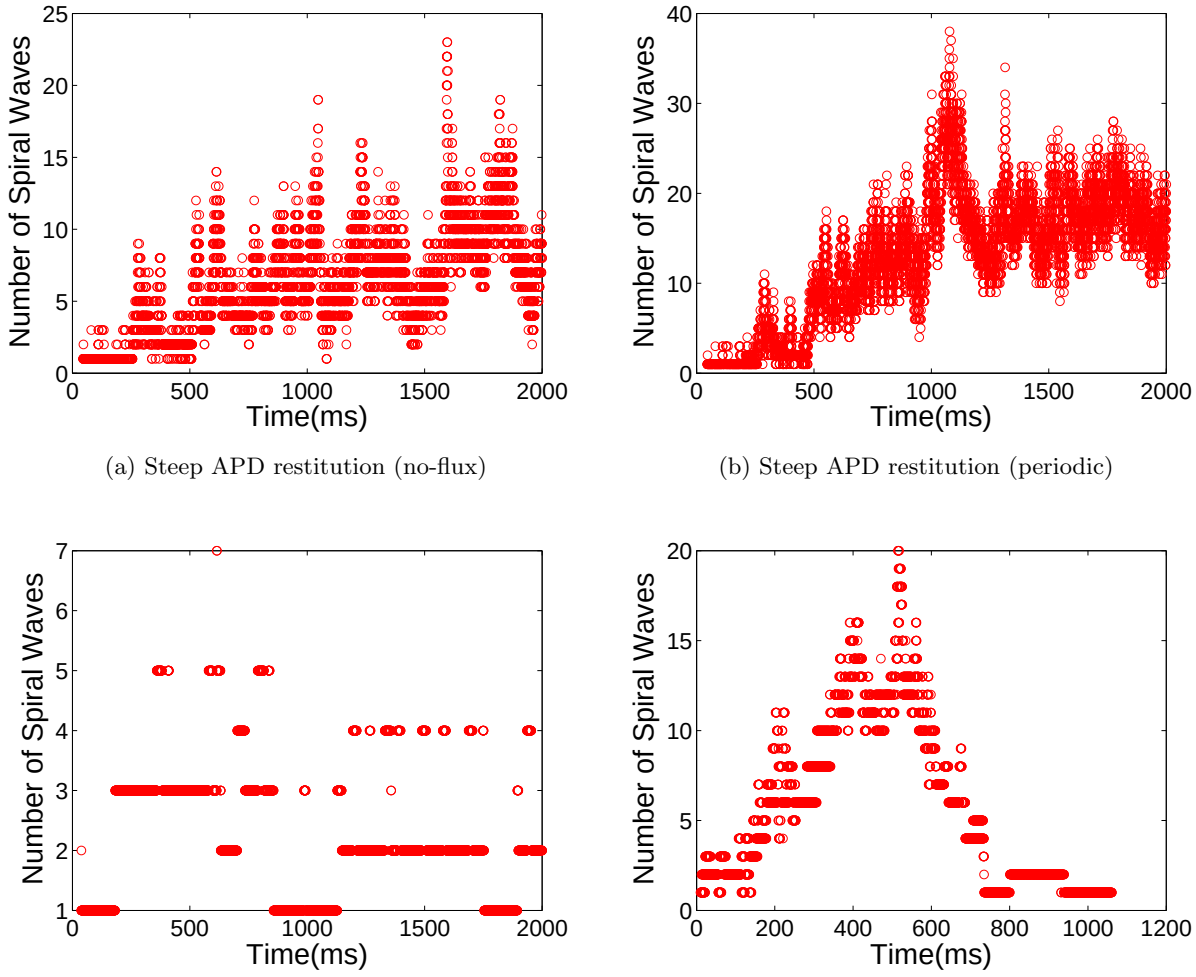

(a) Steep APD restitution (no-flux)

(b) Steep APD restitution (periodic)

(c) Doppler Effect (no-flux)

(d) Doppler Effect (periodic)

Figure 7.1: Distribution of number of spiral waves over time with no-flux and periodic boundary conditions

Figure 7.1b shows the effects of combining periodic boundary conditions with steep APD restitution. When steep APD restitution was implemented in isolation (See Figure 7.1a), it showed a similar distribution, wherein the number of waves increased with time. For this particular instance, adding periodic boundary conditions induced more breakup.

Figure 7.1d shows a combination of the Doppler effect and periodic boundary conditions. It

seems like the distribution of the number of waves changed drastically. When the Doppler effect was the only breakup mechanism in effect (See Figure 7.1c), the breakup was more uniform throughout the simulation. However, the addition of periodic boundary conditions not only increased the breakup, but also changed it such that the breakup increased until t=1000ms after which, the number of waves rapidly decreased culminating as a single wave. In summary, breakup was not sustained through the simulation. From these observations, it is clear that combining different mechanisms of breakup can yield results that differ from implementing the mechanism in isolation. Perhaps useful observations can be obtained by applying other metrics as we did above, which are opportunities for future research.

7.3 Future Work

The work presented here could be extended in several ways. The metrics that were considered can be expanded into looking at other properties of the spiral waves like the wavelengths and frequencies, which could serve to be useful. Examining more properties of spiral waves would improve our understanding how they develop and destabilize. With access to more training data, higher levels of accuracy can be achieved and more distinguishing features can possibly be found for each mechanism of breakup. It would also enable the application of machine-learning algorithms, which could yield better results.

As highlighted in [5], experimentally other mechanisms have been shown to produce spiral wave breakup. These mechanisms have been implemented in 3D to simulate the propagation of spiral waves in the ventricles. Investigating the implementations of the mechanisms in 3D can highlight the kind of variations that we may see by the application of our metrics to different kinds of data sets. In addition to this, access to more datasets of the mechanisms that were used in this thesis could also enhance the reliability of our approach and improve our metrics. Chapter 6 only involved testing four given datasets that exhibited three different mechanisms of spiral wave breakup. Future work in this area could also entail testing the metrics on other datasets that are known to produce breakup through mechanisms not covered in Chapter 6 and using different models.

Bibliography

[1] A. S. Go, D. Mozaffarian, V. L. Roger, E. J. Benjamin, J. D. Berry, M. J. Blaha, S. Dai, E. S. Ford, C. S. Fox, S. Franco, H. J. Fullerton, C. Gillespie, S. M. Hailpern, J. A. Heit, V. J. Howard, M. D. Huffman, S. E. Judd, B. M. Kissela, S. J. Kittner, D. T. Lackland, J. H. Lichtman, L. D. Lisabeth, R. H. Mackey, D. J. Magid, G. M. Marcus, A. Marelli, D. B. Matchar, D. K. McGuire, E. R. Mohler, C. S. Moy, M. E. Mussolino, R. W. Neumar, G. Nichol, D. K. Pandey, N. P. Paynter, M. J. Reeves, P. D. Sorlie, J. Stein, A. Towfighi, T. N. Turan, S. S. Virani, N. D. Wong, D. Woo, and M. B. Turner, "Heart disease and stroke statistics 2014 update: A report from the american heart association," *Circulation*, vol. 129, no. 3, pp. e28–e292, 2014.

[2] J. M. Davidenko, A. V. Pertsov, R. Salomonsz, W. Baxter, and J. Jalife, "Stationary and drifting spiral waves of excitation in isolated cardiac muscle," *Nature*, vol. 355, pp. 349–351, 1992.

[3] F. X. Witkowski, L. J. Leon, P. A. Penkoske, W. R. Giles, M. L. Spano, W. L. Ditto, and A. T. Winfree, "Spatiotemporal evolution of ventricular fibrillation," *Nature*, vol. 392, pp. 78–82, 1998.

[4] R. A. Gray, A. M. Pertsov, and J. Jalife, "Spatial and temporal organization during cardiac fibrillation," *Nature*, vol. 392, no. 6671, pp. 75–78, 1998.

[5] F. H. Fenton, E. M. Cherry, H. M. Hastings, and S. J. Evans, "Multiple mechanisms of spiral wave breakup in a model of cardiac electrical activity," *Chaos: An Interdisciplinary Journal*

of Nonlinear Science, vol. 12, no. 3, pp. 852–892, 2002.

[6] F. Fenton and A. Karma, "Vortex dynamics in three-dimensional continuous myocardium with fiber rotation: Filament instability and fibrillation," *Chaos: An Interdisciplinary Journal of Nonlinear Science*, vol. 8, no. 1, pp. 20–47, 1998.

[7] National Institutes of Health, "Understanding the heart's electrical system and ekg results." `http://www.nhlbi.nih.gov/health/health-topics/topics/hb/understanding.html`, July 2012.

[8] "Preliminary report: Effect of encainide and flecainide on mortality in a randomized trial of arrhythmia suppression after myocardial infarction," *New England Journal of Medicine*, vol. 321, no. 6, pp. 406–412, 1995.

[9] "Effect of the antiarrhythmic agent moricizine on survival after myocardial infarction," *New England Journal of Medicine*, vol. 327, no. 4, pp. 227–233, 1992.

[10] D. S. Echt, P. R. Liebson, L. B. Mitchell, R. W. Peters, D. Obias-Manno, A. H. Barker, D. Arensberg, A. Baker, L. Friedman, H. L. Greene, M. L. Huther, and D. W. Richardson, "Mortality and morbidity in patients receiving encainide, flecainide, or placebo," *New England Journal of Medicine*, vol. 324, no. 12, pp. 781–788, 1991.

[11] A. L. Waldo, A. J. Camm, H. deRuyter, P. L. Friedman, D. J. MacNeil, J. F. Pauls, B. Pitt, C. M. Pratt, P. J. Schwartz, and E. P. Veltri, "Effect of d-sotalol on mortality in patients with left ventricular dysfunction after recent and remote myocardial infarction. the sword investigators. survival with oral d-sotalol.," *Lancet*, vol. 348, no. 9019, pp. 7–12, 1996.

[12] R. A. Gray, J. P. Wikswo, and N. F. Otani, "Origin choice and petal loss in the flower garden of spiral wave tip trajectories," *Chaos: An Interdisciplinary Journal of Nonlinear Science*, vol. 19, no. 3, 2009.

[13] R. N. Fogors M.D., *Electrophysiologic Testing-5th Edition*. Wiley-Blackwell, 2012.

[14] J. N. Weiss, Z. Qu, P.-S. Chen, S.-F. Lin, H. S. Karagueuzian, H. Hayashi, A. Garfinkel, and A. Karma, "The dynamics of cardiac fibrillation," *Circulation*, vol. 112, no. 8, pp. 1232–1240, 2005.

[15] J. N. Weiss, P.-S. Chen, Z. Qu, H. S. Karagueuzian, and A. Garfinkel, "Ventricular fibrillation: How do we stop the waves from breaking?," *Circulation Research*, vol. 87, no. 12, pp. 1103–1107, 2000.

[16] J. B. Nolasco and R. W. Dahlen, "A graphic method for the study of alternation in cardiac action potentials.," *Journal of Applied Physiology*, vol. 25, no. 2, pp. 191–196, 1968.

[17] M. Guevara, G. Ward, A. Shrier, and L. Glass, "Electrical alternans and period-doubling bifurcations," *IEEE Computers in Cardiology*, vol. 11, pp. 167–170, 1984.

[18] A. T. Winfree, "Varieties of spiral wave behavior: An experimentalists approach to the theory of excitable media," *Chaos: An Interdisciplinary Journal of Nonlinear Science*, vol. 1, no. 3, pp. 303–334, 1991.

[19] R. A. Gray, J. Jalife, A. Panfilov, W. T. Baxter, C. Cabo, J. M. Davidenko, and A. M. Pertsov, "Nonstationary vortexlike reentrant activity as a mechanism of polymorphic ventricular tachycardia in the isolated rabbit heart," *Circulation*, vol. 91, no. 9, pp. 2454–2469, 1995.

[20] Z. Qu, J. N. Weiss, and A. Garfinkel, "Cardiac electrical restitution properties and stability of reentrant spiral waves: a simulation study," *American Journal of Physiology - Heart and Circulatory Physiology*, vol. 276, no. 1, pp. H269–H283, 1999.

[21] A. Garfinkel, Y.-H. Kim, O. Voroshilovsky, Z. Qu, J. R. Kil, M.-H. Lee, H. S. Karagueuzian, J. N. Weiss, and P.-S. Chen, "Preventing ventricular fibrillation by flattening cardiac restitution," *Proceedings of the National Academy of Sciences*, vol. 97, no. 11, pp. 6061–6066, 2000.

[22] J. O. Schwab, "Antitachycardia pacing to terminate ventricular tachyarrhythmia: new insights into how to reduce painful implantable cardioverter defibrillator shocks," *Europace*, vol. 14, no. 10, pp. 1381–1382, 2012.

[23] M. Courtemanche, L. Glass, and J. Keener, "Instabilities of a propagating pulse in a ring of excitable media," *Physical Review Letters*, vol. 70, no. 14, pp. 2182–2185, 1993.

[24] A. Karma, H. Levine, and X. Zou, "Theory of pulse instabilities in electrophysiological models of excitable tissues," *Physica D*, vol. 73, no. 1-2, pp. 113–127, 1994.

[25] G. W. Beeler and H. Reuter, "Reconstruction of the action potential of ventricular myocardial fibres," *The Journal of Physiology*, vol. 268, no. 1, pp. 177–210, 1977.

[26] M. Watanabe, F. Fenton, S. Evans, H. Hastings, and A. Karma, "Mechanisms for discordant alternans," *J. Cardiovasc. Electrophysiol.*, vol. 12, no. 2, pp. 196–206, 2001.

[27] Z. Qu, A. Garfinkel, P.-S. Chen, and J. N. Weiss, "Mechanisms of discordant alternans and induction of reentry in simulated cardiac tissue," *Circulation*, vol. 102, no. 14, pp. 1664–1670, 2000.

[28] O. Kwon, T. Y. Kim, and K. J. Lee, "Period-2 spiral waves supported by nonmonotonic wave dispersion," *Phys. Rev. E*, vol. 82, no. 4, p. 046213, 2010.

[29] E. Cherry, F. Fenton, H. Hastings, F. Xie, A. Garfinkel, J. Weiss, and S. Evans, "The role of decreased conduction velocity in the initiation and maintenance of atrial fibrillation in a computer model of human atria.," *Pacing and Clinical Electrophysiology*, vol. 24, no. 538, 2002.

[30] F. Fenton, H. Hastings, F. Xie, A. Garfinkel, J. Weiss, and S. Evans, "Validation of realistic 3d computer models of ventricular arrhythmias with optical mapping experiments," *Pacing and Clinical Electrophysiology*, vol. 24, no. 538, 2002.

[31] F. Fenton, H. Hastings, F. Xie, A. Garfinkel, J. Weiss, and S. Evans, "Effects of restitution and activation shape on the dynamics of cell models," *unpublished*.

[32] F. Fenton and A. Karma, "Fiber-rotation-induced vortex turbulence in thick myocardium," *Phys. Rev. Lett.*, vol. 81, no. 2, pp. 481–484, 1998.

[33] F. Fenton, "Theoretical investigation of spiral and scroll wave instabilities underlying cardiac fibrillation," *Ph.D. thesis, Northeastern University, Boston, MA*, 1999.

[34] I. Banville and R. Gray, "Effect of action potential duration and conduction velocity restitution and their spatial dispersion on alternans and the stability of arrhythmias," *J Cardiovasc Electrophysiol*, vol. 13, no. 11, pp. 1141–1149, 2002.

[35] A. Arif, "The numerical solution of elliptic and parabolic partial differential equations with boundary singularities," *Journal of Computational Physics*, vol. 26, no. 3, pp. 285 – 296, 1978.

[36] K. in 't Hout and B. Welfert, "Unconditional stability of second-order ADI schemes applied to multi-dimensional diffusion equations with mixed derivative terms," *Applied Numerical Mathematics*, vol. 59, no. 34, pp. 677 – 692, 2009.

[37] D. W. Peaceman and H. H. Rachford Jr., "The numerical solution of parabolic and elliptic differential equations," *Journal of the Society for Industrial and Applied Mathematics 3*, vol. 3, no. 1, pp. 28–41, 1955.

[38] N. F. Otani, "A primary mechanism for spiral wave meandering," *Chaos: An Interdisciplinary Journal of Nonlinear Science*, vol. 12, no. 3, pp. 829–842, 2002.

[39] V. G. Fast and A. M. Pertsov, "Drift of vortex in the myocardium," *Biofizika*, vol. 35, 1990.

[40] A. S. Mikhailov and V. S. Zykov, "Kinematical theory of spiral waves in excitable media:comparison with numerical simulations," *Physica D*, vol. 52, pp. 379–397, 1991.

[41] J. Beaumont, N. Davidenko, J. M. Davidenko, and J. Jalife, "Spiral waves in two-dimensional models of ventricular muscle: Formation of a stationary core," *Biophys. J.*, vol. 75, pp. 1–14, 1998.

[42] N. F. Otani, "A primary mechanism for spiral wave meandering," *Chaos: An Interdisciplinary Journal of Nonlinear Science*, vol. 12, no. 3, pp. 829–842, 2002.

[43] E. M. Cherry and F. H. Fenton, "Visualization of spiral and scroll waves in simulated and experimental cardiac tissue," *New Journal of Physics*, vol. 10, no. 12, 2008.

[44] R. L. Devaney, *An Introduction to Chaotic Dynamical Systems*. Second ed. Westview, 2003.

[45] C.-E. E. Meador, "Numerical calculation of lyapunov exponents for three-dimensional systems of ordinary differential equations," *Theses, Dissertations and Capstones*, no. 107, 2011.

[46] Y. Sun, "Fault detection in dynamic systems using the largest lyapunov exponent," *Thesis*, 2011.

[47] J. C. Sprott, *Chaos and Time-Series Analysis*. University of Wisconsin-Madison: Oxford University Press, 2003.

[48] S. Wu M.D.Ph.D., J. N. Weiss M.D., C.-C. Chou M.D., M. Attin R.N., H. Hayashi M.D. Ph.D., and S.-F. Lin Ph.D., "Dissociation of membrane potential and intracellular calcium during ventricular fibrillation," *Journal of Cardiovascular Electrophysiology*, vol. 16, no. 2, pp. 186–192, 2005.

[49] T. M. Cover and J. A. Thomas, *Elements of Information Theory*. John Wiley and Sons,Inc, 1991.

[50] P. V. Bayly, B. H. KenKnight, J. M. Rogers, E. E. Johnson, R. E. Ideker, and W. M. Smith, "Spatial organization, predictability, and determinism in ventricular fibrillation," *Chaos: An Interdisciplinary Journal of Nonlinear Science*, vol. 8, no. 1, pp. 103–115, 1998.

[51] R. H. Clayton and A. V. Holden, "Dynamics and interaction of filaments in a computational model of re-entrant ventricular fibrillation," *Physics in Medicine and Biology*, vol. 47, no. 10, p. 1777, 2002.

[52] C. H. Luo and Y. Rudy, "A model of the ventricular cardiac action potential. depolarization, repolarization, and their interaction.," *Circulation Research*, vol. 68, no. 6, pp. 1501–26, 1991.

[53] X. Zeng, R. Eykholt, and R. A. Pielke, "Estimating the lyapunov-exponent spectrum from short time series of low precision," *Phys. Rev. Lett.*, vol. 66, no. 25, pp. 3229–3232, 1991.

[54] R. Clayton and A. Holden, "Filament behavior in a computational model of ventricular fibrillation in the canine heart," *IEEE Transactions on Biomedical Engineering*, vol. 51, no. 1, pp. 28–34, 2004.

[55] M. Courtemanche, "Complex spiral wave dynamics in a spatially distributed ionic model of cardiac electrical activity," *Chaos: An Interdisciplinary Journal of Nonlinear Science*, vol. 6, no. 4, pp. 579–600, 1996.

[56] M. Courtemanche and A. T. Winfree, "Re-entrant rotating waves in a beeler-reuter based model of two-dimensional cardiac electrical activity," *International Journal of Bifurcation and Chaos*, vol. 1, no. 2, pp. 431–444, 1991.

[57] A. V. Holden and A. V. Panfilov, "Spatiotemporal chaos in a model of cardiac electrical activity," *Int. J. Bifurcation Chaos Appl. Sci. Eng.*, vol. 1, pp. 219–225, 1991.

[58] A. Karma, "Electrical alternans and spiral wave breakup in cardiac tissue," *Chaos: An Interdisciplinary Journal of Nonlinear Science*, vol. 4, no. 3, pp. 461–472, 1994.

[59] A. Karma, "Spiral breakup in model equations of action potential propagation in cardiac tissue," *Phys. Rev. Lett.*, vol. 71, no. 7, pp. 1103–1106, 1993.

[60] J. J. Fox, M. L. Riccio, F. Hua, E. Bodenschatz, and E. E. Gilmour Jr., "Spatiotemporal transition to conduction block in canine ventricle," *Circ. Res.*, vol. 90, no. 3, pp. 289–296, 2002.

[61] Z. Qu, A. Garfinkel, P.-S. Chen, and J. N. Weiss, "Mechanism of ventricular vulnerability to single premature stimuli in open-chest dogs," *Circ. Res.*, vol. 62, pp. 1191–1209, 1988.

[62] J. N. Weiss, A. Garfinkel, H. S. Karagueuzian, Z. Qu, and P.-S. Chen, "Chaos and the transition to ventricular fibrillation: A new approach to antiarrhythmic drug evaluation," *Circulation*, vol. 9, no. 21, pp. 2819–2826, 1999.

[63] J. Nolasco and R. Dahlen, "A graphic method for the study of alternation in cardiac action potentials," *J. Appl. Physiol.*, vol. 25, pp. 191–196, 1968.

[64] F. H. Fenton, "Numerical simulations of cardiac dynamics. what can we learn from simple and complex models?."

[65] D. G. Dritschel and B. Legras, *Modeling oceanic and atmospheric vortices.* Physics Today 46, 1993.

[66] J. Braun and M. Sambridge, *A numerical method for solving partial differential equations on highly irregular evolving grids.* Nature 376, 1995.

[67] J.-H. Xiao, G. Zhang, and B. Hu, "Controlling the breakup of spiral waves in an excitable medium by applying time-delay feedback signals," *Europhys. Lett.*, vol. 69, no. 1, pp. 29–35, 2005.

[68] F. H. Fenton, E. M. Cherry, and L. Glass, "Cardiac arrhythmia," 2008.

[69] A. Pearanda, I. R. Cantalapiedra, J. Bragard, and B. Echebarria, "Cardiac dynamics: a simplified model for action potential propagation," *Theoretical Biology and Medical Modelling*, vol. 9, no. 1, p. 50, 2012.